The Key Laboratory of Weak Light Nonlinear Photonics,
Ministry of Education

Annual Report 2009

南开大学弱光非线性光子学

教育部重点实验室

Annual Report 2009

The Key Laboratory of Weak Light Nonlinear Photonics,
Ministry of Education

南开大学弱光非线性光子学

教育部重点实验室

▼ 乌克兰国家科学院物理所的 Andrey Iljin 研究员来访并进行学术交流。（2009.2.16-3.14）

▼ 德国 Osnabrück 大学的 Peter Hertel 教授访问我院。（2009.4.7）

▼ 人工晶体研究所副院长黄存新教授受聘为兼职教授。（2009.5.8）
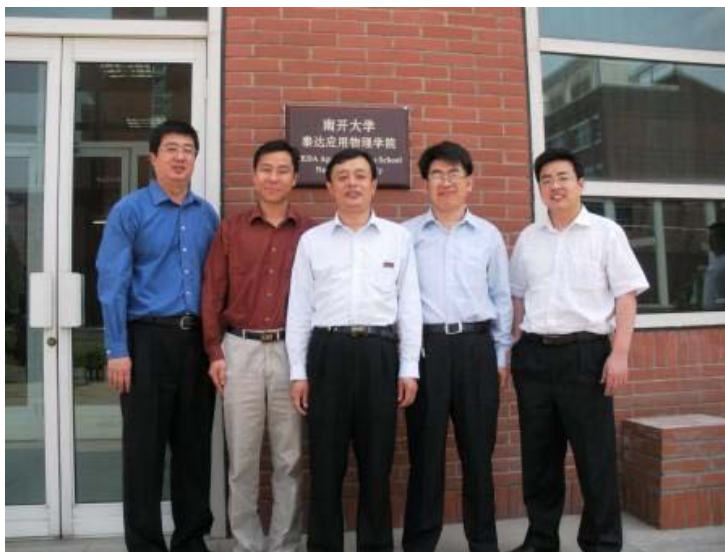
▼牛津大学 Robert A. Taylor 教授来访。（2009.5.24-5.27）

▼ 乌兹别克斯坦 Mirzo Ulugbek 国立大学的 Uyugun Vakhidovich Valiev 教授进行学术交流访问。（2009.5.20-7.20）

▼麻省理工学院 Keith A. Nelson 教授访问了我院。（2009.6.13-17）

▼ 法国 Thales Research & Technology 中心的 Brigitte Loiseaux 教授参观访问了我院。（2009.6.26）

▼ 德国德累斯顿工业大学的 Alexander Eychmüller 教授访问我院。（2009.8.17）

▼ 德国亚琛工业大学 Georg Roth 教授来我院访问。（2009.9.25）

▼ 法国 Thales Research & Technology 中心的 Brigitte Loiseaux 教授参观访问了我院。（2009.6.26）
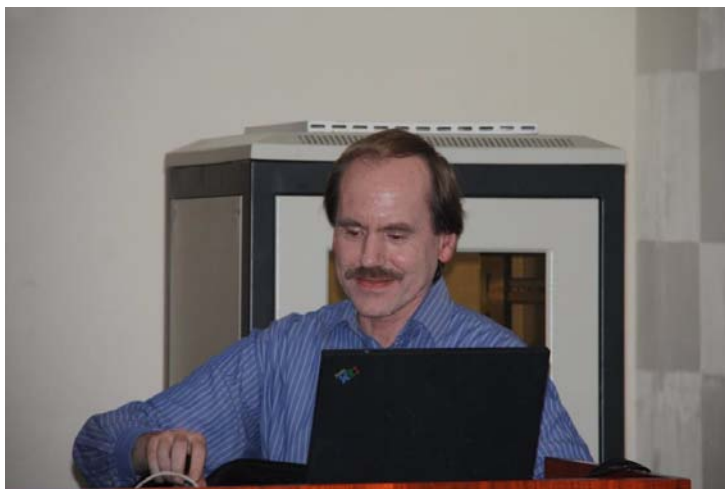
▼ MIT 博士生 Christopher A. Werley 访问我院。（2009.10.12）
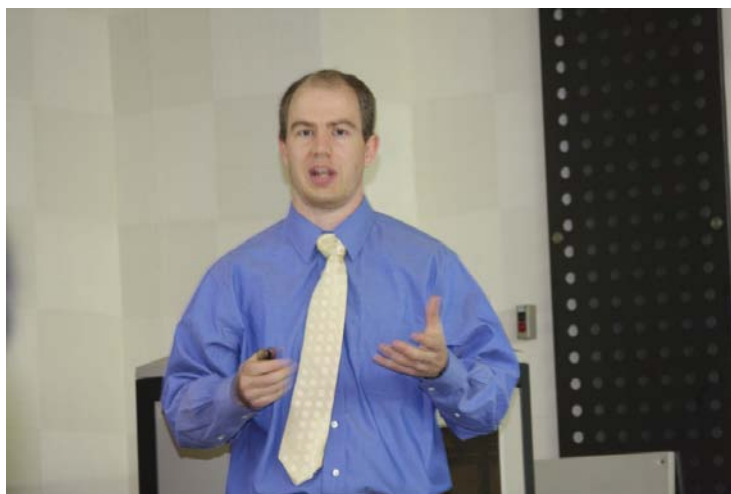
▼ 中科院段宣明、刘前研究员受聘为兼职教授。（2009.11.4）

▼ 美国亚利桑那大学光学科学院 Arturo Pirson-Chavez 博士来访。

（2009.11.9）
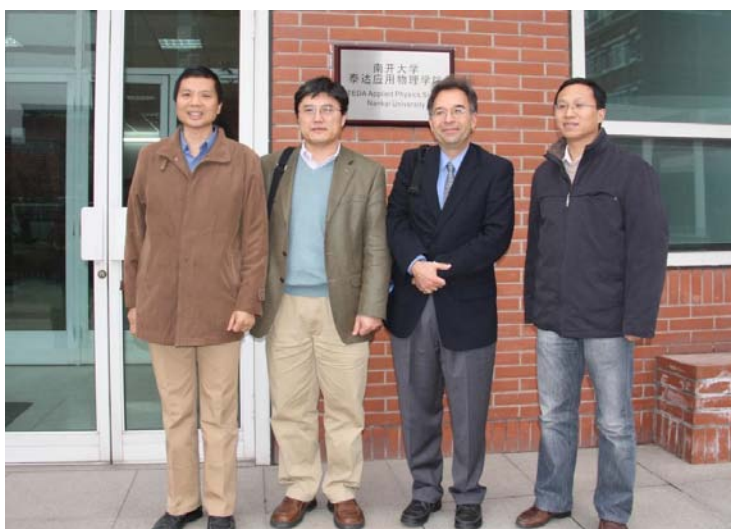
前　言/Preface

In 2009, the work at our lab was mainly focused on optical nonlinearities of organic materials, functional optical crystals, micro-crystal glass ceramics, nano-particulate films, up-conversion-luminescent materials, rare-earth doped glasses and their microstructures, also nonlinear optical manipulation of light in photonics structures. Especially achieved some fruitful results in the slow-light nonlinear optics and addressable optical buffer memory by EIT, the graphene hybrid material covalently functionalized with Porphyrin and optical limiting, optical trapping and manipulation of metallic micro-particles, generation of propagating plasmons by electron beams. In addition our newly startup researches are going along well, such as the silicon based MOS light emitting devices, weak-light nonlinear bio-optical effects, et al. In this report, we present a short summary of the results achieved in each line of activity of 2009.

All the activities summarised here have been done in the frame of international projects, cooperation agreements, and contracts with NSFC, MOE, MOST and Tianjin Municipal government. We also benefit a lot from our colleagues from other units all over world, who provide us advices and supports. Many thanks for their kind supports. In addition, our staff and students worked hard in order to make our research better and faster. Thanks a lot for their indispensible contributions and wonderful research works.

Here I would also like to stress that our research works in topics of ultrafast detection and analysis by fs technology, semiconductor growth, and spectrally sensing techniques have been not going along well in 2009 and we do hope that we can catch up and achieve more in 2010.

Prof. Dr. Jingjun Xu

Director,

The Key laboratory of Weak-Light Nonlinear Photonics

目　录/Contents

人员结构/Organization

实验室主任/Director

　　许京军　教　授

实验室副主任/Deputy Directors　　　　　　　　　　　　学术秘书/Academical Secretary

　　张国权　教　授　　　　　　　　　　　　　　　　禹宣伊　副教授

　　孙　骞　教　授

研究方向负责人/Research Group Leaders

　　弱光非线性及量子相干光学　　　许京军　教　授

　　非线性物理与光子技术　　　　　田建国　教　授

　　光子学材料及先进制备技术　　　孔勇发　教　授

　　光谱表征及传感技术　　　　　　臧维平　教　授

　　半导体生长技术和半导体器件　　舒永春　教　授

学术委员会/Academic Committee

主　任/Chairman

　　王占国　院　士　　　　　　（中国科学院半导体研究所）

委　员/ Committee Members

　　沈德忠　院　士　　　　　　（清华大学化学系功能晶体与薄膜研究所）

　　薛其坤　院　士　　　　　　（清华大学物理系）

　　姚建年　院　士　　　　　　（中国科学院化学研究所）

　　许宁生　教　授　　　　　　（中山大学理学院）

　　陈志刚　教　授　　　　　　（南开大学物理科学学院）

　　龚旗煌　教　授　　　　　　（北京大学物理学院）

　　陆　卫　研究员　　　　　　（中国科学院上海技术物理研究所）

　　田建国　教　授　　　　　　（南开大学物理科学学院）

　　王慧田　教　授　　　　　　（南开大学物理科学学院）

　　徐现刚　教　授　　　　　　（山东大学晶体材料国家重点实验室）

　　许京军　教　授　　　　　　（南开大学物理科学学院）

　　资　剑　教　授　　　　　　（上海市复旦大学表面物理国家重点实验室）

外籍学术顾问委员

　　D. Kip　　　　　　教　授　德国 Cauthburge 大学

　　L. Hessenlink　　教　授　美国斯坦福大学物理系

　　R. A. Rupp　　　教　授　奥地利维也纳大学实验物理所

　　T. Volk　　　　　教　授　俄罗斯国家晶体研究所

　　Y. Tomita　　　　教　授　日本电气通信大学

　　K. A. Nelson　　　教　授　美国麻省理工学院

杰出人才/Intelligent Staff

教育部"长江奖励计划"特聘教授

    许京军（1999）   王慧田（1999）   陈志刚（2006）

国家杰出青年基金获得者

    许京军（1998）   田建国（2001）   王慧田（2003）   李宝会（2009）

教育部"优秀青年教师资助计划"入选者

    张国权（2002）   宋　峰（2003）

教育部"跨世纪优秀人才培养计划"入选者

    许京军（1998）   田建国（2000）   孙　骞（2001）   孔勇发（2002）

教育部"新世纪优秀人才支持计划"入选者

    张国权（2004）   宋　峰（2004）   臧维平（2005）   李宝会（2005）

    徐章程（2006）   孙甲明（2007）   张心正（2008）   刘智波（2009）

首批新世纪百千万人才工程国家级人选

    田建国（2004）

国家海外青年学者合作研究基金获得者

    陈志刚（2005）

"天津市授衔专家"称号获得者

    许京军（2005）   田建国（2005）

教育部"长江学者和创新团队发展计划"创新团队基金资助

杰出人才/Intelligent Staff

弱光非线性光子学重点实验室人员名录/Name List

研究人员/Scientific Staff（47 人）

王占国	许京军	王慧田	田建国	Romano A. Rupp	陈志刚	张国权	孔勇发	孙 骞
宋 峰	臧维平	李宝会	舒永春	徐章程	姚江宏	赵丽娟	曹亚安	孙甲明	张天浩
李玉栋	徐晓轩	张心正	周文远	乔海军	邢晓东	禹宣伊	余 华	吴 强	孙同庆
武 莉	楼慈波	高 峰	刘智波	李祖斌	薄 方	齐继伟	叶 青	潘雷霆	蔡 卫
陈树琪	宋道红	孙 军	张 玲（兼）	刘士国（兼）	唐柏权（兼）	李 威（兼）
王振华（兼）

技术人员/Technical Staff（6 人）

黄自恒　陈绍林　马玉祥　张 玲　刘士国　王振华

行政人员/ administrative Staff（3 人）

梁 建　李 威　唐柏权

博士生/Ph.D Students（64 人）

胡 毅	叶卓艺	郭 贺	孔凡磊	赵立华	孙立萍	郝志强	刘建彬	祁轶舲	齐新元
窦宜领	许宁宁	翟召辉	龚 亮	李 俊	王 喆	边 飞	王俊俏	张学智	任梦昕
向吟啸	程 化	郝召锋	鄂小卿	李建威	张校亮	刘 欣	栗建兴	应翠凤	王文杰
刘富才	师丽红	张雅婷	李燕丽	曹永强	翟晓辉	王恩君	裴子栋	冯页新	董江舟
袁继翔	张新星	周凯迪	叶志诚	李俊梅	刘海旭	袁志翔	张新星	周凯迪	明成国
王青如	刘加东	施曙东	吴 限	谭信辉	石 凡	辛非非	洪佩龙	刘鹏翊	梁 毅
闫卫国	葛新宇	程 辉	韦 晨

硕士生/M.S. Students（144 人）

王慎之	钱学波	谢 楠	高光宇	胡金霞	张文定	段长莎	辛非非	刘 泽	孙海峰
李 辉	金妮娜	李 建	李 祥	李海燕	陈宗强	陈子坚	郭尚雨	胡 皓	徐 燕
杨 冉	刘 泽	南晓宇	惠王伟	张墨林	马雅盛	赵子宇	余 璇	梅剑春	惠王伟
杨晓玲	李亚东	徐 建	刘世松	史 烁	赵 欣	李 艳	刘博洋	李西峰	孟翔峰
何 嵩	孔祥天	阚颖慧	高洪利	寇大勇	杨 熹	韩 榕	刘张骞	马海梅	安旭东
李昕睿	平维杰	杨 东	胡 欣	高冬子	匡元江	周 波	崔 磊	王利忠	周晓东
季鸣元	曾 浩	田 甜	陈金金	杨晓丹	王海涛	韩文卿	董印锋	陈 猛	陈 鸿
田 澍	梁启锐	胡 男	曹 雪	张威威	张新霞	杨 阳	张俊杰	王静密	王 醉
朱鸿雁	康 培	姚惠梓	李 洁	卢志璐	王红亚	侯春霄	宋令枝	郑一凡	胡 男
胡承学	张宇佳	朴文益	于 音	蔡莹莹	郭 宁	骆兰军	王文涛	赵红艳	樊学芳
李 伟	李 斌	赵 飞	王莲莲	孟 涛	杨 明	陈战东	尹鹏飞	杨 涛	郭燕磊
辛建康	栾艳彩	代 林	范小龙	石伟科	张光子	李 莉	马 强	刘文波	张建峰
樊文博	孟 楠	郑先明	郭丽梅	张 铭	张 盼	王亚洲	王 俊	赵建彬	张 宇
王景声	朱美玲	胡永能	孟繁杰	颜艳花	王云峰	栾 星	李广平	邢 飞	董职福
杜 鹏	王 芳	张 超	张 功

弱光非线性光子学重点实验室人员名录/Name List

承担课题/Projects under Researching

序号	项 目 名 称	项 目 来 源	起止时间	负责人
1	纳/微结构非线性光学、光调控与器件应用研究	973 项目	2007.5-2012.8	许京军
2	光诱导人工光学结构及光传播特性研究	973 项目	2007.7-2011.12	陈志刚
3	硅基发光材料与光互联的基础研究（南开部分）	973 项目	2007.7-2012.12	孙甲明
4	氧化物介观薄膜原子尺度可控制备与超快紫外器件研究（南开部分）	973 项目	2007.5-2011.4	孔勇发
5	表面等离子体共振定向辐射机理及超高方向性辐射特性研究（南开部分）	973 项目	2006.7-2010.6	宋峰
6	基于亚波长尺度光纤的复合波导结构与新器件（南开部分）	973 项目	2008.1-2010.12	孙骞
7	光泵浦 1064nm 半导体垂直外腔表面发射激光器芯片材料的制备	863 项目	2006.12-2009.12	舒永春
8	四价掺杂铌酸锂晶体	863 新材料技术	2007.12-2010.11	孔勇发
9	关联光子学微结构阵列的光传输与调控研究	国家重大科学研究计划	2007.1-2011.12	田建国
10	弱光非线性光子学科学与技术创新引智基地	111 计划	2007.1-2011.12	许京军

承担课题/Projects under Researching

11	基于一维光自带隙结构的光限制效应研究	国家自然科学基金	2007.1-2009.12	臧维平
12	弱关联光子晶格体系中飞秒光传播特性及其导致的非线性光学效应	国家自然科学基金	2007.1-2009.12	吴强
13	光学相干周期微结构系综的光学性质	国家自然科学基金	2007.1-2009.12	张国权
14	光折变非线性表面光波导及其应用研究	国家自然科学基金	2007.1-2009.12	张天浩
15	电场调制下纳米硅微晶和 Er 离子耦合系统的发光特性和高效率场致发光	国家自然科学基金	2008.1-2010.12	孙甲明
16	掺 Er 磷酸盐玻璃陶瓷的发光和激光特性	国家自然科学基金	2008.1-2010.12	宋峰
17	聚合物/无机量子点红外复合材料的非线性和超快光谱研究	国家自然科学基金	2008.1-2010.12	徐章程
18	Er^{3+}离子掺杂钨酸镧钾晶体的生长和性质研究	国家自然科学基金	2008.1-2010.12	孙同庆
19	有机超分子材料的光学非线性调控及其应用研究	国家自然科学基金	2008.1-2010.12	刘智波
20	光诱导铌酸锂表面金属微纳结构及其与光的相互作用	国家自然科学基金	2009.1-2011.12	张心正
21	超声调制复合周期性折射率结构与光群速调控的研究	国家自然科学基金	2009.1-2011.12	高峰
22	基于光流体的荧光光源及其光子学性质的研究	国家自然科学基金	2009.1-2011.12	禹宣伊
23	高效率纳米 TiO2 基复合固溶体新型可见光催化剂的制备	国家自然科学基金	2009.1-2011.12	曹亚安

24	复合微纳阵列结构的光调控及其应用研究	教育部科技创新工程重大项目培育资金项目	2009.1-2011.12	张国权
25	近红外有机/无机量子点复合材料和器件	教育部新世纪优秀人才支持计划	2007.1-2009.12	徐章程
26	高效率的硅 MOS 电致发光器件	教育部新世纪优秀人才支持计划	2008.1-2010.12	孙甲明
27	光子局域化中的相干背散射研究	教育部新世纪优秀人才支持计划	2009.1-2011.12	张心正
28	石墨烯材料光学非线性及其机制研究	教育部科学技术研究重点项目	2009.1-2011.12	刘智波
29	新型激光自倍频晶体基质材料五磷酸镧二钾的生长与性质研究	教育部高等学校博士点新教师基金	2008.1-2010.12	孙同庆
30	Er 掺杂的富硅 SiO_2 MOS 结构的高效率场效应电致发光	教育部高等学校博士点新教师基金	2008.1-2010.12	孙甲明
31	新型硼酸盐发光材料结构与性能研究	教育部高等学校博士点新教师基金	2008.1-2010.12	武莉
32	有机超分子材料光学非线性研究	教育部高等学校博士点新教师基金	2008.1-2010.12	刘智波
33	亚波长结构光传播性质的研究	教育部高等学校博士点新教师基金	2008.1-2010.12	李祖斌
34	表面等离子体共振及共振条件下的拉曼光谱研究	教育部高等学校博士点新教师基金	2008.1-2010.12	王斌
35	动态和静态光栅中光脉冲形变的抑制	教育部高等学校博士点新教师基金	2009.1-2011.12	薄方
36	掺锆铌酸锂晶体的缺陷模型和畴反转研究	教育部高等学校博士点新教师基金	2009.1-2011.12	刘宏德

37	稀土掺杂的硅基 MOS 结构电致发光	教育部留学回国人员基金	2009.1-2010.12	孙甲明
38	光泵浦 980nm 半导体垂直外腔表面发射激光器芯片的制备	天津市自然科学基金重点基金	2006.4-2009.12	舒永春
39	新型无机液体激光介质-掺稀土氟化物纳米晶溶胶	天津市自然科学基金重点基金	2009.4-2012.3	赵丽娟
40	矿石检测小型化激光拉曼光谱仪	天津市科技支撑计划重点项目	2007.4-2009.10	徐晓轩
41	若干新型弱光非线性效应及其应用的研究	天津市国际科技合作项目	2006.4-2009.3	张国权
42	弱光非线性光学新效应和机制	天津市科技创新能力与环境建设平台项目	2006.7-2009.6	孙骞
43	用相位编码方法在铌酸锂表面构造亚微米金属微结构	天津市自然科学基金	2007.4-2009.9	张心正
44	电磁波与微结构的瞬态相互作用	天津市自然科学基金	2009.4-2012.3	吴强
45	碳基材料复合物光学非线性及其应用研究	天津市自然科学基金	2009.4-2012.3	刘智波
46	碱金属碱土金属硼酸盐基发光材料结构与性能研究	天津市自然科学基金	2009.4-2012.3	武莉
47	长江学者启动基金	985	2006.3-2009.2	陈志刚
48	离散体系对瞬态量子相干的影响	教育部留学回国人员科研启动基金	2008.8-2009.08	张心正
49	聚合物/无机量子点红外复合材料中的载流子动力学	中科院上海技物所红外物理国家重点实验室开放课题	2007.6-2009.6	徐章程

50	拉曼表面增强传感器	精密测试技术及仪器国家重点实验室开放基金	2009.9-2012.9	徐晓轩
51	若干掺杂铌酸锂晶体的研制	横向课题	2008.8-2010.7	张玲
52	太阳能电池增透膜技术开发	横向课题	2009.12-2010.12	曹亚安
53	XXXXXX	军品配套项目		张玲
54	XXXXXX	军品配套项目		张玲
55	小型自动光纤拉丝机的研制	横向课题	2009.1-2009.6	宋峰

仪器设备平台/Facilities

仪器设备名称	规格型号	购置时间
激光器工作站	899-29	2005.09
飞秒激光器	VF-T2S	2000.08
皮秒激光器	PY61	2003.11
纳秒激光器	Panther OPO	2003.11
光纤激光器	PLY-20-M	2003.11
可调频再生放大器	Spitfire F-1K	2000.04
时间分辨光谱及瞬态吸收光谱系统	Spectrapro.300i	2000.04
光谱分析仪	AQ6315A	2005.09
显微拉曼光谱仪	MKI2000	1998.09
分子速外延生长炉	Riber Compact 21T	2003.09
提拉法晶体生长炉	研制	2002.04
晶体切割研磨抛光系统	Logitech 系列	2001.06
扫描探针显微镜	Nanoscope Ⅲa	2006.08

注：除开放基金外，所有仪器设备均为有偿使用

仪器设备平台/Facilities

研究工作报告／Scientific Report

非线性物理与光子技术/ Nonlinear Physics and Photonics Techniques

负责人：田建国

本方向涉及有机材料光学非线性、光在介质中的传播、光子带隙材料、亚波长微结构、以及非线性表面波等方面。本年度发表论文 14 篇；申请或授权专利 3 项。在研课题经费 467.88 万元。2009 年度"非线性物理与光子技术"方向主要在以下方面取得了进展：

In this field, we mainly focused on optical nonlinearities of organic materials, beam propagation, one dimensional photon crystal, sub-wavelength microstructure, and nonlinear surface waves. 14 papers have been published in international academic journals, and 3 patents applicanted. The total reasearching founds are 4.6788 millions. This year, we obtained some important results as following:

在有机材料光学非线性方面，我们在石墨烯和卟啉修饰石墨烯的光学非线性研究中，取得了较大的进展，我们报道了氧化石墨烯结构在纳秒和皮秒时域下的光学非线性，发现二维结构的石墨烯有着与其它两种碳结构材料（零维的富勒烯和一维的碳纳米管）不同的非线性机制，存在强的双光子吸收（图 1），发现卟啉修饰后的碳纳米管和石墨烯的光限制效应有较大提高（图 2）。通过对卟啉修饰石墨烯结构的紫外吸收和荧光特性的研究，我们认为光限制效应的提高除了反饱和吸收和非线性散射两种光限制机制的结合外，还可能有来自卟啉与石墨烯之间光致电子转移效应的贡献。其次，我们研究了各项同性介质中，三阶非线性的各项性异性导致的光束偏振态和介质光学非线性的变化，在 Z 扫描的理论和实验分析中我们首次引入了偏振态的影响，并获得了不同偏振光下的 Z 扫描解析表达式。

Optical nonlinearities of organic materials, such as porphyrin, graphene, have been measured. The nonlinear optical properties of graphene oxide were investigated at 532 nm in nanosecond and picosecond regimes. Results show that two-photon absorption dominates nonlinear absorption process of GO in the case of picosecond pulses, while excited state nonlinearities play an important role in the case of nanosecond pulses. In the studies of porphyrin-Graphene supramolecular system,the porphyrins covalently functionalized graphene
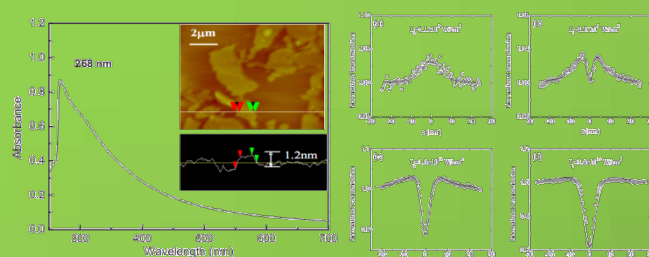
图 1 氧化石墨烯皮秒脉冲下开孔 Z 扫描曲线
Fig. 1 Open aperture Z-scan curves of GO in DMF at different intensities.
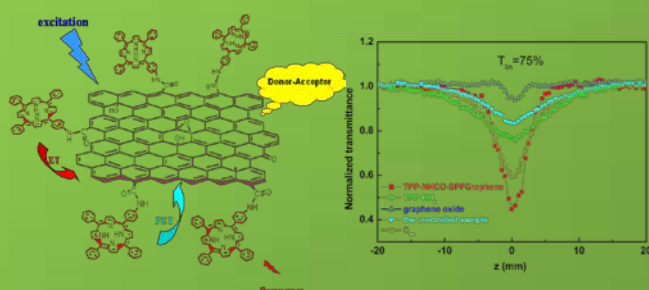
图 2 卟啉修饰石墨烯的光限制效应
Fig. 2 Optical limiting of porphyrin-Graphene supramolecular system

offered superior performance to C60, the individual graphene and porphyrins by combination of nonlinear mechanism of reverse saturable absorption and nonlinear scattering, and the photoinduced electron or energy transfer between porphyrin moiety and graphene also play an important role in improvements of optical limiting effect. Secondly, the evolutions of polarization and nonlinearities in an isotropic medium induced by anisotropy of third-order nonlinear susceptibility

were studied experimentally and theoretically. We report on an extension of common Z-scan method to arbitrary polarized incidence light for measurements of anisotropic thirdorder nonlinear susceptibility in isotropic medium. The normalized transmittance formulas of closed-aperture Z-scan are obtained for linearly, elliptically and circularly polarized incidence beam.

在光束在波导传播的理论分析方面，我们提出了采用广角分步有限差分和局域一维格式的算法来求解三维的标量波方程。从而将三维问题转化为两个二维方程，没有做慢变包络近似和单路传播近似。分析了倾斜波导的本征模传播问题。结果表明该方法具有高的精度和数值效率，如图 3 所示。理想匹配层边界条件很容易结合进来。
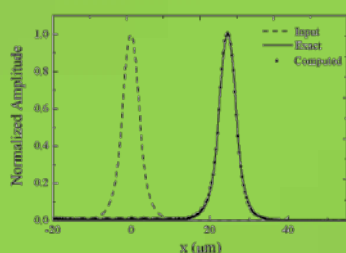
图 3 输入导模和沿波导传播了 60 微米后的输出导模在 x-z 平面的剖面图，倾斜波导管与 z 轴成 30 度夹角，与 x、y 轴均成 45 度夹角。
Fig.3 Profiles in x-z plane of input and out modulus of the mode propagating through a channel waveguide with 30 degrees tilted with respect to z axis 45 degrees with respect to both x and y axes over a distance of 60 um.

A wide-angle, split-step finite difference method with the classical local one-dimensional scheme is presented to analyze the three-dimensional scalar wave equation. Its essence is to convert the three-dimensional scalar wave equation into two two-dimensional equations that can be solved without using slowly varying envelope or one-way propagation approximations. The eigen-mode propagation in tilted step-index channel waveguide are compared with other beam propagation algorithms. Results show high accuracy and numerical efficiency. The perfectly matched layer boundary can be implemented easily.

在电子加速理论研究方面，当采用一个

紧聚焦高斯激光束来加速电子是，通常是采用 Lax 方面来求解电磁场。但是，Lax 级数表示有时发散，所以可能会导致一个不准确地模拟结果。我们提出采用 Weniger 变换来消除 Lax 级数的发散现象。得到了准确地电子加速动力学结果。

For an electron accelerated by a tightly focused Gaussian laser beam, its dynamics are usually simulated through the field obtained by Lax approach. However, as Lax series field (LSF) is not always convergent, the obtained results are usually inaccurate and even illogical. Here we report that the divergence of LSF can be eliminated by using Weniger transformation, and the electron dynamics simulated by this new field are accurate.
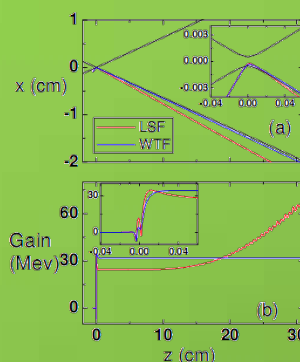
图 4 (a) 电子运动轨道图, (b) 激光光束中电子动态的能量增益
Fig.4 (a) The trajectories of the electron. (b) The energy gains of the electron dynamics in a laser beam.

在一维光子带隙材料方面，我们提出了一种理想的一维非线性光子带隙材料的 Z 扫描理论，我们的理论可以同时得到开孔和闭孔 Z 扫描曲线。我们分析了一维周期性非线性光子带隙材料的开孔和闭孔 Z 扫描曲线特征，结果表明只含非线性折射的一维非线性光子带隙材料的 Z 扫描曲线与同时包含非线性折射和非线性吸收的体材料 Z 扫描曲线相似。同时我们也讨论了非线性吸收对反射和透射 Z 扫描曲线的影响。我们的结果可以被用来拟合一维光子带隙材料的 Z 扫描实验结果，得到材料的非线性响应。同时，还可以优化一维光子带隙材料的结构设计，控制一维光子带隙材料在不同波长的应用，裁剪一维光子带隙材料的特性。

We presented a novel Z-scan theory for 1D nonlinear PBG materials, which enables a direct

calculation of both open- and closed-aperture Z-scan curves. We analyzed the Z-scan characteristics for a 1D PBG material, which are quite different from those of uniform materials. The effects of nonlinear absorption on reflected and transmitted Z-scan curves are also discussed. Our results can be used to simulate the experimental Z-scan results and obtain the nonlinear material response. Optimizing 1D PBG structure designs and operation wavelengths can be applied to engineer nonlinear PBG materials and tailor their properties for various applications.
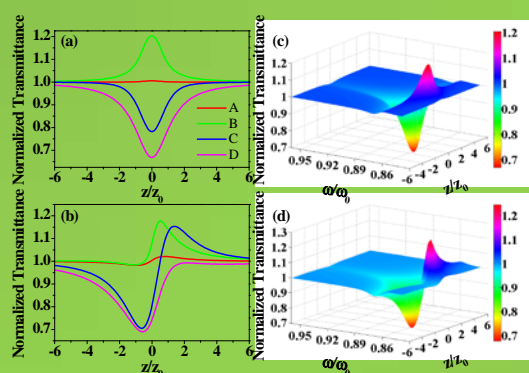
图 5、假设纯非线性折射情况下的 Z 扫描曲线。(a)(c)：开孔 Z 扫描；(b)(d)：闭孔 Z 扫描。

Fig 5. Z-scan curves assuming purely refractive nonlinearity. (a) and (c) Open- aperture Z-scan; (b) and (d) Closed-aperture Z-scan.

在飞秒激光微加工方面，我们提出了一种新的并行微加工方法。将具有不同曲率半径波面的光共线通过一个聚焦物镜，使之在样品不同深度处聚焦，从而实现样品上不同层之间的并行微结构加工。通过调整光束的波面曲率半径以及物镜的数值孔径，可以改变不同加工层之间的间距以及不同层之间的对准度。我们用这种方法加工了双层的菲涅尔波带片（见图6）。这种并行加工方法可以大大缩短飞秒微结构加工的时间。

We present a parallel writing method in silica glass by multiple femtosecond laser beams. Collinear femtosecond laser beams with different wavefront curvature were incident on an objective lens and focused at different depths below the surface of silica glass. Hence multiple focal points exist in the glass simultaneously and parallel writing on multiple layers is realized. By adjusting

the beam wavefront, the layer distance and the layer alignment can be changed. Our parallel writing method is useful to shorten the fabrication time of femtosecond laser direct writing.
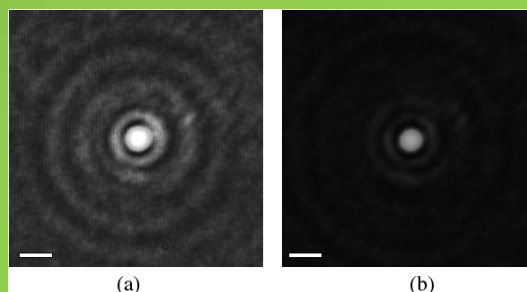
图 6 菲涅尔波带片主焦点。(a) 双层波带片 （b）单层波带片
Fig. 6. Photoghraphs of the main focal point: (a) two-layer zone plates, (b) single-layer zone plates. The length of the bars in the photographs is 20 μm.

在亚波长狭缝增强透射理论机制问题研究中，我们讨论了狭缝深度（薄膜厚度）和凹槽深度对增强透射的影响。随着狭缝深度和凹槽深度的增加，透射率呈现周期变化，我们用类法布里-波罗共振理论解释这一现象。另外，狭缝及凹槽内部的场分布表现了同样的周期关系，这也验证了我们的假设。

We studied the effects of the slit depth (i.e. film thickness) and the groove depth on the enhanced transmission through the subwavelength slit. The transmission varies periodically as the slit depth and the groove depth increase. We employed a Fabry-Perot like resonance effect to explain this. The field distributions in the slit and the grooves present a similar periodical variation, which confirm our supposition of the Fabry-Perot resonance.

通过在亚波长小孔中设置两个相对的齿状结构或在孔中心放置条状结构，可以使小孔的近场透射获得强烈增强。这种增强效应是由于孔内结构激发的局域化表面等离激元共振引起的。这两种小孔的增强透射有很强的偏振依赖关系，只有特定偏振才能得到增强透射峰。我们设计了四次旋转对称的亚波长小孔，也就是孔内有四个齿状结构和孔中心的十字结构，这两种小孔成功实现了不依赖入射偏振的增强透射，其透射率在任

何偏振角度都相等。这些结果，对亚波长小孔在近场成像等方面的应用具有一定价值，特别是其偏振特性，可以实现偏振选择器件或设计不受偏振影响的光学器件。
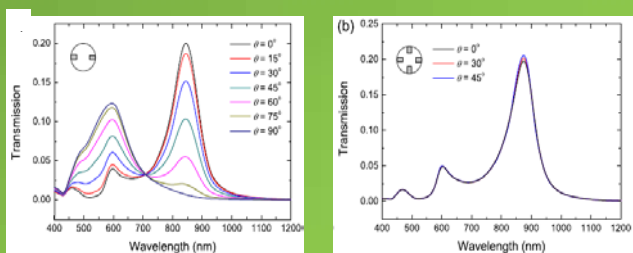
图 7 不同偏振角度下双孔(a)和四孔(b)透射光谱
Fig. 7 Transmission spectra of (a) the tooth-hole for different polarization angles and (b) four-tooth-hole for θ = 0°, 30°, and 45° respectively.

By setting some effective structures, a rod or two teeth in the holes, the near-field transmission of the holes can be extraordinarily enhanced. We attribute this enhancement to the localized surface plasmon excited by the rod and the teeth. The enhanced transmission of the rod-hole and the tooth-hole exhibits very strong polarization dependence, which is determined by the property of the localized surface plasmon directly. Starting from a basic optical theory, we find a simple way to design some polarization independent structures, i.e. cross-hole and four-tooth-hole. The spectra of these two holes for different polarization angles almost overlap together. These results may be useful for some polarization dependence and independence applications.

光子学材料及先进制备技术/ Photonics Materials and Advanced Fabrication Techniques

负责人：孔勇发

本方向涉及功能光学晶体、微晶玻璃陶瓷、光子学微结构、纳米光子学、低维功能材料等方面。本年度发表论文13篇，申请发明专利3项，获得授权专利4项，在研课题经费423.8万元。取得的代表性成果如下：

In this field, we mainly focused on the functional optical crystals, micro-crystal glass ceramics, photonic microstructure, nano-photonics, and nano-particulate films. 13 papers were published in international academic journals, 3 patents applicanted, and 4 patents issued. The total researching founds are more than 4 millions. This year, we obtained some important results, they are mainly shown as following:

铁锰双掺铌酸锂(LN:Fe,Mn)晶体被认为是实现非挥发全息存储的理想材料(Nature 393, 665 (1998))，但是该材料的响应时间在分钟量级，显然不能满足实际需求。本年度我们设计生长了锆铁锰三掺铌酸锂晶体(LN:Zr,Fe,Mn)，锆的掺入消除了反位铌缺陷，从而大大提高了载流子的迁移速度。LN:Zr,Fe,Mn 晶体非挥发存储的响应时间缩短至 0.95s（波长 532nm，光强 400 mW/cm^2），灵敏度达到 1.31 cm/J。该研究结果表明锆铁锰三掺铌酸锂晶体一种理想的全息存储介质。

Iron and manganese doubly doped LiNbO$_3$ (LN:Fe,Mn) has been suggested for non-volatile photorefractive recording (Nature 393, 665 (1998)), however its response time is still in the order of minutes. Here we present results on LiNbO$_3$ triply doped with zirconium, iron, and manganese (LN:Zr,Fe,Mn). The co-doping with Zr eliminates undesirable intrinsic traps, which strongly enhances the charge transition speed. The response time of LN:Zr,Fe,Mn for nonvolatile holographic storage shortens to only 0.95 s (wavelength 532 nm, intensity 400 mW/cm^2), and the sensitivity reaches 1.31 cm/J. Thus it seems that we have found an excellent recording medium for practical holographic storage devices.
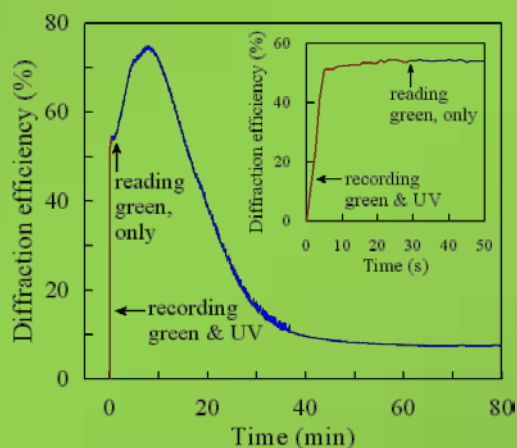
Fig. 1. Holographic recording and fixing characteristics of LN:Zr,Fe,Mn. Recording time is 30 seconds, readout time is about 80 minutes. The inset shows the recording process (0 s to 30 s)

图 1. LN:Zr,Fe,Mn 晶体中双色全息存储的记录和读出曲线。记录时间 30 秒，读出时间约 80 分钟。内图为细化的记录过程（0 至 30 秒）。

利用聚焦的 514.5 nm 激光，我们研究了掺镁、掺锆及名义纯铌酸锂晶体的光致畴反转。实验中发现这些晶体的组分虽然不同，但光致畴反转电场的降低却大致相同，约为 3 kV/mm。同时，反转畴总是在晶体–c 面的光照区成核，但在晶体的+c 面却是光照区的边沿首先贯通。实验中还发现施加反向电场，或者对晶体进行温度高达 600°C 的热处理，光致反转畴均保持稳定。综合上述及前人的实验现象，我们提出了光致畴反转的理论模型（如图 2）。

Light-induced domain reversal of Mg-doped, Zr-doped, and nominally pure LiNbO$_3$ crystals were investigated with focused 514.5 nm laser beams. It was found the light-reduced values of electric field for domain reversal are almost the same, about 3 kV/mm. Inverted domains always first nucleate on the –c surface within the illuminated region but appear at the edge of the spot on the +c surface. The light-induced inverted domains are hard to be reversed by application of a reverse electric field or by heating to temperatures as high as 600°C.

According to these experimental results, we present a qualitative model (as shown in Fig. 2) on the light-induced domain reversal process in LiNbO₃.

- ● hole
- ▬ light irradiation
- ↑ polarization
- ⊖ electron
- ↑↑↑ electric field
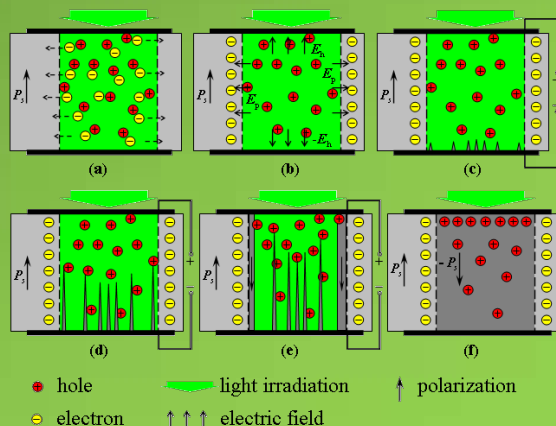
Fig. 2. The six stages of domain kinetics during light induced domain reversal. (a) Light induced charge carriers. (b) Electrons drift to the un-irradiation region and the left holes create opposite electric field under +c and –c surfaces. (c) Domain nucleation at the –c surface with the applied external electric field. (d) Domain tips propagation toward the +c face and holes drift along with these tips for electric neutralization. (e) The domain tips near the edge of illuminated region firstly arrive at +c surface. (f) The light induced domain reversal completed after small domains drift transversely and coalescence.

图 2.光致畴反转过程的六个阶段。(a)光激载流子产生。(b)电子迁移至暗光区，剩余的空穴在±c 表面附近形成方向相反的净电场。(c)在外电场作用下—c 表面首先成核。(d)反转畴的尖端向+c 表面生长，畴壁稳定的电中性要求空穴随反转畴尖端向前推进。(e)光照区边缘处的反转畴首先贯通晶体。(f)贯通的反转畴横向扩张生长、合并，完成光致畴反转过程。

利用光诱导极化反转技术，在近化学计量比掺镁铌酸锂晶体中实现了高质量畴结构的周期极化反转（Fig. 3）。对近化学计量比掺锆铌酸锂晶体的抗光损伤强度进行了研究，研究结果发现其在 1064nm（10ns）波长下可达到 2 J/cm² 以上（此时铌酸锂样品未出现"灰迹"现象，透射的倍频光斑未发生形变）。同时，经实验测量表明，该晶体在可见光区域其抗光损伤强度达到 10 MW/cm²（@532nm）以上。因此，近化学计量比掺锆铌酸锂晶体有可能成为优秀的准相位匹配材料。

We processed the high-quality domain structure on the near-stoichiometric Zirconium doped lithium niobate crystals with the technique of *Light-assisted Poling* (LAP) (Fig. 3). We studied the resistant photorefraction of the near-stoichiometric Zirconium doped lithium niobate crystals, and found that the resistance intensity of "Optical damage" is beyond the 2 J/cm² (1064nm, 10ns), at which no "gray trace" happened and the spot of transmitted light doesn't distort. Meanwhile, the resistant intensity of "Optical damage" in the range of visible light exceeds 10 MW/cm² at the wavelength of 532 nm. Therefore, the near-stoichiometric Zirconium doped lithium niobate crystals will become the excellent QPM materials in the visible range.
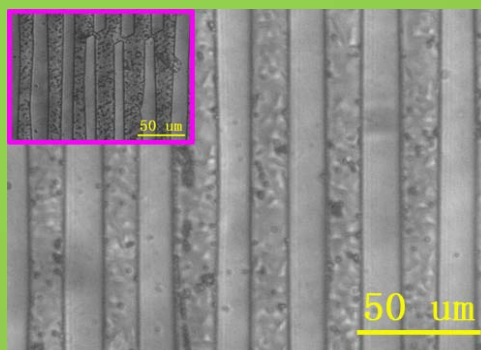
Fig. 3. Microscopic image of the +z face of a light-assisted periodically poled structure in a crystal doped with 1.0 mol% magnesium after wet etching in hydrofluoric acid. The inset image is the periodically poled structure without UV illumination.

图 3. 光辅助周期极化的 +z 面腐蚀图。内图是无紫外光照条件下的周期极化结构腐蚀图。

首次生长出环式 CsLaP₄O₁₂ 晶体并确定其晶体结构。CsLaP₄O₁₂ 单晶通过高温溶液缓冷法获得。X 射线单晶结构分析表明，该晶体属于 $I\bar{4}3d$ 空间群，晶胞参数为 a = 15.3443(13)Å，Z = 12。晶体结构由通过 LaO₈ 和 CsO₁₂ 多面体相互连接的 P₄O₁₂ 环堆积而成（图 4），该环具有 $\bar{4}$ 对称性。同时对 CsLaP₄O₁₂ 的红外光谱表征分析，发现其 ν_s(P —O—P)峰位与同质异构的链状化合物有显著差异；热分析研究结果表明，该化合物非同成分熔融，在 884°C 发生热分解。CsLaP₄O₁₂ 具有作为激光基质材料的两点结构特征：La³⁺离子周围环境不具有对称中心，有利于辐射跃迁；LaO₈ 多面体之间是"分离"的，易于减少浓度焠灭。La³⁺易被其它稀土激活离子取代，同时该晶体没有对称中心，而且其结构上的高对称性使晶体显现各向同性的性质，这将使该晶体在激光和非线性光学材

料领域具有潜在的应用价值。

Cesium lanthanum cyclic tetraphosphates ($CsLaP_4O_{12}$) crystal have been grown by spontaneous nucleation technique from high temperature solution and its crystal structure had been determined firstly. $CsLaP_4O_{12}$ belongs to $I\bar{4}3d$ space group, and its cell parameters are a = 15.3443(13)Å Z = 12. The crystal structure is characterized by $[P_4O_{12}]^{4-}$ rings connected by LaO_8 and CsO_{12} polyhedra. The $[P_4O_{12}]^{4-}$ rings have $\bar{4}$ symmetry. IR spectrum of $CsLaP_4O_{12}$ was studied. The results of DSC and DTA analysis showed that $CsLaP_4O_{12}$ melted incongruently. Materials for rare earth lasers should have two structural characteristics: first, they should have no local inversion symmetry about the La^{3+} ions so as not to decrease the probability of radiative transitions, and second, the La-O polyhedrons should be isolated among them so as to decrease the quenching fluorescence process of active ions. The structure of $CsLaP_4O_{12}$ satisfies both of these crystallographic conditions. $CsLaP_4O_{12}$ can be easily doped with any other lanthanide ions since the lanthanum has a high capacity to be substituted. $CsLaP_4O_{12}$ noncentrosymmetric crystal is isotropic by virtue of its symmetry and may combine luminescent and nonlinear optical properties.
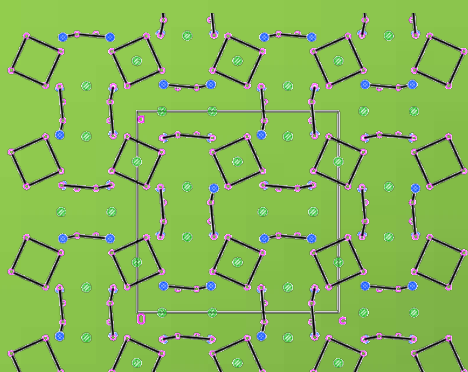
Fig. 4. Projection of the structure of $CsLaP_4O_{12}$ along [010] direction. Small open circles represent P atoms, large shaded circles represent La atoms, and large cross-hatched circles depict Cs atom. All O atoms are omitted.
图 4. $CsLaP_4O_{12}$ 沿[010]方向的晶胞堆积图。

对硼酸盐化合物 $NaSrB_5O_9$ 和 $Na_3SrB_5O_{10}$ 进行 Eu^{2+} 离子掺杂，研究其光致发光性质。并通过 Rietveld 结构精修分析其掺杂后的结构变化。研究中发现，两个五硼酸盐特殊的结构可以在无还原气氛的条件下，稳定部分 Eu^{2+} 离子，使其替代 Sr^{2+} 离子在晶格中的位置；同时存在部分 Eu^{3+} 离子的发光。不同的烧结条件，对于 Eu^{2+} 和 Eu^{3+} 的发光强度比有较大影响。对固熔体系列化合物 $NaSr_xBa_{4-x}B_3O_9$ 进行 Eu^{3+} 离子掺杂，发现在 x 不同的情况下，色度连续改变。以 $KSr_4(BO_3)_3$ 为基质，进行了 Eu^{3+}，Tb^{3+} 离子的掺杂，研究其发光性质。$KSr_4(BO_3)_3$：Eu^{3+}可实现有效的红光发射。用粉末从头算法对新化合物 $KMgBO_3$ 进行了结构解析，发现该化合物为非线性光学晶体，并且与 $NaMgBO_3$ 有一定的固熔度。此外，研究了 $K_{1-x}Na_xSr_4(BO_3)_3(0≤x≤0.5)$ 的晶体结构变化。

Photoluminescence of Eu^{2+} doped $NaSrB_5O_9$ and $Na_3SrB_5O_{10}$ were investigated, and the structures of the doped samples were refined by Rietveld method. It was found that the Eu^{2+} could be stabilized without reducing atmosphere because of the special structures of the two compounds, and the results of refinement showed that the Eu^{2+} occupied the Sr^{2+} positions. At the same time, some Eu^{3+} emissions could also be found in the PL patterns. The luminous intensities of Eu^{2+} and Eu^{3+} were infected quite a lot by the different anneal temperatures. Eu^{3+} doped solid solution compounds $NaSr_xBa_{4-x}B_3O_9$ were studied. It was found that the red color changed continuously with variable x values. The photoluminescence of Eu^{3+} and Tb^{3+} doped $KSr_4(BO_3)_3$ were investigated, and an effective red emission of $KSr_4(BO_3)_3$: Eu^{3+} was detected. The structure of $KMgBO_3$ was solved by SDPD (Structure Determination from Powder Diffractometry) method. It was found to be a nonlinear optical crystal, and patical soluble with $NaMgBO_3$. On the other hand, the structural changes of $K_{1-x}Na_xSr_4(BO_3)_3(0≤x≤0.5)$ were studied.

采用变温光致发光技术，研究了双层 InGaAs/GaAs 量子点层之间的能量转移。我们发现在 110 K 附近，沉积量较大的量子点层的光致发光异常增强现象。该现象可以通

过考虑在较高温度下通过浸润层态双层量子点之间的共振能量转移来解释。

The abnormal enhancement of the photoluminescence of the QDs in the layer with a larger amount of coverage at 110K is observed, which can be explained by considering the resonant Forster energy transfer between the wetting layer states at elevated temperatures.

采用溶胶-凝胶技术，结合阶段升温烧结方法，制备出一系列 Sn^{4+} 掺杂 TiO_2 纳米粒子。采用XRD、XPS和TEM等测试技术，研究了 Sn^{4+} 离子存在的状态、掺杂方式，Sn^{4+} 掺杂 TiO_2 的组分和相变过程。

Sn^{4+}-doped TiO_2 nanoparticles have been prepared by sol-gel method and annealed at different temperatures. Doping mode and existing states of Sn^{4+} dopants as well as the constituents and phase transition of the resultant nanoparticles have been investigated by X-ray diffraction, X-ray photoelectron spectroscopy, and high resolution transmission electron microscopy techniques.
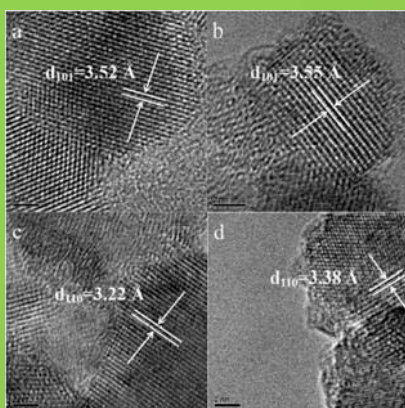
Fig. 5. HRTEM images of (a) TiO_2 and (b−d) Sn doped TiO_2.
图 5. TiO_2 (a) 与 Sn 掺杂 TiO_2 (b-d)的 HRTEM 照片。

采用溶胶-凝胶法，制备出不同掺杂浓度的 In 离子掺杂 TiO_2 纳米粒子。研究发现，In 离子掺杂在 TiO_2 纳米粒子表面形成 O-In-Clx 物种，该物种的表面态能级在 TiO_2 导带下 0.3 eV，TiO_2 价带到 O-In-Clx 物种的表面态能级的跃迁产生可见光响应，由于 O-In-Clx 物种的表面态能级的存在，促进了光生载流子的分离，导致了可见光活性的提高。

TiO_2 doped by different contents of indium was prepared by the sol-gel method It was revealed that a unique chemical species, O-In-Clx, existed on the surface of the indium doped TiO_2. The surface state energy level attributed to the surface O-In-Clx species was located at 0.3 eV below the conduction band of TiO_2. The transition of electrons from the valence band of TiO_2 to the surface state energy level was responsive to visible light. The photogenerated carriers generated under visible light irradiation can be efficiently separated by the surface state energy level of the O-In-Clx species and the valence band of TiO_2 to contribute to the photocatalytic reaction. Consequently, the indium doped TiO_2 showed improved photocatalytic activity for photodegradation of 4-chlorophenol compared to pure TiO_2 under visible light irradiation.
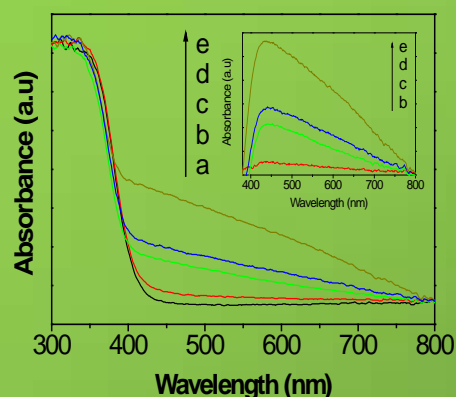
Fig. 6. Diffuse reflectance UV-visible spectra of pure TiO_2 (a), TiO_2-In3% (b), TiO_2-In7% (c), TiO_2-In10% (d) and TiO_2-In15% (e). The insert gives the difference DRS spectra of TiO_2-Inx% (curve b-e).
图 6. 未掺杂 TiO2 (a)、TiO_2-In3% (b)、TiO_2-In7% (c)、TiO_2-In10% (d) 与 TiO_2-In15% (e)的漫反射紫外—可见光谱。内图为 TiO_2-Inx% (曲线 b-e)的 DRS 差值谱。

采用磁控溅射法，制备出一组金红石/锐钛矿混晶结构的纳米 TiO_2 薄膜催化剂。光催化实验证明，随着催化剂中金红石含量减少，催化剂的光催化活性逐渐提高。 XRD、XPS、SPS谱和AFM结果表明，催化剂随着金红石含量减少，表面羟基(OH)和桥氧(-O-)的含量逐渐增加，费米能级提高 导致了 TiO_2/H_2O 界面 TiO_2 表面带弯增大，有利于光生载流子的分离，使光催化活性有效地提高。

A group of nano-TiO_2 film catalysts with rutile/anatase mixed crystal structures were prepared by a magnetron sputtering method. The

photodegradation of phenol was employed to evaluate the photocatalytic activities of the film catalysts. With less rutile content the amount of hydroxyl groups (OH) and bridging oxygen atoms (-O-) on the surfaces of catalysts increase gradually and the Fermi levels gradually shift upwards as well. because of the shifting of the Fermi level, the surface band bending of TiO_2 at the interface of TiO_2/H_2O is enhanced leading to an increase in the charge carrier separation and an improvement in the photocatalytic activity.

under visible light. Based on XRD, XPS and SPS, it can be inferred that when the doped content is low, the indium ion substitutes Ti into the TiO_2 lattice forming the $In_xTi_{1-x}O_2$ structure and the In doped energy-band narrows the band gap by mixing with Ti 3d states. With increasing the doped content, In_2O_3 comes up on the surface of $In_xTi_{1-x}O_2$ nanotubes to form the $In_xTi_{1-x}O_2/In_2O_3$ composite structure. This composite structure efficiently enhances promotes photogenerated carriers separation and increases the utilization of photogenerated carriers in photocatalytic reactions at the solid/liquid interface, resulting in the higher photocatalytic activity under visible light.

Fig. 7. AFM images of samples A1-A4
图 7. A1-A4 样品的 AFM 照片。
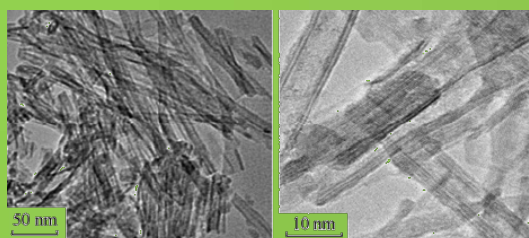
Fig. 8. TEM images of the pure TiO_2 nanotube and In doped TiO_2 nanotube
图 8. 未掺杂 TiO_2 纳米管与 In 掺杂 TiO_2 纳米管的 TEM 照片。

采用两步预掺杂方法，制备出In 离子掺杂二氧化钛纳米管可见光催化剂。可见光催化实验证明：掺In离子量为3%的TiO_2纳米管可见光活性是纯TiO_2纳米管的2倍以上。XRD，XPS and SPS表征结果表明：当In离子掺杂浓度较小时，In离子以取代式掺杂方式存在，形成$In_xTi_{1-x}O_2$结构。In离子的掺杂能级与Ti 离子的3d 轨道形成混合价带，使禁带宽度变窄，增强了可见光响应。随着In 离子掺杂浓度的增加，在In离子掺杂的TiO_2纳米管表面生成$In_xTi_{1-x}O_2/In_2O_3$的复合结构，促进了光生载流子的分离，提高了光生载流子参加光催化反应的利用率，使纳米管催化剂可见光催化活性显著提高。

Indium doped TiO_2 nanotubes were fabricated by a two-step pre-doping method. It was found that the TiO_2 nanotubes with indium doped content at 3% exhibited the best photocatalytic activity being over twice as much as that of pure TiO_2 nanotubes on the photocatalytic degradation of 4-chlorophenol

采用溶胶-凝胶法，制备出Zr 离子掺杂TiO_2 光催化剂。光催化实验表明，Zr 离子掺杂浓度为10%时光催化活性最高，其紫外光、可见光催化活性分别是纯TiO_2 的1.5 和4 倍。XRD, XPS, UV-Vis DRS, PL 等表征结果表明，Zr 离子以取代式掺杂方式进入TiO_2晶格，在TiO_2导带下方0.3 eV形成Zr 离子掺杂能级，增强了可见光响应，促进了光生载流子的分离，从而使Zr离子掺杂TiO_2 的紫外、可见光催化活性显著提高。

TiO_2 photocatalysts doped by different contents of zirconium ions were prepared by a sol-gel method. The experiments of 4-chlorophenol photocatalytic degradation showed that the TiO_2 with zirconium doped content at 10% exhibited the best photocatalytic activity. Its photocatalytic efficiency is 1.5 and 4 times as high as that of pure TiO_2 under ultraviolet and visible light. The samples were characterized by XRD, XPS, UV-Vis DRS and PL. It was revealed that zirconium ions substituted

the lattice titanium ions in TiO$_2$ lattice. And thus, the doping energy level attributed to the zirconium dopant was located at 0.3 eV below the conduction band of TiO$_2$, which enhanced the response to the visible light and accelerated the separation of photogenerated carries. Consequently, the zirconium doped TiO$_2$ showed improved photocatalytic activity for photodegradation of 4-chlorophenol compared to pure TiO$_2$ under both UV and visible light irradiation.

以 ZnO 纳米柱阵列为模板,采用溶胶-凝胶法,制备出 TiO$_2$/ZnO 和 N 掺杂 TiO$_2$/ZnO 复合纳米管阵列。SEM、UV-Vis、and XPS 表征结果表明, 两种阵列的纳米管均为六角形结构(直径约为 100nm, 壁厚约为 20nm)。在 N-TiO$_2$/ZnO 样品中, 掺入的 N 离子主要是以 N-Ox、N-C 和 N-N 物种的形式化学吸附在纳米管表面, 仅有少量的 N 离子以取代式掺杂的方式占据 TiO$_2$ 晶格 O 的位置。N 物种的取代式掺杂导致带隙的窄化,增强了纳米管阵列光的吸收效率, 促进了光生载流子的分离, 因此, 与 TiO$_2$/ZnO 复合纳米管阵列相比,

N-TiO$_2$/ZnO 复合纳米管阵列光催化活性得到了提高。

TiO$_2$/ZnO and N-doped TiO$_2$/ZnO composite nanotube arrays were synthesized by sol-gel method using ZnO nanorod arrays as template. SEM, UV-Vis, and XPS were used to characterize the samples. The nanotubes showed a uniform hexagonal shape. The diameter and wall thickness of the nanotubes were about 100 nm and 20 nm, respectively. Some N dopants were substitutionally doped into the TiO$_2$/ZnO lattice, while the majorities, such as N-O$_x$, N-C and N-N species were chemically absorbed on the surface of TiO$_2$/ZnO composite nanotubes. The dopant-induced narrow of the band gap is due to the doping of N ions in the TiO$_2$ lattices which enhance the visible-light response and promote the separation of photogenerated carriers. Compared with the TiO$_2$/ZnO composite nanotube arrays, N-TiO$_2$/ZnO composite nanotube arrays exhibited a higher photocatalytic activity.
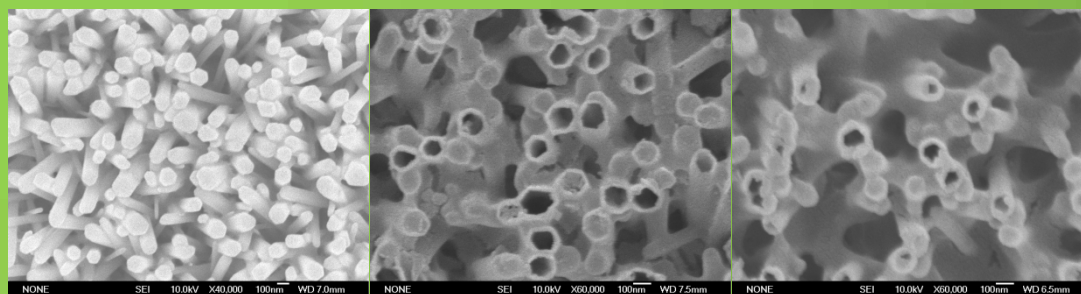
Fig. 9. SEM images of the ZnO nanorod arrays (a), TiO$_2$/ZnO composite nanotube arrays (b) and the N-TiO$_2$/ZnO composite doped TiO$_2$ nanotube arrays (c) respectively. The inset of Fig. 1a shows the XRD pattern of ZnO nanorod arrays.

图 9. ZnO 纳米棒阵列 (a)、TiO$_2$/ZnO 复合纳米管阵列 (b)与 N-TiO$_2$/ZnO 复合掺杂 TiO$_2$ 纳米管阵列 (c)的 SEM 照片。

弱光非线性及量子相干光学/ Weak Light Nonlinear Optics and Quantum Coherent Optics

负责人：许京军

本方向主要开展微/纳结构制备、微/纳非线性光调控、量子非线性光学与调控、飞秒超快探测技术以及光折变材料与新效应等方面的研究。2009 年度本方向共发表论文 25 篇，主要取得如下进展：

The main research topics in this group are fabrication of micro/nano-structure, nonlinear optical manipulation in micro/nano-structure, quantum nonlinear optics, ultrafast detection and analysis by using fs technology and photorefractive nonlinear optics. We published 25 papers in various academic Journals. The main research progresses in 2009 are as follows.

我们在掺杂 Pr^{3+} 离子的 Y_2SiO_5 晶体中实现了电磁感应透明效应，将光脉冲存储在晶体中并读取出来。我们发现光脉冲的存储与读出过程存在由位相匹配条件引起的高度角度选择特性。为此我们引入了基于电磁感应透明效应的角度复用技术，并实现了一个可寻址的双通道缓存器，在光脉冲读取过程中两个通道之间不存在串扰。如图 1 所示。这项技术不仅增大了量子存储的存储容量，
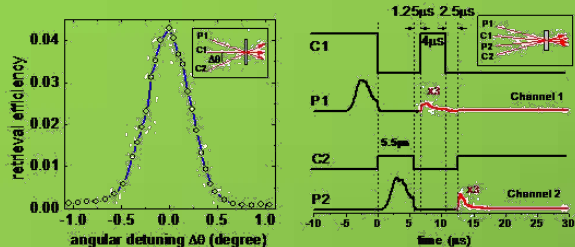
图 1 （左）读出效率和耦合光 C1 与读取光 C2 之间的夹角 Δθ 的关系图。当读取光 C2 和耦合光 C1 共线时读出效率达到最大值。P1 为要存储的光脉冲。（右）基于角度复用的可寻址光缓存。两个光脉冲（P1、P2）在被存储到晶体之后可以被 C1 和 C2 分别读取出来，并且两个通道之间没有串扰。

Fig.1 (Left) Retrieval efficiency versus the angular detuning Δθ between the retrieval beam C2 and the storage coupling beam C1 shown in the inset. The efficiency reaches maximum when C2 propagates collinearly with C1. P1 was the pulse to be stored. (Right) Addressable optical buffer memory based on angular multiplexing. Two pulses (P1, P2) can be selectively readout without crosstalk by C1 and C2, respectively, after they were stored into the crystal.

而且使得可寻址多通道缓存成为可能。

Electromagnetically induced transparency (EIT) was implemented in Pr^{3+} doped Y_2SiO_5 crystal, and light pulse was stored in the crystal and retrieved thereafter. We found that the retrieval efficiency is of high angular selectivity during the readout process. Based on this angular selectivity, we introduced angular multiplexing in light pulses storage. A multi-channel buffer memory and addressable all-optical routing without cross-talk between neighboring channels were demonstrated by selectively reading out the pulses. This technique enables one to increase the storage capacity and to selectively route the pulses in parallel and in an addressable way.
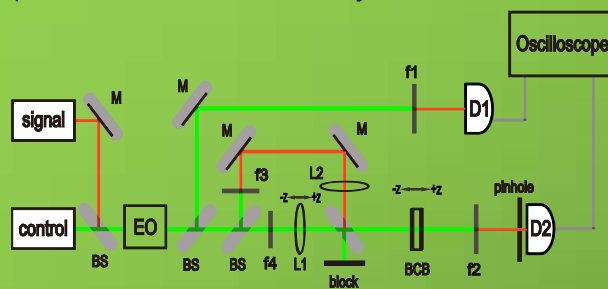
图 2. 实验装置示意图。 BS：分光棱镜。M：反射镜，EO：电光调制器，f1, f2, f3, f4：785nm 以及 532nm 带通滤波器，D1 和 D2：探测器。

Fig. 2. The experimental setup. BS: beam splitter, M: mirror, EO: electro-optic modulator, f1, f2, f3, f4: band- pass filter used to select component at 785 nm or 532 nm, D1 and D2: photo-detectors.

通过使用一个特定波长的控制光，我们在 BCB 聚合物介质中实现了一个可以对任意波长信号光进行群速调控的新方法，如图 2 所示。该方法去除了对于信号光光学非线性或共振响应等的要求，并且通过采用特定波长的控制光易于达到较强的光学非线性效应，从而产生更显著的慢光或者快光效应。

We proposed a new method to generate slow and fast lights at arbitrary signal wavelength in benzocyclobutene (BCB) polymer with the help of a control beam (see Fig. 2). This method, to actively and chromatically control the group velocity of light, eliminates the requirements on the optical nonlinearity or resonance at the signal wavelength,

while it is much easier to have very strong optical nonlinearity at a specific control wavelength, therefore to generate efficient slow and fast lights.

我们发现通过改变 BCB 样品沿光传播方向上相对于聚焦信号光束腰的位置可以精确调节信号光的群速度大小以及正负，如图 3(a)。另外，还可以通过控制 BCB 样品上的控制光，即控制信号光所感受到的折射率变化大小来调节信号光群速度的大小，如图 3(b)所示。该方法实现了主动式任意波长的群速调控，因此在光纤通信网络以及光信息处理等领域具有潜在的实际应用价值。

We found that the signal group velocity can be precisely tuned simply by scanning the position of the BCB sample along the light propagation direction. Another advantage is the ability to control chromatically the group velocity of the signal beam by adjusting the control beam in the BCB sample, which, in essence, is to control the refractive index change experienced by the signal beam. This method provides an active chromatic control on the group velocity of light at arbitrary signal wavelength and therefore may have important potential applications in optical communication network and optical information processing.
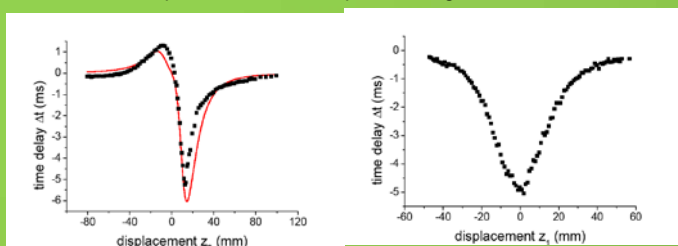
图 3. 时延 Δt 随样品位置 z_2（相对于聚焦信号光束腰，图 a）以及 z_1（即通过控制光改变信号光感受到的折射率变化，图 b）的变化曲线。红线为理论拟合曲线。

Fig.3. Time delay Δt versus the sample position displacement z_2 (with respect to the focused signal beam waist, a) and z_1 (that is to adjust the control beam to control the refractive index experienced by the signal beam, b). The red solid curve is the theoretical fit.

我们使用光感应方法在具有饱和自散焦非线性的掺铁铌酸锂晶体中制作了大面积弱调制二维光子晶格薄板。在这种光子晶格薄板中，实验观察到了光束的线性和非线性离散传输现象。实验结果表明弱调制二维光子晶格薄板支持布拉格衍射、离散衍射，

并在适当条件下可以支持空间离散孤子的形成，如图 4 所示。研究结果表明，由于晶格中临近有效波导间的强烈的能量泄露导致离散孤子的形成需要较高的光学非线性作用。我们的数值模拟结果和实验结果符合得很好。
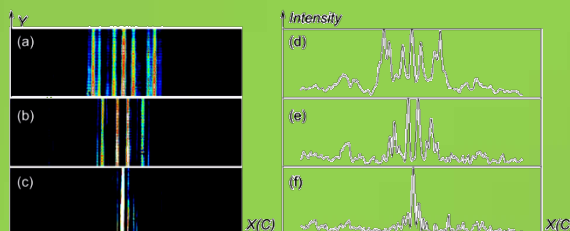
图 4. 在不同辐照时刻，二维光子晶格薄板出射面上探测光光强分布图样（左列）和其相对应的强度分布曲线（右列）。

Fig.4. The intensity distribution images (left column) and the corresponding intensity distribution profiles (right column) on the output X-Y surface of the 2D photonic lattice slab at different exposure time t when a He-Ne probe laser beam was coupled into one backbone waveguide. The exposure time of the probe beam was t = 0 minutes for (a) and (d), t = 200 minutes for (b) and (e), and t = 530 minutes for (c) and (f), respectively.

We fabricated large-area weakly modulated two-dimensional photonic lattice slabs using the optical induction method in LiNbO$_3$:Fe crystal exhibiting a saturable self-defocusing nonlinearity. We observed experimentally the linear and nonlinear discrete light propagation dynamics in such a photonic lattice slab. The experimental results show that the weakly modulated two-dimensional photonic lattice slab supports the Bragg-matched light diffraction, the discrete light diffraction, and the formation of discrete optical spatial soliton under appropriate conditions, as shown in Fig. 4. However, stronger optical nonlinearity is required to form a discrete soliton due to the stronger energy leakage between the adjacent effective waveguides in the lattice slab. Our numerical simulations are in good agreement with our experimental observations.

我们发展了一种有效的理论方法,即通过调节二维砷化镓光子晶体薄板结构参数将光子晶体泄漏本征模式调控到特定的光谱位置。利用这一方法，我们得到了光子晶体泄漏模式波长位于 1492 nm 和 1519 nm 处时的薄板结构参数，如图 5 所示。这两个波

长与掺铒富勒烯的吸收和发射波长相重合，可实现位于光子晶体薄板表面的掺铒富勒烯的荧光发射增强。这一方法可以推广到其他的荧光发射材料如掺杂量子点和碳纳米管，用以增强它们的荧光发射功率，在量子信息处理和高灵敏度探测方面有重要应用。

We developed an effective way to engineer a two-dimensional (2D) GaAs photonic crystal slab (PCS) with its leaky eigenmodes at desired wavelengths by investigating its spectral dispersion, particularly in terms of transmission efficiency spectra at different launch angles of the light beam. Structural parameters for the photonic crystal slab with leaky eigenmode wavelengths at both 1492 nm and 1519 nm are obtained, as shown in Fig. 5, which overlap with the absorption and luminescence spectra of erbium-doped trinitride-template fullerenes ($Er_3N@C_{80}$). This may lead to the enhanced luminescence from $Er_3N@C_{80}$ on the surface of the photonic crystal slabs. This can be very useful in enhancing the fluorescence emission efficiency of fluorescent species such as ion-doped fullerenes, quantum dots and carbon nanotubes on the PCS surface by overlapping the fluorescence spectra with the leaky modes, which may have great potential applications in quantum information processing and high sensitivity sensors.

(a)   (b)
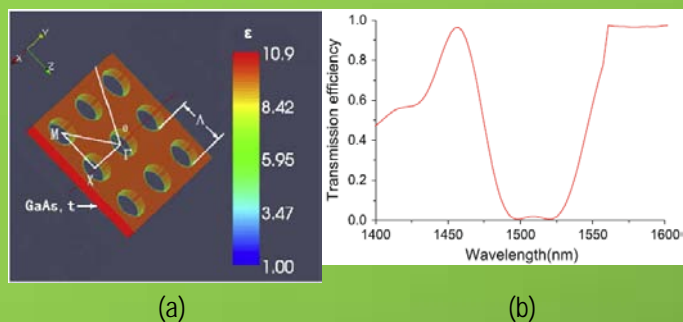
图5. (a) 二维砷化镓光子晶体薄板结构。(b) 在正入射条件下，当光子晶体薄板的结构参数r = 233.4 nm和t = 301.5 nm时的透射谱，可以看到其泄漏本征模式波长分别位于1497.25 nm和1519.55 nm，和设计目标波长符合得相当好。
Fig. 5 (a) Structure scheme of 2D PLS. (b) Transmission efficiency of the photonic lattice slab versus wavelength at normal incidence with r = 233.4 nm and t = 301.5 nm. The leaky modes are found to be at 1497.25 nm and 1519.55 nm, respectively, which is in good agreement with the target wavelengths.

通过研究掺 R6G 的 PMMA 中的类非简并二波耦合群速调控，我们得到了-5.1m/s 及

9.19m/s 的超快光和超光慢。研究一方面证明了掺 R6G 的 PMMA 可以作为红宝石样品的廉价替代品实现群速调控；另一方面，在掺 R6G 的 PMMA 和纯 PMMA 中观测非简并二波耦合和群速调控的对照实验也间接证明了我们先前的假设：即在存在非简并二波耦合效应的介质中，可以通过类非简并二波耦合效应来调控群速。
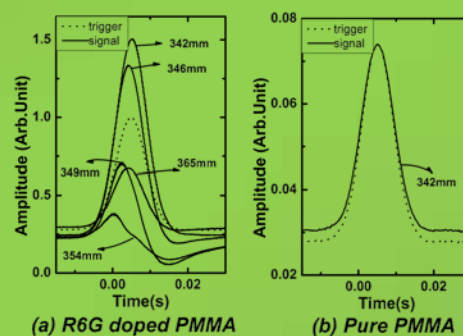
图6. 样品处在不同位置时的脉冲延迟。(a)图中是掺杂PMMA的数据，(b)图中是纯PMMA样品的数据。
Fig.6 Temporal profiles of the transmitted paraxial pulses with different Zs in pure PMMA and R6G-doped PMMA. (a) is the result in the doped PMMA and (b) is the result in the pure one.

The typical superluminal result of -5.1m/s and the subluminal result of 9.19 m/s was achieved in the R6G doped PMMA via non-degenerate two-wave coupling like mechanism (NDTWC-like mechanism), respectively. The result provides a cheap substitution of ruby to control the group velocity via NDTWC-like mechanism. At the same time, the experiment together with the non-degenerate two-wave coupling (NDTWC) experiment in the doped and pure PMMA provides the proof of our former conclusion that NDTWC-like mechanism could be used to change the group velocity of the paraxial part of a focused TEM_{00} beam in materials with NDTWC process.

光诱导类离子光学晶格中新颖孤子态研究
Novel solitons in an optically induced 2D ionic-type lattice

a)   光在周期性微结构中的非线性传输存在许多有趣的现象和潜在的应用，其中包括多种空间晶格孤子。一般地，晶格孤子的形成要么利用单一的自聚焦非线性，要么利用单一的自散焦非线性，而最近的研究表明，

在非传统偏压条件下的光折变晶体中，存在一种特殊的混合非线性，它在不同的空间方向上同时存在自聚焦和自散焦非线性。依靠这种特殊的混合非线性效应，在同一光诱导光子晶格中，我们同时得到了利用不同非线性形成的孤子串。仅改变入射条形光束的空间取向，我们可以选择性地激发不同的带隙孤子或带内孤子。我们的实验和数值模拟都表明这种混合非线性（自聚焦和自散焦非线性共存）是选择激发不同带隙孤子或者不同带内孤子的关键，同时我们还首次观测到利用自聚焦非线性形成的带内孤子。相关结果发表在 Opt. Lett.上。
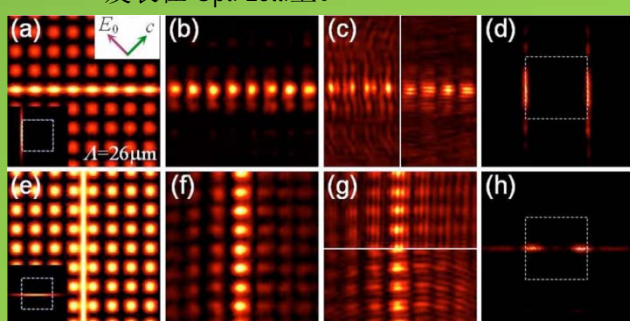
图 7 自聚焦（上排）和自散焦（下排）带内鞍点孤子的光学转换。从左到右依次为激发条件、孤子串光强分布，及其干涉图和空间频谱。
Fig.7 Experimental results of in-band soliton trains bifurcated from point X under self-focusing (a)–(d) and -defocusing (e)–(h) nonlinearity. From left to right, superimposed input intensity pattern of probe and lattice beams (insets show the spectra of probe beam excitation), output intensity pattern of the soliton trains, interferograms from two orthogonal directions, and soliton output spectra.

Wave propagation in optical periodic structures has been studied extensively, including various types of lattice solitons. In general, lattice solitons have been generated with either a self-focusing or defocusing nonlinearity, which in photorefractive (PR) materials was established simply by changing the polarity of the bias field. Recently, we demonstrated that in a nonconventionally biased (NCB) PR crystal self-focusing and -defocusing nonlinearities coexist, leading to unusual excitation of spatial solitons in the same nonlinear material. In this Letter, we demonstrate quasi-1D soliton trains in a new type of photonic lattice induced with periodic positive and negative index changes in a NCB PR crystal. Solely by changing the orientation of an input stripe

beam, selective excitation of the soliton trains arising from different gaps or within the continuum spectrum of the Bloch band is realized. We show that the self-focusing and –defocusing hybrid nonlinearity supported by the NCB condition is the key for in-band or in-gap soliton excitations and demonstrate for the first time to our knowledge the embedded solitons under a self-focusing nonlinearity.

b) 周期性光子晶格的正常（反常）衍射特性，可以利用自聚焦（自散焦）非线性与之平衡产生晶格孤子，而对于二维光子晶格的鞍形衍射关系（在不同的方向上同时具有正常衍射和反常衍射），用单一的非线性（自聚焦或自散焦）无法同时平衡两个方向上不同的衍射。在非传统偏压下的光折变晶体中，我们利用特殊的混合非线性与光诱导光子晶格中的鞍形衍射关系达到完美的平衡，产生了一种新颖的空间带隙孤子——鞍点孤子。这种孤子和以前发现的任何带隙孤子都不一样，它的相位结构接近带隙结构中第一带鞍点的布洛赫模式，同时它在傅立叶空间的频谱主要集中在第一布里渊区的两个 X 点上，所以它是由第一布洛赫带的鞍点分化出来的。另外，我们还观察到了不稳定的带内鞍点孤子。其结果发表在 Opt. Lett.上。

Despite the discovery of a variety of soliton entities in discrete systems, to our knowledge, it has not been possible to demonstrate a two-dimensional (2D) spatial soliton in a physical arrangement where an optical beam exhibits simultaneously normal and anomalous diffractions in different transverse directions. First, natural materials typically are not endowed with a saddle-shaped bi-diffractive property; second, it remains a challenge to find a nonlinear material that can support hybrid self-focusing and self-defocusing nonlinearities without changing experimental conditions. Previous work on nonlinear X waves and light bullets was aimed toward balancing of beam diffraction and pulse dispersion simultaneously, but in spatial domain alone compensation of normal and anomalous

diffractions in the same experimental setting has not been realized. In this Letter, we employ the hybrid nonlinearity to demonstrate a type of spatial gap solitons, namely, "saddle solitons," by balancing the saddle-shaped diffraction in an optically induced 2D ionic-type lattice. Such solitons have propagation constant residing in the Bragg reflection gap, but they differ from all previously observed solitons supported by a single self-focusing or self-defocusing nonlinearity. In addition, quasi-localized 2D in-band solitons are also identified, but they are not stable during propagation. Our theoretical analysis finds good agreement with experimental observations.

光诱导三维光学晶格及其离散衍射增强效益研究
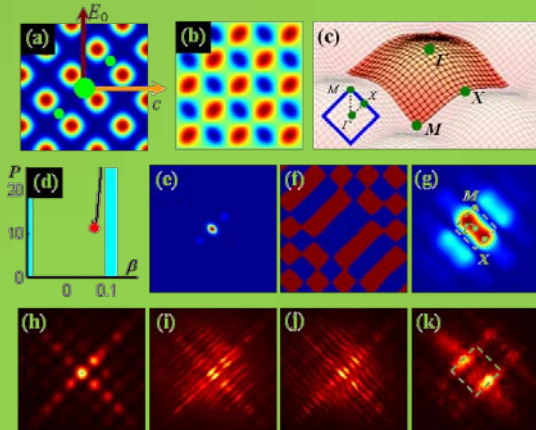
图8 (a) 周期光场; (b) 光子晶格; (c) 衍射关系; (d)鞍点孤子存在曲线; (e)-(g) (d) 中红点处孤子的强度、相位和频谱分布的模拟结果; (h-k) 鞍点孤子的实验结果, 依次对应孤子光强分布、与不同方向平面波的干涉图和空间频谱。

Fig.8 (Color online) (a) Orientations of crystalline c axis, bias field, and square lattice-inducing beam; (b) refractive index distribution of the induced ionic-type lattice; (c) extended first Bloch band; (d) Existence curve of saddle solitons at V0=0.94; (e)–(g) Intensity pattern (associated index change shown in insert), phase structure, and Fourier spectrum of the saddle soliton at the marked point in (d); The bottom row shows the (h) intensity pattern; (i), (j) interferograms with a tilted plane wave at two orthogonal directions; and (k) Fourier spectrum of the soliton.

在本项工作中我们利用光学诱导的方法在光折变体材料中成功制备出三维可调节光学晶格。如图9所示, 此结构是通过两束正交并垂直于晶体c轴的二维正方格点光束构成。并能通过改变外加电场方向得到自聚焦（图9b）或自散焦（图9c）非线性的三维光学晶格。合理调整光束的格点分布或是

外场还能实现六角或类离子结构的三维光学晶格。
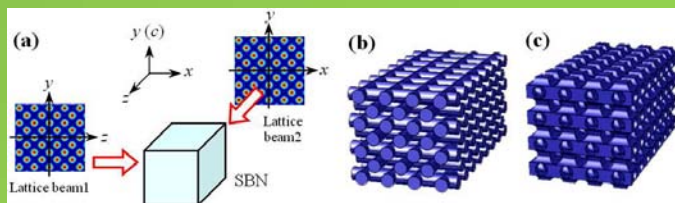
图9 (a)三维光学晶格配置图。在 SBN 晶体中沿两个垂直于晶体 c 轴的方向入射两束正交的二维正方格点光束。（b）、（c）分别对应自聚焦和自散焦非线性情况下的两种结构。

Fig.9 (a) Schematic drawing of the optical induction method for 3D photonic lattices. The photorefractive strontium barium niobate (SBN) crystal is a uniaxial crystal, with its crystalline c-axis oriented along y-direction. The two lattice-inducing beams are launched along two crystalline a-axes (oriented along x- and z-directions). (b, c) Illustration of induced lattice structures under self-focusing and self-defocusing nonlinearity, respectively.

通过在两个正交方向上对其导光和布利渊频谱的观测我们可以轻易的监视这种周期性结构。在观测同比与二维光学晶格离散衍射的实验过程中, 我们发现这种离散行为被很大程度上放大, 且和第三维度上的调制深度成正比。实验结果如图10所示。我们可以将这种衍射增强效应归结于横向耦合的增加, 这是由于纵向的波导通道被横向的通道所连接, 使得横向波导的耦合加大。它为全光路由以及方向可选性自陷提供新的解决思路。相应工作发表在Optics Express。
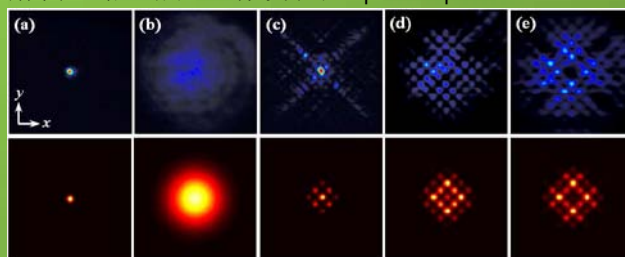
图10, 实验（顶行）和数值模拟（下行）三维光学晶格中衍射增强效益。（a）、（b）为无晶格情况下入射和出射图。（c）-（e）对应随纵向调制深度加强, 出射光斑的离散衍射图像。

Fig.10 Experimental observation (top) and numerical simulation (bottom) of diffraction enhancement in a 3D photonic lattice. (a, b) Input and output of a probe beam propagating along z-direction without lattice; (c-e) its output discrete diffraction patterns after propagating through the lattice when the intensity of the lattice-inducing beam along x-direction (see Fig. 1) is gradually increased.

缺陷光学晶格中的多色光子回路

在本工作中我们模拟斜入射光在线性

光学晶格缺陷通道中的导光和路由行为。同过合理设计我们可以得到L、T、+等形状的缺陷通道（Fig.11）。在进一步适度调节后我们横向上实现对导入光的一系列操控，如完全反射、阻断、分束、能量比可控的分流等。另外我们还利用有限波动阵列的边界模式，实现边界的"口"字型横向导光（Fig. 12）。最后在"L"型缺陷通道中实现多色光的缺陷导波(Fig. 13).
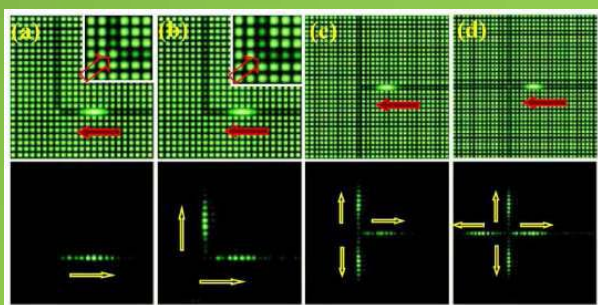
图 11.利用不同结构的线缺陷控制与操纵光束。顶行为具有线缺陷的晶格与向左倾斜的入射光，底行为出射光强分布. (a) 和 (b)分别为通过调节 L-型缺陷拐角处的波导折射率来达到阻塞光与50/50 分光。（c），(d)分别为 T-型 与 +型线缺陷的导光

Fig.11 Blocking and splitting of light with different designs of line defects. Top panels show lattice structures superimposed with a left-tilted probe beam at input; bottom panels show the probe beam exiting the lattice. (a) and (b) show examples of blocking and 50/50 splitting by adjusting the refractive index of the corner waveguide in L-defect to be 100% and 32.5% with respect to that in the uniform waveguide arrays, respectively. (c) and (d) show splitting of a light beam by T and + shaped line defects in the lattices.
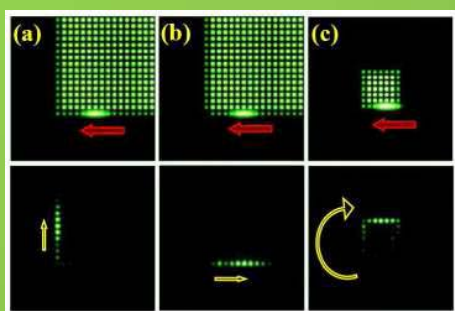
图 12 有限波导阵列表面线缺陷的导光。顶行表示的是光子晶格结构。底行表示的是出射光强分布。（a）转角线缺陷对光的操纵，（b）线缺陷转角处波导格点缺失对入射光的反射作用，（c）入射光在表面线缺陷上的环绕。

Fig.12 Routing of a light beam around the surface of finite waveguide arrays. Top panels show the lattice structures superimposed with a left-tilted probe beam at input; and bottom panels show the output of the probe beam. (a) Steering of the probe beam around a corner along surface line defects, (b) blocking when the defect at the corner is missing, and (c) spiraling around the surface of a finite waveguide arrays bounded by surface line defects.

这些结果将对低调制度微结构器件的发展产生有益的推动。此工作发表在Optics Express。
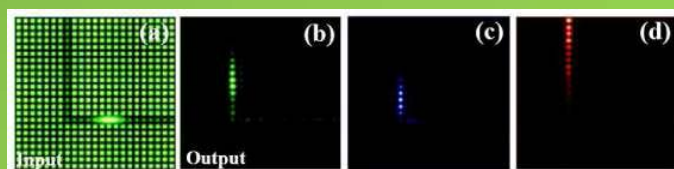
图 13 光子晶格中 L-型的线缺陷结构（a）对不同波长光的路由功能。(b-d)为不同波长的光出射图，波长分别为 532 nm, 488 nm, and 633 nm.

Fig.13 Routing of a light beam of different wavelengths in the same setting of L-shaped defect channel in lattice structure shown in (a). (b-d) show the output of the probe beam exiting the lattice. From (b) to (d), the wavelengths used are 532 nm, 488 nm, and 633 nm, respectively.

光致光学超晶格中的类Tamm和Shockly表面态研究
Tamm-like and Shockley-like surface states in optically induced photonic superlattices

在此项研究工作中,我们首次在光诱导的光学超晶格观测到表面类Shockley态。不同与半导体工艺制备的超晶格，光诱导超晶格微结构（Fig. 14）的耦合强弱是具有可控性的，通过合理的计算和控制能够轻易地调节其带隙结构特性，从而可支持不同的表面模式。相应工作发表在Optics Letters 和Phys. Rev. A上。

此外，我们还发现，通过调节表面缺陷
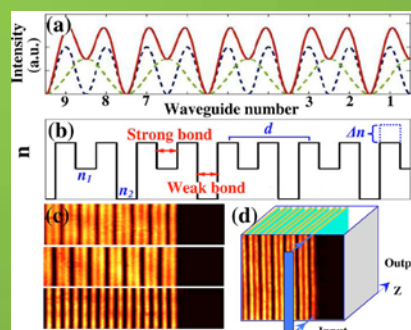
图14 (a)光子超晶格结构示意图（实线）是由两个不同周期的光强叠加而成（虚线）（b）理论计算中简化的光子超晶格的折射率模型，（c）光诱导光子晶格与连续介质的界面，具有强耦合（顶行）和弱耦合（中间）的超晶格表面，简单的超晶格（底行）表面；（d）入射光与界面的示意图。

Fig.14 (a) Intensity profiles used to create superlattice structures (solid curve) by superimposing two periodic patterns (dashed black and gray curves). (b) Simplified structure used in our theoretical model, where surface termination bond is located in the right end; denotes surface index perturbation, and d is the lattice period. (c) Transverse patterns of induced lattices with an interface between homogeneous medium (right black region) and an SL with either an SB (top) or a WB (middle) termination, or a simple lattice (bottom). (d) Schematic illustration of a probe beam aiming at the interface.

的调制度或是改变探测光的强度，可以实现表面类Tamm态和Shockley态之间的转换。只有当超晶格具有适合边界的时候，我们才能观测到表面Shockley态；而通过表面缺陷或

是探讨光非线性效益的显现还能将表面Shockley态（Fig.15b）转变为表面Tamm态（Fig. 15a、c）。特别值得指出的是，在不改变超晶格条件的情况下，我们观测到从线性表面Tamm态到线性表面Shockley态，再到非线性表面Tamm态演化过程。最后利用耦合模理论计算的结果和实验符合得相当完美。
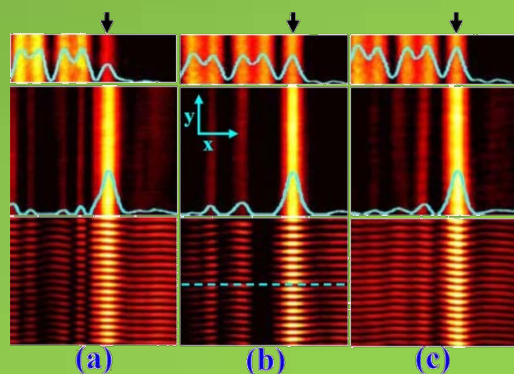
图15 从线性Tamm态到线性Shockley态再到非线性Tamm表面态转变的实验结果。探测光入射到超晶格的表面波导上。（a）负缺陷导致的线性Tamm态；（b）线性shockly态 （c）非线性诱导的正缺陷形成的非线性Tamm态；顶部两行为超晶格的强度分布与出射的光强。底行是与倾斜平面波的干涉图。

Fig.15 Experimental output results of the transition from linear Tamm-like to linear Shockley-like and to nonlinear Tamm-like surface states. The probe beam enters the first waveguide shown with arrow of the superlattice. a) Linear Tamm-like state due to a negative surface defect. b) Linear Shockley-like state at the surface without any perturbation. c) Nonlinear Tamm-like state due to a self-induced positive surface defect. Top two rows: transverse intensity patterns of superlattice and output probe beams. Bottom row: phase measurement by interference between the output probe beam and a tilted plane wave.

通过FDTD模拟我们发现当光通过长度为微米量级的电介质纳米波导阵列的时候会发生会聚现象。结果显示焦距依赖于波导阵列的长度和总宽度并且在几十微米到波长量级可调。TM波和TE波入射都能被波导阵列聚焦。通过改变介电纳米波导阵列中波导的间隔，我们能够获得波长量级的焦距。这种独特的聚焦行为我们归结于纳米波导阵列中存在的长衰减距离的辐射模和大的疏逝场。我们相信，这个理论模拟结果对实验会有很大的指导意义。

The light focusing by using dielectric nano-waveguides array with its length in micron is investigated *via* the finite-difference time domain (FDTD) method. Simulated results show that the focal length depends on the length and the total width of the arrays and can be altered from tens of micron to wavelength order. Both TM and TE mode incident light can be focused by the array. The wavelength-order focal length is achieved by employing the dielectric nano-waveguide array with variant separations. The unique focusing behavior is contributed to the radiation mode with longer decay length and the large evanescent field which appears in the nano-waveguide array. We believe this simulation results can be a promising guidance for the experiments.
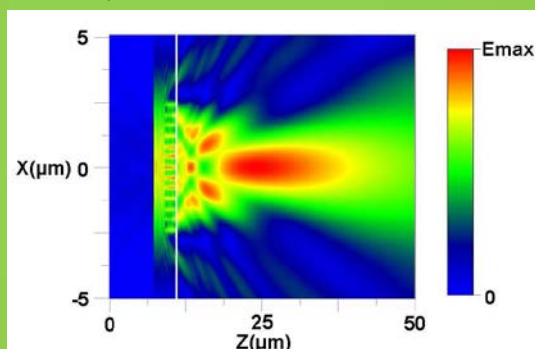
图16 纳米波导阵列电场强度分布图。其中$N = 13$, $W = D$ =300nm, $L = 2.0\mu m$。入射光的半高宽为7.5微米。白线代表阵列的末端。

Fig.16 The electric field distribution of the nano-waveguide array with $N = 13$, $W = D$ =300nm, $L = 2.0\mu m$. The *FWHM* of the incident light is 7.5μm. The white vertical line presents the end of the array.

我们实现了用多束飞秒激光在硅玻璃中并行写入信息的方法。共线但波前曲率半径不同的飞秒激光光束入射到同一个物镜上并聚焦在硅玻璃的不同深度处。这样在硅玻璃中形成了多个焦点，从而实现了多层并行写入。通过调节光束波前的曲率半径可以改变层距和层的队列。我们的并行写入方法有利于缩短飞秒激光直写的写入时间。

We present a parallel writing method in silica glass by multiple femtosecond laser beams. Collinear femtosecond laser beams with different wavefront curvature were incident on an objective lens and focused at different depths below the surface of silica glass. Hence multiple focal points exist in the glass simultaneously and parallel writing on multiple layers is realized. By adjusting the beam wavefront, the layer distance and the layer alignment can be changed. Our parallel

writing method is useful to shorten the fabrication time of femtosecond laser direct writing.
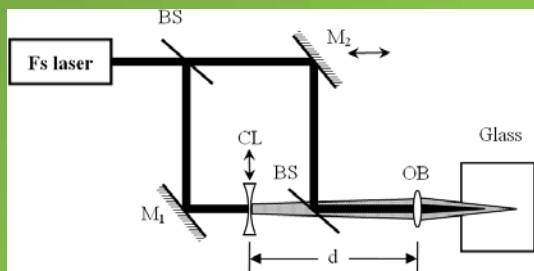
图17 并行直写配置草图。

Fig.17 Sketch of the parallel writing setup.

为了研究吸收双层球形微粒的横向光俘获,基于几何光学模型提出了双层带吸收球形微粒的光俘获模型,对TEM00模式高斯光束照射下外层有光吸收的双层电介质球形微粒受到的横向光俘获力进行了数值模拟,取得了光俘获力特性的一系列结果. 结果显示,双层球形微粒的外层吸收系数对包括稳态俘获位置,峰值强度,稳态俘获的刚度等光俘获特性有很大影响. 此外,内外径的比率对吸收双层球形微粒的光俘获特性也有调制性的影响。在一定条件下,带吸收的双层球形微粒可以被俘获在光轴上,也可能被俘获在中心在光轴上的圆环上.

The transverse optical trapping of absorbing double2layer spherical particle is studied based on geometrical optics model . A model for double2layer spherical particle with optical absorption is presented. The transverse optical trapping force of a double2layer dielectric spherical particle with linear absorption in the outer layer illuminated by a focused Gaussian beam of TEM00 mode is simulated numerically. Our results show that the characteristics of optical trapping , including the stable trapped positions , the peak intensity and the stiffness of stable trapping , greatly depend on by the absorption coefficient of the double2layer spherical particle. Besides , the ratio of the inner radius to the outer radius of the particle also has modulating influence on the properties of transverse trapping. It is possible to trap transversely the double2layer spherical particle with absorption on the axis of the incident Gaussian beam and on a circle centered at the optical axis for different axial offsets of sphere center from the beam waist as well .

光谱表征及传感技术/Spectral Charaterization and Sensing Techniques

负责人：臧维平

　　本方向涉及激光器，上转换发光材料，光纤器件，稀土掺杂发光材料，应用光谱学和光谱仪器等方面。取得的代表性成果如下：

　　In this field, we mainly focused on the laser, up conversion luminescent material, fiber optic, rare earth dope glass, applied spectroscopy and spectral instrument. This year, we obtained some important results, they are mainly shown as following:

玻璃陶瓷的研究
Research on glass ceramics

　　Er^{3+}/b^{3+}共掺磷酸盐玻璃具有储能大、能量传递效率高等优点，这对上转换和下转换发光都有很大的益处。但磷酸盐玻璃自身又具有一些缺点，比如机械强度较差、易潮解和发光效率底等，这使得在应用上受到了很大限制。但玻璃陶瓷能结合玻璃和晶体的优点，从而弥补玻璃材料的不足。目前对于掺铒的氟氧化物玻璃陶瓷的研究较多，但是对掺铒磷酸盐玻璃陶瓷的报道很少。尤其热处理温度和时间对析出的纳米晶类型的影响研究还很不深入。为此，我们制备了多种配比的玻璃样品，并最终通过热处理得到玻璃陶瓷，取得的具体成果有：

表1 不同Li浓度的磷酸盐玻璃陶瓷
Table1 Phosphate glass ceramics with different Li-doped concentration

玻璃组分	P_2O_5	Li_2O	Er_2O_3	Yb_2O_3
摩尔比（mol％）	80	20	0.05	0.25
摩尔比（mol％）	75	25	0.05	0.25
摩尔比（mol％）	70	30	0.05	0.25
摩尔比（mol％）	65	35	0.05	0.25
原料	$NH_4H_2PO_4$	Li_2CO_3	Er_2O_3	Yb_2O_3

　　Er^{3+}/Yb^{3+} phosphate glass has advantages of large energy storage and high energy transfer efficiency, which has important applications in the upconversion. However, the glass itself has some weaknesses, such as the weak mechanical strength, easy to deliquescence and lower luminous efficiency, which make the applications of the materials limited. But glass ceramic combines the advantages of glass and ceramic. Now Er^{3+}-doped fluoride glass-ceramic have widely been studied. But the research on the phosphate glass ceramics (especially, the impacts of the annealing temperature, time on the type of nanocrystal) is less. Therefore, we prepared the Er^{3+}/Yb^{3+} phosphate glasses. And by annealing, the phosphate glass ceramics were obtained.

(1) 通过热处理前驱玻璃，我们成功得到了掺铒磷酸盐玻璃陶瓷．下图为配比$(80P_2O_5\text{-}20Li_2O)\text{-}0.05$ $Er_2O_3\text{-}0.25Yb_2O_3$ (mol%)在不同热处理温度的 XRD 图．图中明显显示随热处理时间的增长，衍射峰的数目和纳米晶的种类也随着增加。
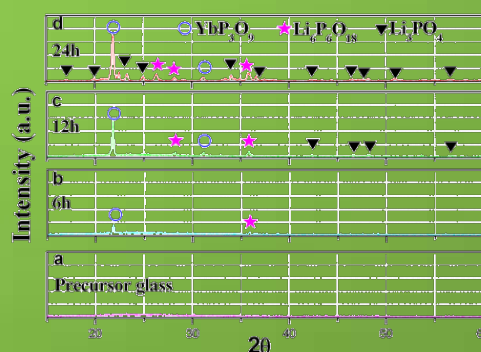
图 1 前驱玻璃和玻璃陶瓷（在 790K 热处理不同时间）的 XRD 谱
Fig.1 XRD patterns of the precursor glass and glass ceramics that were annealed at 790K for different heat treatment times

　　By annealing the precursor glasses, the phosphate glass ceramics were prepared. The next picture shows the XRD diagrams of the samples with the ratio of $(80P_2O_5\text{-}20Li_2O)\text{-}0.05$ $Er_2O_3\text{-}0.25Yb_2O_3$ (mol%), which were heated at 790K for different times. From the figure, it is obvious that the numbers and kinds of diffraction peaks increase with the increasing of annealing time.

(2) 为了进一步证实 XRD 的结果，我们对玻璃陶瓷样品做了透射电镜（TEM）测试。 测试结果和通过 XRD 得到的结论很好吻合，见图 2。
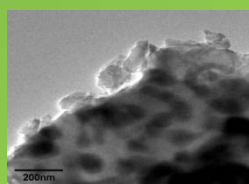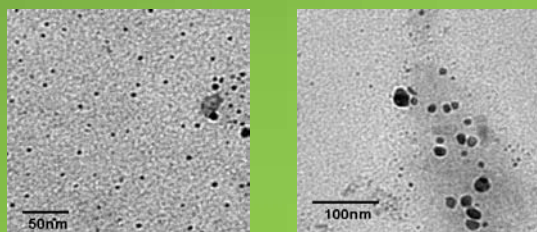
图 2 玻璃陶瓷 [790K 热处理 6h(a)、 12h(b) 和 24h(c)] 的 TEM 图像

Fig.2 TEM image of glass ceramics annealed at 790K for 6h(a)、12h(b) and 24h(c)

For proving the results of XRD, the TEM diagrams of the glass ceramics were measured. And the results were in good agreement with the XRD measurements and calculations.

(3) 图 3 是前驱玻璃和玻璃陶瓷在 975nm 激光二极管泵浦下的发光光谱。 如图可见，玻璃陶瓷样品的发光要明显强于玻璃的，而且谱线也出现了明显的劈裂，证明了 Er^{3+} 周围的晶体场明显增强。

Fig.3 shows the luminescence spectra of the glass and glass ceramics at 975 nm laser diode pump. From Fig.3, the emission intensity of the glass ceramics are stronger compared to that of the glass. And the Stark split is very obvious, which shows that the crystal field intensity around Er^{3+} has increased.
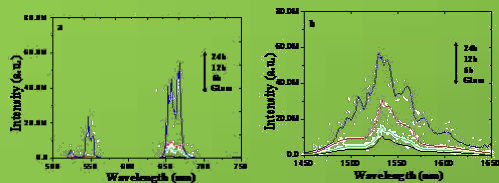
图 3 在 975nm 激光二极管泵浦下，前驱玻璃和玻璃陶瓷的上转换和红外光谱

Fig.3 UC emission and infrared luminescence spectra of the glass and glass ceramics at 975nm LD pump

(4) 图 4 是上转换发光强度与泵浦功率的关系图。如图可知玻璃和玻璃陶瓷的上转换红光和绿光的布居进程基本一样，都是两光子进程。
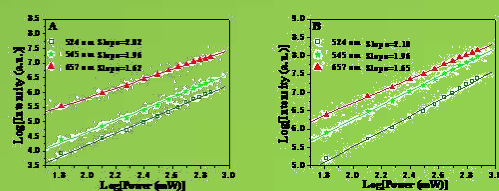
图 4 上转换红光和绿光的发光强度与泵浦功率的关系

Fig.4 log-log plots for the dependence of the green emissions and the red emission intensities of on pump power

Fig.4 is the log-log plots for the dependence of the green emissions and the red emission intensities on pump power. The population processes of both the red emission and the green emissions are two-photon processes.

(5) 1.54um 荧光的增强

(5) Increasing of 1.54um luminescence

表 2 是样品中掺入了 Ce,Yb,Er 的比例，通过 Ce 的掺入，我们发现 $^4I_{11/2}$ 能级寿命明显降低，$^4I_{13/2}$ 能级寿命变化不大，1.54um 荧光强度有所增强，见图 5。

表 2 不同掺 Ce 浓度的磷酸盐玻璃陶瓷

Table 2 Phosphate glass ceramics with different Ce-doped concentration

Samples	CeO₂(mol%)	Er₂O₃(mol%)	Yb₂O₃(mol%)
CYE0	0	0.2	7.0
CYE1	0.2	0.2	7.0
CYE2	0.4	0.2	7.0
CYE3	0.8	0.2	7.0
CYE4	1.2	0.2	7.0
CYE5	1.6	0.2	7.0
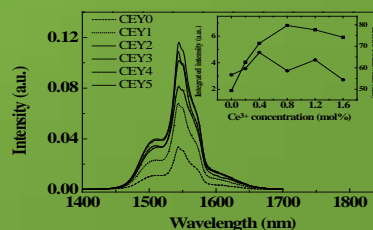
图 5 Ce^{3+} 的敏化对于 1.54um 荧光的影响

Fig.5 Impact 1.54um luminescence on the sensitizing of Ce^{3+}

Table 2 is the rate of Ce,Yb,Er in the glass ceramics. Through doping Ce, we observed that

the lifetime of $^4I_{11/2}$ energy level obviously decreased, but the lifetime of $^4I_{13/2}$ energy level changed less. And the 1.54um luminescence intensity increased, seen in Fig.5.

结论：通过在 790K 热处理前驱玻璃我们得到了磷酸盐玻璃陶瓷，并且发现随热处理时间的增长，纳米晶的尺寸和类型都发生转变。在光谱的测试中发现，玻璃陶瓷样品的发光要明显强于玻璃的。

Results: By annealing the precursor glasses at 790K, we obtained the phosphate glass ceramics. And we observed that the type and size had changed with the increasing of annealing time. By measuring the luminescence spectra, we also found that the emission intensity of the glass ceramics are stronger than that of glass.

氟氧化物玻璃陶瓷的相关研究

对于热诱导-腐蚀法制备的纳米发光颗粒进行了深入的研究，主要集中在以下方面：对于纳米发光颗粒的结构进行研究，结果发现在热诱导过程中纳米发光颗粒的结构会随着热诱导温度的升高而发生改变，已经通过结构模型对这一问题进行了模拟，正在撰写论文。对于纳米发光颗粒的激发态电子的瞬态行为进行了研究，发现其红色和绿色激发态能级寿命存在数量级的差别，从而导致发光过程存在不同的能量传输过程。尝试使用水相纳米发光颗粒搭建液体激光器系统。
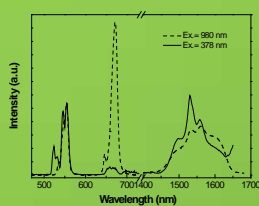
图 1 Er^{3+}/Yb^{3+}共掺碲酸盐玻璃陶瓷中上转换和下转换光谱。

Fig.1 Up-conversion and down-conversion fluorescence spectra of Er^{3+}/Yb^{3+}-codoped tellurite oxyfluoride glass ceramics.

The properties of luminescent nanoparticles prepared by the thermal induction and corrosion treatment were researched as following. Structure of luminescent nanoparticles. With the increasing of thermal temperature, the structure of luminescent nanoparticles was changed. The model was build to simulate the structure variety. Transient state process of metastable energy level. The life time of

red and green excited state have a rather large difference, which indicates that different energy transfer processes exist in the transition of red and green excited state to ground state. Try to build fluid state laser system by nanoparticles in aqueous solution.
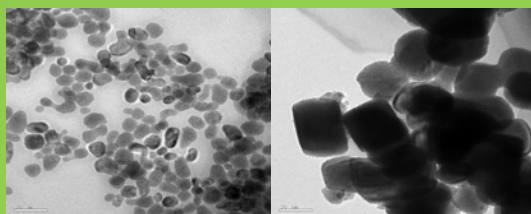
图 2 不同热处理条件下玻璃陶瓷中微晶的 TEM 图片
Fig.2 TEM micrographs of nano-particles under different thermal treatment

3.光谱表征领域和仪器领域

主要开展如下几个方面工作：

（1）金属纳米微结构的制备工作和拉曼表面增强光谱研究。利用氧化铝纳米结构模板，制备了具有 60－200nm 特征尺寸的微结构金属薄膜（图 1，图 2），并应用于表面增强拉曼光谱检测中，稳定的获得了 10^5 的增强因子。

（2）拉曼光谱仪器研究。开发了小型化激光拉曼光谱仪（图 3），具有如下技术重点：光栅尺反馈精密定位机构光栅转台；研究级别显微镜探头；大尺寸三维光纤扫描探头装置；光纤共焦扫描采谱；像散纠正成像光谱仪等。

（3）光谱检测应用研究。继续开展 OLED 发光器件的光谱表征研究，以及紫外敏化镀膜技术（图 4）应用研究。

3. Spectral characterization and spectral instrument

Mainly carrying out the following aspects of work:

(1) The preparation and surface-enhanced Raman spectroscopy of the metal nano-micro structure. Useing alumina oxidized AO nano-structured template, we prepared micro-structure of metal film with 60-200nm feature size (Fig1 Fig2), and applied to surface-enhanced Raman spectroscopy detection the silver film has uniform Raman enhancement factor about 10^5.
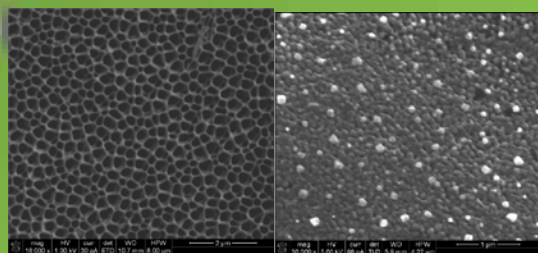
图 1 银薄膜网状微结构 SEM 照片
Fig1 The SEM image of mesh structure on silver film

图 2 银薄膜点状微结构 SEM 照片
Fig2 The SEM image of dot structure on silver film

图 3 显微拉曼光谱仪样机
Fig3 The prototype of micro-RAMAN spectrometer

(2) Raman spectrometer (Fig3). We has developed a small laser Raman spectrometer, with the following technical features: precision positioning mechanism grating turntable with optical grating feedback; research-level microscope probe; large-size three-dimensional optical fiber scanning probe device; optical fiber confocal scanning spectrum; astigmatism corrected imaging spectrometer.

(3) Applied research of spectrum detection. Continue to carry out the research of spectral characterization OLED devices, as well as applied research of UV sensitized film using CCD (Fig4).
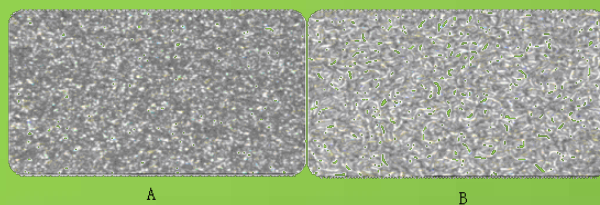
图 4 Lumogen 紫外敏化材料晶体薄膜（A）显微照片与再晶化处理后薄膜（B）显微照片对比

Fig4 The morphology image of LUMOGEN pigment material for CCD UV sensitized film（A：crystallized Lumogen pigment material，B：re-crystallized Lumogen pigment mateial）

半导体生长技术和半导体器件/ Semiconductor Growth and Devices

负责人：舒永春

2009 年度本方向主要在以下方面取得了进展：

This year, we obtained some important results, they are mainly shown as following:

硅基发光器件的研究进展

（1）搭建了光致发光和电致发光测量系统利用 Laview 程序将锁相放大器、高压源表、光谱仪和数据采集系统结合起来，实现了光致发光光谱、激发光谱、电致发光光谱、光强－电流－电压特性、电致发光老化的自动化测量，如图 1 所示。程序方框图如图 2。系统可以测量红外－紫外波段的光谱，电流范围 10pA－1A， 电压 0-1100V，最低探测光强极限小于 1 纳瓦。

图 1.电致发光、光致发光、I-V，L－I－V 综合自动测量系统

Fig.1 the automatic EL and PL measurement system and the programs
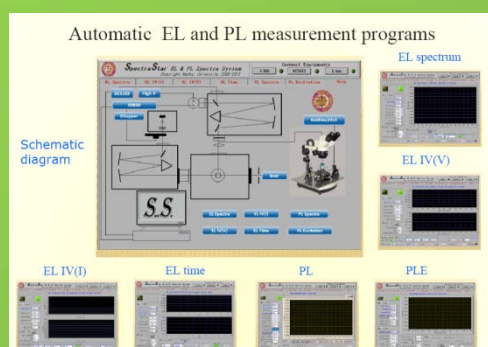
图 2.程序方框图

Fig.2 the automatic EL and PL measurement programs

PL, EL and optoelectrical system has been set up.We have set up a photoluminescence and electroluminescence study system with Labview program. Fig.1 and Fig.2 show the automatic EL and PL measurement system and the programs. With this system we can measure photoluminescence spectra from ultraviolet to near infrared (200-1700nm). Electroluminescence from silicon pn diodes and MOS light emitting devices at constant current from 10pA to 1A or constant voltage from 0-1100V. I-V-L characteristics in a current controlled or voltage controlled mode. The sensitivity of the system are very high, the lowest detectable light intensity <1nW.

建立起了一套硅基电致发光器件工艺线。包含硅片标准清洗柜原子层沉积系统，用来制备高质量稀土掺杂的 SiO_2 发光薄膜，HfO_2 high-K 薄膜等，超声波雾化热分解透明 ITO 薄膜沉积系统，真空热蒸发技术金属薄膜沉积系统，光刻系统和旋转涂敷系统。

A processing line for silicon based MOS light emitting devices has been installed including Silicon wafer cleaning. An atomic layer deposition system for deposition of rare-earth oxide, HfO_2 high-K dielectric layers, and SiO_2 layer doped with rare earths. Ultrasonic Spray Pyrolysis Method for deposition of transparent ITO electrode. Vacuum thermal evaporation system for Al Au and Ag metallic films. Photolithography system and spin coating system.

（2）确定了电致发光器件的标准 MOS 工艺流程，最终制备的硅基 MOS 电致发光器件 ITO/SiON/Si-richSiOB$_{2B}$ /Si   MOS 电致发光器件。

Er-doped silicon nanocluster based MOS light emitting devices have been processed with a structure of ITO/SiON/Si-richSiOB$_{2B}$ /Si.

纳米硅的强烈敏化作用使 Er 离子的红外发光增强了 2 个数量级。在功率 20 mW、波长 405 nm 的 GaN 激光器激发下，可以观测到来自纳米硅和 Er 离子的强烈光致发光。图 3 为具有不同过量纳米硅浓度的富硅 TSiOB$_{2B}$ 薄膜的光致发光光谱。当纳米硅浓度大于 5% 时，来自纳米硅微晶法人发光峰随着纳米硅浓度的增大显著增强，随着富硅含量的增加，纳米硅的直径增大，相应的发光

峰发生红移，符合低维半导体的量子尺寸效应。
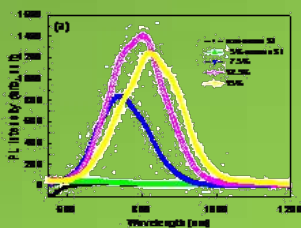
图 3. 具有不同过量纳米硅浓度的富硅 SiO₂ 薄膜的光致发光光谱。
Fig.3 PL spectra from the Si-rich SiO2 films containing different excess Si concentrations of 0,5,7.5,12.5 and 15%.

图 4 为 1.5% Er 掺杂的分别具有 0、5、7.5、12.5 过量纳米硅浓度的 Si-rich SiO₂：Er 薄膜的光致发光光谱，可以看出，当纳米硅浓度大于 5% 时，来自 Er 的红外发光峰值随着纳米硅浓度的增大显著增强，比不含纳米硅的样品增强两个数量级，这表明，在 Er 掺杂的富硅 SiO₂ 薄膜中，来自纳米硅的能量转移对于 Er 离子的光致发光具有很大的增强作用。

Efficient photoluminescence from the silicon nanoclusters in Si-rich SiO₂ has beeen observed, and strong energy transfer from silicon cluster to Er luminescent centers causes a strong increased of the luminescence efficiency of the infrared emission. Fig.3 shows the PL spectra from the Si-rich SiO₂
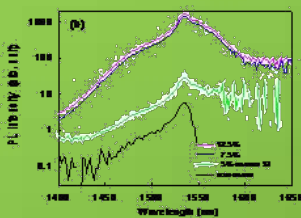
图 4. 1.5%Er 掺杂的分别具有不同过量纳米硅浓度的 Si-richSiO₂：Er 薄膜的光致发光光谱
Fig.4 PL spectra from the 1.5% Er doped Si-rich SiO2:Er films containing different excess Si concentrations of 0,5,7.5,12.5 and 15%.

films containing different excess Si concentrations of 0, 5 ,7.5, 12.5 and 15%. Fig.4 shows the PL spectra from the 1.5% Er doped Si-rich SiO₂:Er films containing different excess Si concentrations of 0,5,7.5,12.5 and 15%.

（3）利用 SiON 缓冲层结构提高了电致发光器件的稳定性。通过采用 SiON 缓冲层符合薄膜结构，制备出 ITO/SiON/Si-rich SiO₂:Er/Si MOS 结构电致发光器件，图 5 是器件结构示意图。为了增加光耦合输出效率，表面电极采用 100 nm 的透明 ITO 导电层。图 6 为固定 SiO₂：Er 发光层厚度，MOS 结构的 I-V 特性随 SiON 缓冲层厚度的变化曲线。其中 SiON 缓冲层显著提高了电致发光器件的工作电压和电流范围， 提高了电致发光器件的稳定性和可靠性，器件的平均寿命提高了四个量级。
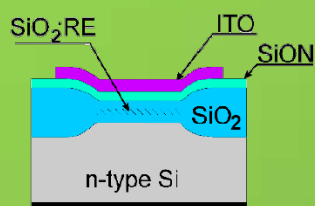
图 5. 复合栅层 MOS 结构电致发光结构简图。结构中 SiON 作为器件的防击穿缓冲层。
Fig.5 Scheme of the Double-gate layer MOS EL structure.
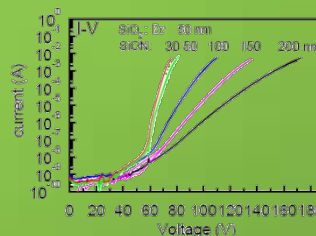
图 6 固定 SiO₂：Er 发光层厚度，MOS 结构的 I-V 特性随 SiON 缓冲层厚度的变化。
Fig.6 I-V characteristics of the MOS structure with different thickness of SiON buffer layer and fixed thickness of SiO2:Er light-emitting layer

The stability of the MOS light emitting devices was strongly improved with SiON buffer layers in the MOS devices.Fig.5 shows the scheme of the Double-gate layer MOS EL structure. Fig.6 is the I-V characteristics of the MOS structure with different thickness of SiON buffer layer and fixed thickness of SiO₂:Er light-emitting layer.

（4）获得了较强的红外电致发光。系统研究了硅微晶密度的变化对于 MOS 结构的电致发光影响。主要结果如图 7、图 8 所示：与光致发光相反，随着纳米硅微晶的增多，

电致发光效率有所降低。其原因为增加纳米硅微晶数量的同时也增加了 SiO₂ 薄膜中的电子俘获陷阱，在电场作用下，纳米硅中的激子在空间上分离为电子和空穴，电子和空
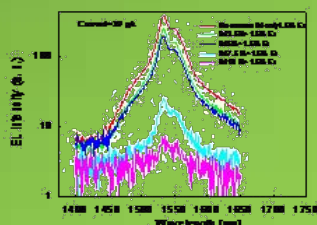
图 7. 1.5%Er 掺杂的分别具有不同过量纳米硅浓度的 Si-richSiO₂：Er 薄膜的电致发光光谱， 器件直径 0.5 mm， 电流为 100 微安。
Fig.7 EL spectra from the 1.5% Er doped Si-rich SiO2:Er films containing different excess Si concentrations of 0,2.5, 5,7.5 and 10%

穴在纳米硅微晶之间的隧穿降低了过热电子的数量和平均能量，因而降低了碰撞激发 Er 离子产生的电致发光效率。
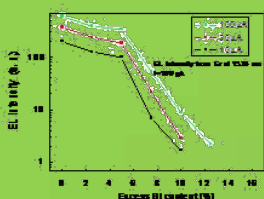
图 8. 1.5%Er掺杂的分别具有不同过量纳米硅浓度的Si-rich SiO₂：Er薄膜的电致发光强度随纳米硅含量的关系。
Fig.8 The relationship of EL intensity from the 1.5% Er doped Si-rich SiO2:Er films with the excess Si content.

Strong infrared electroluminescence from Er doped silicon rich SiO₂ MOS devices has been observed. Fig.7 EL spectra from the 1.5% Er doped Si-rich SiO₂:Er films containing different excess Si concentrations of 0,2.5, 5,7.5 and 10%.Fig.8 shows the relationship of EL intensity from the 1.5% Er doped Si-rich SiO₂:Er films with the different content of excess Si.

MBE 工作汇报
The MBE working report
1. VECSEL 研究进展
（1）材料生长达到的角度：VCESEL 全结构材料生长精度均在 1%以内 ，除 AlGaAs 层外，生长厚度误差均在 1nm 以内

The research progress of VESCEL

The scale precision of material growth: The forms show that the scale precision of the VESCEL whole structure material growth was below 1%, the deviation of thickness growth was below 1 nm except the layer of AlGaAs.

Structure		Measurement values	Design values	Error ratio	
		unit：nm			%
DBR	AlAs	91.50	91.4	0.10	0.11%
	GaAs	77.17	76.6	0.57	0.74%
	Total:	168.90	168	0.90	0.54%
WeLL	InGaAs	153.12	153.1	0.02	0.01%
	AlGaAs	445.7	441.5	4.2	0.95%

（2）980nm、1064nm VECSEL 芯片材料：所得到的 VECSEL 芯片材料荧光光谱的波长误差在 5nm 以内；半高宽在 15nm 以内。

The photoluminescence spectrum of 1064nm whole structure material of VESCEL chip were shown in fig 2
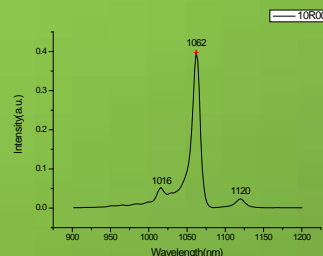
图 2 VECSEL 芯片材料全结构荧光光谱
Fig.2 The photoluminescence spectrum of 1064nm whole structure material of VESCEL chip

（3）下一步工作：AR coating 、散热和泵浦实验研究、光路平台搭建。

Next steps: AR coating, heat sinking and optical pumping experiment, setting up the optical platform

2. DWELL (dots-in-a-well)结构材料研究
The research of DWELL (dots-in-a-well) structure material
目的：开发远红外探测新型结构材料。
1、理论分析与计算工作：以材料为垒层 GaAs，量子阱 In0.15Ga0.85As，量子点 InAs,建立三维计算模型；考虑周期性分布的量子点间的横

向相互作用，分量子点现状分别为金字塔形和圆柱形两种方式进行分析，结果如下：

Object: exploit the novel material of infrared detecting device.

The theoretical analysis and numerical simulation: The material including barrier-layer: GaAs, well-layer: $In_{0.15}Ga_{0.85}As$, dots-layer: InAs, forming the 3D model, included the effect of the periodic arrangement of quantum dots, the pyramid and cylinder type quantum dots were both computed.

A、金字塔型量子点：No.1 和 No.2 中基态和第一激发态之间的能级差分别为 64.2meV，46.3meV；No.2 的基态能和激发态能均低于No.1，可见量子点间的横向作用可以降低能级同时减小能级差。

No.1 dirichlet boundary condition
z=20nm, x=1~20, y=1~20
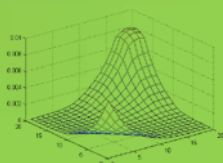
ground state energy= 0.2889meV
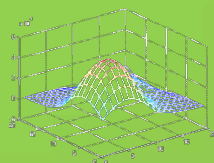
first excited state energy= 0.3531meV

No.2 periodical boundary condition
z=20nm, x=1~20, y=1~20
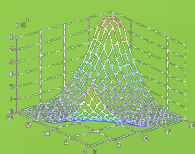
ground state energy = 0.2794meV
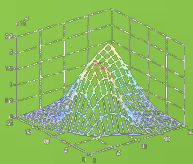
first excited state energy = 0.3257meV

Pyramid QD: The results show that No.1 and No.2 energy-level difference between the ground state energy and first excited state energy were 64.2meV and 46.3meV respectively, both states energy and energy-level difference in No.2 were smaller than those in No.1, it could be explained by the transverse effect between QDs.

B、圆柱型量子点：No.3 和 No.4 中基态和第一激发态之间的能级差分别为 51.6meV，48.4meV，No.4 的基态能和激发态能均低于No.3；同样再次说明了量子点间的横向作用。

Cylinder QD: The results show that No.3 and No.4 energy-level difference between the ground state energy and first excited state energy were 51.6meV and 48.4meV respectively, the energy Comparison results demonstrate the the transverse effect between QDs.

No.3 dirichlet boundary condition
z=20nm, x=1~20, y=1~20
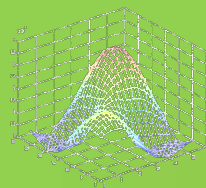
ground state energy= 0.1297meV
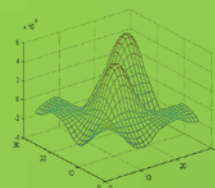
first excited state energy = 0.1813meV

No.4 periodical boundary condition
z=20nm, x=1~20, y=1~20
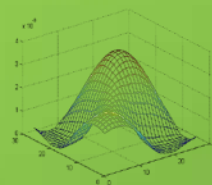
ground state energy= 0.1285meV
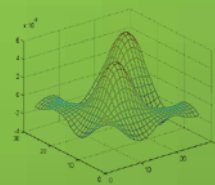
first excited state energy = 0.1769meV

理论分析结果：量子点间的横向相互作用可降低能级，有助于在远红外波段的应用；同样，我们结合泊松方程计算掺杂效应，也能观察到类似效应，通过改变和调节量子阱的宽度则能进一步调整相应波段，对于我们制备远红外探测器提供了理论依据和指导。

The interaction effect between QDs can lower the energy level and energy difference, it contributes to the DWELL application in infrared wave band; if included the doping effect by the combination with the Poisson function, the similar results were obtained. By means of adjusting the quantum well width, the response wave band could be further improved. Those effects show the

theoretical basis and guidance of the preparation of infrared detecting device materials.

2、下一步工作：2010 年开展该材料的生长

与性能研究。

Next steps: starting the research of the DWELL material growth and performance in 2010.

发表论文∕Publications in Journal

1. Wending Zhang, Feng Gao, Guoquan Zhang, Wei Li, Xinzheng Zhang, and Jingjun Xu, "Experimental observation of subluminal and superluminal light propagation in R 6G -doped PMMA ", Appl. Phys. Lett. 95, 171106 (2009).*

2. Zhibo Liu, Yan Wang, Xiaoliang Zhang, Yanfei Xu, Yongsheng Chen, Jianguo Tian, "Nonlinear optical properties of graphene oxide in nanosecond and picosecond regimes", Appl. Phys. Lett. 94: 021902(2009).*

3. Shao Weiwei, Li Lin, Liu Weiwu, Zhang Tianhao, Ma Huihui, Xu, Jingjun, Tian Jianguo, "Tunable long-range surface plasmon polaritons taking advantage of nonlinear surface waves", Appl. Phys. Lett.95: 211105(2009).

4. Yanfei Xu, Zhibo Liu, Xiaoliang Zhang, Yan Wang, Jianguo Tian, Yi Huang, Yanfeng Ma, Xiaoyan Zhang, Yongsheng Chen, "A Graphene Hybrid Material Covalently Functionalized with Porphyrin: Synthesis and Optical Limiting Property", Adv Mater. 21(12): 1275(2009).*

5. Wei Cai, Rebecca Sainidou, Jingjun Xu, A. Polman, and F. J. G. de Abajo, "Efficient generation of propagating plasmons by electron beams", Nano Lett. 29(3), 1176-1181 (2009).*

6. Xinyuan Qi, Ivan L. Garanovich, Zhiyong Xu, Andrey A. Sukhorukov, Wieslaw Krolikowski, Arnan Mitchell, Guoquan Zhang, Dragomir N. Neshev, and Yuri S. Kivshar, "Observation of nonlinear surface waves in modulated waveguide arrays", Opt. Lett. 34, 2751 (2009).*

7. H.Yi, C. Lou, P. Zhang, S. Liu, F. Xiao, J. Zhao, J. Xu and Z. Chen, "Orientation-dependent excitations of lattice soliton trains with hybrid nonlinearity", Optics Letters 34, 1114 (2009). **Also selected for the May 2009 issue of Virtual Journal of Ultrafast Science.***

8. Yong-Fa Kong, Fu-Cai Liu, Tian Tian, Shi-Guo Liu, Shao-Lin Chen, Romano Rupp and Jing-Jun Xu, "Fast responsive nonvolatile holographic storage in $LiNbO_3$ triply doped with Zr, Fe, and Mn", *Opt. Lett.* 34(24), 3896-3898 (2009).*

9. Kang HZ, Zhang TH, Wang BH, Lou CB, Zhu BG, Ma HH, Liu SM, Tian JG, Xu JJ, "(2+1)D surface solitons in virtue of the cooperation of nonlocal and local nonlinearities", Opt. Lett. 34(21), 3298-3300 (2009).*

10. N. Malkova, I. Hromada, X. Wang, G. Bryant, and Z. Chen, "Observation of optical Shockley-like surface states in photonic superlattices", Optics Letters 34, 1633 (2009).

11. H. Yi, C. Lou, P. Zhang, J. Xu, J. Yang and Z. Chen, "Saddle solitons: a balance between bi-diffraction and hybrid nonlinearity", Optics Letters 34, 3259 (2009).

12. I. Hromada, N. Malkova, X. Wang, G. Bryant, and Z. Chen, "Optical Shockley-like surface states in photonic superlattices", Opt. & Photonics News 20, 23 ("Optics in 2009").

13. Yanfei Tu, Guoquan Zhang, Zhaohui Zhai, and Jingjun Xu, "Angular multiplexing storage of light pulses and addressable optical buffer memory in Pr3+:Y2SiO5 based on electromagnetically induced transparency", Phys. Rev. A 80, 033816 (2009).*

14. Lei Xu, Guoquan Zhang, Ningning Xu, Fang Bo, Feng Gao, Wande Fan, Jingjun Xu, Kar Pong LOR, and Kin Seng Chiang, "Active chromatic control on the group velocity of light at arbitrary wavelength in BCB polymer", Opt. Express 17, 18292-18303 (2009).

15. Xinyuan Qi, Guoquan Zhang, Ningning Xu, Yiling Qi, Bin Han, Yulan Fu, Changsha Duan, and Jingjun Xu, "Linear and nonlinear discrete light propagation in weakly modulated large-area two-dimensional

---

* 选录论文∕Selected papers

photonic lattice slab in LiNbO3:Fe crystal", Opt. Express 17, 23078-23084 (2009).

16. Xinzheng Zhang, Junqiao Wang, Baiquan Tang, Xinhui Tan, Romano A. Rupp, Leiting Pan, Yongfa Kong, Qian Sun, and Jingjun Xu, "Optical trapping and manipulation of metallic micro/nanoparticles via photorefractive crystals", Opt. Exp. 17(12), 9981-9988 (2009).*

17. Jian-Xing Li, Wei-Ping Zang,Ya-Dong Li, Jianguo Tian, "Acceleration of electrons by a tightly focused intense laser beam", Opt. Express 17: 11850-11859 (2009).

18. Jianxing Li, Weiping Zang, Jianguo Tian, "Simulation of Gaussian laser beams and electron dynamics by Weniger transformation method", Opt. Express 2009, 17: 4959-4969.

19. Xiao-Liang Zhang, Xin Zhao, Zhi-Bo Liu, Yong-Sheng Liu, Yong-Sheng Chen, Jian-Guo Tian "Enhanced nonlinear optical properties of graphene-oligothiophene hybrid material", Opt. Exp. 2009 17(26): 23959.

20. Xiao-Qing Yan, Zhi-Bo Liu, Xiao-Liang Zhang, Wen-Yuan Zhou, Jian-Guo Tian, "Polarization dependence of Z-scan measurement: theory and experiment," Opt. Exp. 2009, 17(8): 6397-6406.

21. Lihua Zhao, Yudong Li, Jiwei Qi, Jingjun Xu, and Qian Sun "Light focusing by the unique dielectric nanowaveguide array", Opt. Exp. 17, 17136-17143 (2009).

22. Qiang Wu, Christopher A. Werley, Kung-Hsuan Lin, August Dorn, Moungi G. Bawendi, and Keith A. Nelson, "Quantitative phase contrastimaging of THz electric fields in a dielectric waveguide", Opt. Exp. 17(11), 9219-9225 (2009).

23. P. Zhang, R. Egger, and Z. Chen, "Optical induction of three-dimensional photonic lattices and enhancement of discrete diffraction", Optics Express, 17, 13151 (2009).

24. X. Wang and Z. Chen, "Beam control and multi-color routing with spatial photonic defect modes", Optics Express, 17, 16927 (2009).

25. W. Wang, V. Roppo, K. Kalinowski, Y. Kong, D. N. Neshev, C. Cojocaru, J. Trull, R. Vilaseca, K. Staliunas, W. Krolikowski, S. M. Saltiel and Yu. Kivshar, "Third-harmonic generation via broadband cascading in disordered quadratic nonlinear media", Opt. Express 17(22), 20117-20123 (2009).

26. Martin Kuttge, Wei Cai, F. Javier Garcia de Abajo and A. Polman, "Dispersion of metal-insulator-metal plasmon polaritions probed by cathodoluminescence imaging spectroscopy", Phys. Rev. B, 80, 033409 (2009).

27. P. Zhang, C. Lou, S. Liu, F. Xiao, J. Zhao, J. Xu and Z. Chen, "Hybrid nonlinearity supported by nonconventionally biased photorefractive crystal", Applied Phys B 95, 559 (2009).

28. Uygun V. Valiev, Sharof A. Rakhimov, Nafisa I. Juraeva, Romano A. Rupp, Lijuan Zhao, Zhenhua Wang, ZhaoYang Zhai, John B. Gruber, and Gary W. Burdick, "Optical and magnetooptical properties of Ho3+:YGG", Phys. Status Solidi B 247(1), 163–169 (2009).

29. J. M. Sun, M. Helm1, W. Skorupa, B. Schmidt, and A. Mücklich, "Light emissionfrom ion-implanted silicon", Phys. Status Solidi C 6, No. 3, 716-720 (2009).

30. Zhang TH, Zhang LZ, Yu XY, He R, Hu ZJ, Xu JJ, "The Coupling Between Forward Propagating Wave and Backward Propagating Wave for Photorefractive Surface Waves", IEEE Journal of Quantum Electronics 45,1-2,132-137(2009).

31. Leiting Pan, Xinzheng Zhang, Kun Song, Baiquan Tang, Wei Cai, Xian Wu, Romano A. Rupp, and Jingjun Xu, "Real-time imaging of autofluorescence NAD(P)H in single human neutrophils", Appl. Opt. 48(6), 1042-1046(2009).

32. Yiling Qi, Anas F. Jarjour, Xu Wang, Robert A. Taylor, and Guoquan Zhang, "Design of leaky modes of two-dimensional photonic crystal slabs to enhance the luminescence from Er3N@C80 fullerenes", Opt.

Commun. 282, 3637–3640 (2009).

33. Wen-Jie Wang, Yong-Fa Kong, Hong-De Liu, Qian Hu, Shi-Guo Liu, Shao-Lin Chen and Jing-Jun Xu, "Light-induced domain reversal in doped lithium niobate crystals", J. Appl. Phys. 105, 043105 (2009).

34. Yudong Li, Chong Xing, Yasheng Ma, Jianguo Tian, Jingjun Xu and Qian Sun "Parallel femtosecond laser direct writing in silica glass by multiple beams with different wavefront curvature" J. Opt. A. 11, 045601(2009).

35. Zu-Bin Li, Yi-Hong Yang, Xiang-Tian Kong, Wen-Yuan Zhou and Jian-Guo Tian. "Fabry–Perot resonance in slit and grooves to enhance the transmission through a single subwavelength slit", J. Opt. A: Pure Appl. Opt., 11: 105002(2009).

36. Zhang, YJ; Zhang, RY; Zhang, ZS, et al, "Surface polariton generation and fluorescence enhancement using a superlens",Journal of the optical society of American B-Optical Physics 26, 2337-2341 (2009)

37. Yu, XC; Song, F; Zou, CG, et al. "Temperature dependence of luminescence behavior in Er^{3+}/Yb^{3+} co-doped transparent phosphate glass ceramics", Optical Materials 31, 1645-1649 (2009)

38. Yu, XC; Song, F; Wang, WT, et al. "Effects of Ce3+ on the spectroscopic properties of transparent phosphate glass ceramics co-doped with Er^{3+}/Yb^{3+}", Optics Communications 282, 2045-2048 (2009)

39. Hua Cheng, Wei-Ping Zang, Zu-Bin Li, Wen-Yuan Zhou, and Jian-Guo Tian. "Nonparaxial Split-Step Method With Local One-Dimensional Scheme for Three-Dimensional Wide-Angle Beam Propagation", J. Lightw. Technol. 27: 2717-2723(2009).

40. Zhi-Bo Liu, Yan-Fei Xu, Xiao-Yan Zhang, Xiao-Liang Zhang, Yong-Sheng Chen, Jian-Guo Tian, "Porphyrin and Fullerene Covalently Functionalized Graphene Hybrid Materials with Large Nonlinear Optical Properties", J. Phys. Chem. B 113(29): 9681(2009).

41. En-Jun Wang, Wen-Sheng Yang and Ya-An Cao, "Unique surface chemical species on indium doped TiO_2 and their effect on the visible light photocatalytic activity", J. Phys. Chem. C 113, 20912-20917 (2009).

42. Yong-Qiang Cao, Tao He, LuSong Zhao, En-Jun Wang and Ya-An Cao, "Structure and phase transition behavior of Sn^{4+}-doped TiO_2 nanoparticles", J. Phys. Chem. C 113, 18121-18124 (2009).

43. Yong-Sheng Liu, Jiao-Yan Zhou, Xiao-Liang Zhang, Zhi-Bo Liu, Xiang-Jian Wan, Jian-Guo Tian, Tuo Wang, Yong-Sheng Chen, "Synthesis, characterization and optical limiting property of covalently oligothiophene-functionalized graphene material", Carbon 2009, 47: 3113-3121.

44. Xiaoyan Zhang, Zhibo Liu, Yi Huang, Xiangjian Wan, Jianguo Tian, Yanfeng Ma, Yongsheng Chen, "Synthesis, characterization and nonlinear optical property of graphene-C60 hybrid", J. Nanosci. Nanotechnol, 2009, 9(10): 5752-5756.

45. Xin Lv, Yi Huang, Zhibo Liu, Jianguo Tian, Yan Wang, Yanfeng Ma, Jiajie Liang, Shipeng Fu, Xiangjian Wan, Yongsheng Chen, "Photoconductivity of Bulk Films Based on Graphene Sheets," Small, 2009, 5(14): 1682.

46. Y. Liu, P. Chen, Z. H. Wang, F. Bian, L. Lin, S. J. Chang, and G. G. Mu, "Efficient Two Photon Absorption of CdSe CdS/ZnS Core Multishell Quantum Dots under the Excitation of Near Infrared Femtosecond Pulsed Laser", Laser Phys. 19 (9), 1886 - 1890 (2009)

47. Wei-Ping Zang, Hua Cheng, and Jian-Guo Tian. "A Novel Three-Dimensional Wide-Angle Beam Propagation Method Based on Split-Step Fast Fourier Transform", Chin. Phys. Lett., 2009, 26: 024202.

48. Zhang-Cheng Xu, Ya-Ting Zhang, Jørn M. Hvam and Yoshiji Horikoshi, "Inter-layer energy transfer through wetting-layer states in Bi-layer ingaas/gaas quantum-dot structures with thick barriers", Chin. Phys. Lett. 26, 057304 (2009).

49. Shaolin Chen, Xiangming Liu, Bo Fu, and Guoquan Zhang, "Nonvolatile two-color holographic recording in near-stoichoimetric lithium niobate crystals gated by incoherent ultraviolet lights", Chin. Opt. Lett.7, 67-69 (2009).

50. Hong-De Liu, Yong-Fa Kong, Wen-Jie Wang, Qi-Rui Liang, Shi-Guo Liu, Shao-Lin Chen and Jing-Jun Xu, "High-quality domain structure with ultraviolet light assisted domain inversion on LiNbO$_3$ crystals", Photorefractive Materials, Effects, and Devices. ISBN 978-3-00-027892-1, p142-143 (2009).

51. Zheng yi-fan , Xu xiaoxuan , Wang bin ,Qin zhe,Li jun-mei , The research of ultraviolet detection by using CCD, Proceedings of SPIE - The International Society for Optical Engineering, v 7384, 2009

52. Mi zhiqiang, Xu xiaoxuan,Li junmei,Wang bin , Wang yufang, Fabrication of the Nano-Structure Metal Film, Proc. Proceedings of SPIE Vol.7382,73822c(2009)

53. 高峰，许京军，张国权，张文定，"红宝石中的弱光非线性与超光速传播"，科学通报，54(7): 861~865（2009）。

54. 张艳峰，李玉栋，赵立华，刘洪冰，陈靖，崔国新，许京军，孙骞，"高斯光束中吸收双层球形微粒的横向光俘获"，物理学报 58(1)，258-263（2009）。

55. 叶青，李福新，刘宇，周文远，张春平，田建国，"基于频域 OCT 的生物组织折射率测量研"光电子.激光，20(1):126-129（2009）。

56. 龙绘锦，王恩君，董江舟，王玲玲，曹永强，杨文胜，曹亚安，"In 离子掺杂二氧化钛纳米管可见光催化活性的研究"，化学学报 67，1533-1538（2009）。

57. 曹永强，龙绘锦，陈咏梅，曹亚安，"金红石/锐钛矿混晶结构的 TiO$_2$ 薄膜光催化活性"，物理化学学报 25(6)，1088-1092（2009）。

58. 孔勇发，刘士国，刘宏德，许京军，"四价掺杂铌酸锂晶体"，红外与毫米波学报 28(3)，181-184（2009）。

59. 张铭，余华，张明浩，侯春霄，赵丽娟，"Tm^{3+}/Yb^{3+}共掺玻璃和玻璃陶瓷中蓝色上转换发光中的能量传递过程"，发光学报 30(3)，123-127（2009）。

60. 张俊杰，孙甲明，杨 阳，张新霞，刘海旭，W. Skorupa，M. Helm，"纳米硅微晶对于 Er 离子掺杂的 SiO$_2$ 薄膜的光致发光和电致发光的不同影响"，《材料科学与工程学报》27，135（2009）。

61. 杨 阳，孙甲明，张俊杰，张新霞，刘海旭，W. Skorupa，M. Helm，"离子注入缺陷局域掺杂的高效率硅 pn 结发光二极管"，《材料科学与工程学报》27，142（2009）。

62. 孙甲明，刘海旭，张俊杰，杨 阳，张新霞，W. Skorupa，M. Helm，"稀土离子注入的高效率硅基纳米材料电致发光器件"，《材料科学与工程学报》27， 121（2009）。

63. 张新霞，孙甲明，张俊杰，杨 阳，刘海旭，"半绝缘 Si/SiO$_2$ 超晶格结构在交流电场下的电致发光特性"《材料科学与工程学报》27，129（2009）。

64. 宋 宁，徐晓轩，张存洲，"基于正交信号校正和 iPLS 的烃源岩红外漫反射光谱定量分析"，光谱学与光谱分析，29（2）378-381（2009）。

65. 潘雷霆，孙文武，齐继伟，吴限，宋昆，胡芬，张心正，许京军，"佛波酯诱导大鼠滑膜细胞骨架改变的研究"，生物化学与生物物理进展，36: 83~87（2009）。

专利∕Patents

申请专利∕ Patents Applied

[1] 200910070175.9；柱透镜进行像散纠正的光谱仪；发明；徐晓轩，王斌。

[2] 200910070081.1；基于单模光纤的等离子体火焰共焦扫描装置；发明；徐晓轩，王斌。

[3] 200910070082.6；腔内体光栅的窄带 532nm 激光器；发明；王斌，徐晓轩，郑一凡。

[4] 200910068819.0；掺锡铌酸锂晶体；发明；刘士国，孔勇发，王利忠，陈绍林，黄自恒，张玲，许京军。

[5] 200910068853.8；一种锆铁锰三掺铌酸锂晶体及其制备方法；发明；孔勇发，刘富才，刘士国，黄自恒，陈绍林，张玲，许京军。

[6] 200910068854.2；一种锆铜铈三掺铌酸锂晶体及其制备方法；发明；孔勇发，刘富才，刘士国，黄自恒，陈绍林，张玲，许京军。

授权专利∕ Patents Approved

[1] ZL200610129356.0；掺锆铌酸锂晶体；发明；刘士国，孔勇发，赵艳军，许京军，陈绍林，黄自恒，张玲。

[2] ZL200710057516.X；一种制备三元素掺杂高活性二氧化钛催化剂的方法；发明；曹亚安，王恩君，赵路松，龙绘锦。

[3] ZL200710058844.1；铌酸锂 pn 结及其制备方法；发明；孔勇发，黄自恒，肖罗生，陈绍林，刘士国，张玲，许京军。

[4] ZL200710057399.7；一种双掺铌酸锂晶体及其制备方法；发明；阎文博，李养贤，师丽红，孔勇发。

专利∕Patents

国际合作与交流／International Cooperation and Exchange

来访人员名单/Visitors List

序号	姓名	国家或地区	单位	职称或职位	来访时间	来访目的
1.	周瑜	美国	马里兰大学巴尔的摩分校	博士	2009.8.19-21	学术交流
2.	区泽宇	美国	印地安那-普渡大学印地安那坡理斯分校	教授	2009.7.13-18	讲学
3.	Robert A. Taylor	英国	Oxford University	Professor	2009.5.24-2009.5.29	访问讲学
4.	贾宝华	澳大利亚	Swinburne University of Technology	博士	2009.4.20	学术交流
5.	Keith A. Nelson	美国	MIT	教授	2009.6.13-17	工作访问合作交流
6.	Christopher A. Werley	美国	MIT	博士生	2009.9.28-10.4	合作交流
7.	Andrii Ilyin	乌克兰	乌克兰科学院物理所	研究员	2009.2.16-3.14 2009.7.4-8.15	合作研究
8.	Uyugun Valiev	乌兹别克斯坦	Mirzo Ulugbek 国立大学	教授	2009.5.20-7.20	合作研究
9.	Peter Hertel	德国	奥斯纳布鲁克大学	教授	2009.9.1-10.15	系列讲座
10.	Baohua Jia	澳大利亚	Swinburne 技术大学		2009.4.20-4.21	学术交流
11.	Valive	乌兹别克斯坦	Mirzo Ulugbek National University of Uzbekistan	教授	2009.5	工作访问学术交流
12.	Alex	德国	德累斯顿工业大学	教授	2009.8	学术交流
13.	Georg Roth	德国	RWTH-Aachen University	教授	2009.9.8-14	讲学
14.	Hu Xinhua	美国	东卡罗来那大学	教授	2009.7	学术交流
15.	Arturo Pirson-Chavez	美国	Optical Sciences Center in University of Arizona	Associate Professor	2009.11．9	学术交流

国际合作与交流／International Cooperation and Exchange

出访人员名单/Personnel exchange Researchers List

序号	姓名	国家或地区	单位	职称或职位	出访时间	出访目的
1.	楼慈波	德国	克劳斯塔尔工业大学物理系	副教授	2009.4-2009.10	合作研究
2.	宋峰	香港	香港城市大学	教授	2009.3-2009.4	合作研究
3.	宋峰	台湾	台湾大学	教授	2009.9.25-30	会议

研究生交流情况/Personnel exchange Students List

序号	姓名	国家或地区	单位	博士生/硕士生	出访时间	出访目的
1.	齐新元	澳大利亚	澳大利亚国立大学	博士生	2008.9-2009.9	联合培养
2.	窦宜领	美国	阿肯色大学	博士生	2009.1-2009.6	访问学习
3.	许宁宁	美国	阿肯色大学	博士生	2009.1-2010.4	访问学习
4.	李俊	斯洛文尼亚	Stefan 研究所	博士生	2009.2	合作研究
5.	王文杰	澳大利亚	国立大学	博士生	2008.9	联合培养
6.	张新星	德国	洪堡大学	博士生	2009.7	联合培养
7.	刘富才	日本	东北大学	博士生	2009.10	联合培养
8.	周凯迪	德国	德累斯顿工业大学	博士生	2009.10	联合培养
9.	王青如	香港	香港城市大学	博士生	2009.1-2010.4	合作研究

引进人才名单/New Staff

序号	姓名	性别	出生年月	职称	研究方向
1	潘雷霆	男	1983.8	讲师	光子学与技术
2	蔡卫	男	1983.9	讲师	光子学与技术
3	陈树琪	男	1979.7	讲师	非线性光学

国内、国际会议报告/Talks at Conferences

1. Z. Chen and P. Zhang, "Manipulation of light waves with reconfigurable ionic-type photonic structures", the Sixth IMACS International Conference on Nonlinear Evolution Equations and Wave Phenomena, Georgia, March, 2009.(邀请报告)

2. 宋峰，"Experimental study and theoretical simulation for high gain compact Er3+-Yb3+-codoped fiber laser"，2009 光学仪器与技术国际会议，上海（2009.10.19-2009.10.22）。（大会报告）

3. 宋峰，"固体激光器热透镜焦距的测量"，第十九届全国激光学术会议，北京 (2009.10.18-2009.10.21)。（大会报告）

4. 张国权，"固体中光速调控研究的若干进展"，全国信息光学与光子器件学术会议 (CIOC2009)，青岛(2009.8.2-6)（邀请报告）

5. 孔勇发，刘士国，赵艳军，吴胜青，陈绍林，许京军，"掺锆铌酸锂晶体"，第 15 届全国晶体生长与材料学术会议，宁波（2009.11.6-10）。（邀请报告）

6. 武莉，粟伟伟，孔勇发，许京军，"$K_{1-x}Na_xSr_4(BO_3)_3(0≤x≤0.5)$的晶体结构研究"，第 15 届全国晶体生长与材料学术会议，宁波（2009.11.6-10）。（优秀口头报告）

7. 武莉，粟伟伟，孔勇发，许京军，"$K_{1-x}Na_xSr_4(BO_3)_3(0≤x≤0.5)$的晶体结构研究"，第十届全国 X-射线衍射学术大会暨国际衍射数据中心（ICDD）研讨会，上海（2009.10.11-18）。（青年优秀论文奖）

8. Yanfei Tu, Guoquan Zhang, Zhaohui Zhai, and Jingjun Xu, " Addressable Optical Buffer via Angular Multiplexing in an Electromagnetically Induced Transparency Solid ", FWK4, Frontiers in Optics 2009/Laser Science XXV, October 11-15, 2009, San Jose, California, USA.

9. Guoquan Zhang, Lei Xu, Ningning Xu, Fang Bo, Feng Gao, Jingjun Xu, Kar Pong LOR, and Kin Seng Chiang, " active control on slow and fast lights at arbitrary wavelength in BCB polymer ", Conference Program & Book of Abstracts pp. 120, International Commission for Optics Topical Meeting on Emerging Trends & Novel Materials in Photonics, October 7-9, 2009, Delphi, Greece

10. Jun Lei, Guoquan Zhang, Jingjun Xu, and Kin Wah Yu, " Narrow-bandwidth spectral filter with extraordinary transmission through sub-wavelength metal slit ", Conference Program & Book of Abstracts pp. 225, International Commission for Optics Topical Meeting on Emerging Trends & Novel Materials in Photonics, October 7-9, 2009, Delphi, Greece

11. Guoquan Zhang, Lei Xu, Ningning Xu, Fang Bo, Feng Gao, Jingjun Xu, Kar Pong LOR, and Kin Seng Chiang, " Slow and fast lights in BCB Polymer induced by the thermo-optic nonlinearity ", Oral 2-2B-1, The 8th International Conference on Optical Communications and Networks (ICOCN2009), Sept. 15-17, 2009, Beijing, China

12. Fang Bo, Guoquan Zhang, and Jingjun Xu, "Slow light in photorefractive GaAs-AlGaAs multiple quantum wells via nondegenerate two wave mixing", T8-3, Proceedings of Topical Meeting in Photorefractive Materials, Effects, and Devices--Control of Light and Matter, June 11-14, 2009, Bad Honnef, Germany.

13. Feng Gao, Guoquan Zhang, Wending Zhang, and Jingjun Xu, "Nondegenerate two wave coupling like mechanism and paraxial energy transport of a focused Gaussian beam in the nonlinear medium", P2-24, Proceedings of Topical Meeting in Photorefractive Materials, Effects, and Devices--Control of Light and Matter, June 11-14, 2009, Bad Honnef, Germany.

14. Daohong Song, Cibo Lou, Liqin Tang, Yi hu, Jingjun Xu and Zhigang Chen, "Self-trapping of vortex at the interface of 2D photonic lattices". The International Conference on Nanophotonics, Harbin, China, May 2009

15. Yi Hu, Cibo Lou, Peng Zhang, Sheng Liu, Jianlin Zhao, Jingjun Xu, Jianke Yang and Zhigang Chen, "Observation of two-dimensional quasi-localized solitons with saddle-shaped diffraction and hybrid nonlinearity" The conference on Lasers and Electro-Optics(CLEO) and The Quantum Electronics and Laser Science Conference(QELS). Baltimore, USA, May 2009

16. Yi hu, Cibo Lou, Peng Zhang, J.Zhao, J. Xu, J.Yang and Zhigang Chen,"Self-Trapping of Light Due to Balance between Saddle-Shaped Diffraction and Hybrid Nonlinearity" OSA's Frontiers in Optics, San Jose, USA, October   2009

17. Zhuoyi Ye, Cibo Lou, Daohong Song, Liqin Tang and Zhigang Chen, "Power dependent defect solitons interaction in focusing waveguide arrays" SPIE international Conference on optical instrument and Technology(OIT) ,Shanghai ,China, October 2009.

18. Lihua Zhao, Yudong Li, Jiwei Qi , Jingjun Xu, Qian Sun "Study of the energy transmission in the nano-fiber with material absorption", International Conference on Nanoscience & Technology，China, September 1-3, 2009

19. Zheng yi-fan , Xu xiaoxuan , Wang bin ,Qin zhe,Li jun-mei , The research of ultraviolet detection by using CCD, Proceedings of SPIE - The International Society for Optical Engineering, v 7384, 2009

20. Mi zhiqiang, Xu xiaoxuan, Li junmei,Wang bin , Wang yufang, Fabrication of the Nano-Structure Metal Film, Proc. Of SPIE Vol.7382,73822c(2009)

21. Yongfa Kong, Shiguo Liu, Shaolin Chen, Jingjun Xu, "Zirconium doped lithium niobate crystals", Topical Meeting of Photorefractive Materials, Effects, and Devices—Control of Light and Matter (PR'09), Bad Honnef, Germany, June 11-14, 2009, pp.32-33.

22. Hongde Liu, Yongfa Kong, Wenjie Wang, Qirui Liang, Shiguo Liu, Shaolin Chen, Jingjun Xu, "High-quality domain structure with ultraviolet light assisted domain inversion on LiNbO3 crystals", The 12th Topical Meeting on "Photorefractive Materials, Effects, and Devices - Control of Light and Matter", Bad Honnef, Germany, Jun 11-14(2009).

23. Xiaoqing Yan, Zhibo Liu, Xiaoliang Zhang, Jianguo Tian, "Study on ultrafast optical nonlinearities by using Z-scan method with arbitrary polarized lights" The 9th international conference on fundamental ultrafast processes in chemistry, biology, and physics, Beijing, August 8-13 (2009).

24. Xiaoliang Zhang, Xiaoqing Yan, Xin Zhao, Zhibo Liu, Jianguo Tian, "Solvent effects on dispersion and optical limiting properties of hydroxyl group modified multi-walled carbon nanotubes", International Conference on Organic Photonics & Electronics 2009 The 11th International Conference on Organic Nonlinear Optics, Beijing, September 20-25 (2009).

25. Shuqi Chen, Weiping Zang, Xin Liu, Jianguo Tian, "Study on Z-scan characteristics for one-dimensional nonlinear photonic band gap materials with defect mode", The International Conference on Nanophotonics 2009, May, 11-14.

26. Chunping Zhang, Meixiu Sun, Jianguo Tian, Guiying Chen, Shengwen Qi, Qing Ye, Jin Wang "Effect of Surface Roughness on Determination of Tissue Optical Properties and Light Distribution in Intralipid", Progress In Electromagnetics Research Symposium, Moscow, Russia, Aug 17-21(2009).

27. 2009 年硅基光电子材料及器件会议，北京，6 月 27 至 30 日，富硅 SiOB2B 基质中 Er 和纳米硅耦合发光体系的电场效应， 孙甲明，口头报告题目。

28. 樊学芳，"自适应固体激光器"，第十九届全国激光学术会议，北京（2009.10.18-2009.10.21）。

29. 潘雷霆，吴限，张心正，许京军，"外源性一氧化氮以亚硝基化途径诱导人嗜中性粒细胞钙库释放机制的探讨"，第十一届中国生物物理大会，桂林（2009.7.12-16）

30. 潘雷霆，吴限，张心正，许京军，"Intensity-dependent fast modulation of the phototoxic effect of ultraviolet irradiation on human red blood cells"，第八届生物医学光子学与成像技术国际学术研讨会，武汉（2009.8.8-10）

31. 孙同庆，陈鸿，陈猛，周晓东，武莉，孔勇发，许京军，"立方相四磷酸镧铯的合成与晶体结构"，第 15 届全国晶体生长与材料学术会议，宁波（2009.11.6-10）。

32. 刘宏德，王文杰，孔勇发，曾浩，梁启锐，陈绍林，刘士国，许京军，"铌酸锂晶体的光辅助极化反转研究"，第 15 届全国晶体生长与材料学术会议，宁波（2009.11.6-10）。

33. 陈树琪，臧维平，Axel Schülzgen，刘欣，田建国，Nasser Peyghambarian，"一维非线性光子带隙材料 Z 扫描特性研究"，中国物理学会 2009 年秋季学术会议.，上海，（2009. 9. 17-20）

34. 赵欣，田凤仪，张校亮，刘智波，田建国，"碳纳米管及石墨烯材料光学非线性及其光限制效应研究" 中国物理学会 2009 年秋季学术会议，上海，（2009.9.17-20）。

35. 刘欣，臧维平，陈树琪，田建国，"基于一维光子带隙材料的复合型光限制研究",中国物理学会 2009 年秋季学术会议，上海 （2009.9.17-20）

36. 栗建兴，臧维平，田建国，"真空中紧聚焦强激光束加速电子模拟研究",中国物理学会 2009 年秋季学术会议，上海 （2009.9.17-20）

37. 余璇，刘智波,田建国，"二硫化碳双光子吸收性质的理论和实验研究" 第十届全国计算化学学术会议，杭州，（2009.10.22-25）。

38. 叶青，李福新，刘宇，周文远，张春平，田建国 "双波长光学相干层析成像研究"，2009 全国信息光学与光子器件学术会议，青岛（2009.8.4-7）。

主办国内、国际会议/Conferences Sponsored by the Laboratory

量子光学讲习班（2009.7.13-7.18；天津）

2009 年 7 月 13 日至 18 日，重点实验室在泰达应用物理学院举办了《量子光学》讲习班。讲习班邀请美国印地安那-普渡大学印地安那坡理斯分校区泽宇教授就量子光学基础和实验进行了为期一周的授课。具体授课内容包括光的全量子理论的引入、量子的相干理论、多模光场的处理、态函数的转换、双光子符合测量和多光子干涉等。本次讲习班共有来自天津大学、南京大学、中国科技大学、北京航空航天大学以及本校的近 80 名师生报名参加。

本次讲习班的举行为参加本次讲习班的师生提供了系统学习量子光学理论和实验的平台，同时也为广大师生提供了进一步交流的平台，在一定程度上提高了重点实验室学术氛围。

南开大学弱光非线性光子学教育部重点实验室/ The Key laboratory of Weak Light Nonlinear Photonics (Nankai University, Tianjin 300457), Ministry of Education, China

学术组织与期刊任职/Academic Service

国内学术组织任职/Service to the Domestic Professional Societies

序号	姓名	任职机构	职位	任期
1	许京军	中国高校知识产权研究会	副理事长	2008-
2	许京军	中国光学学会	理事	2006-
3	许京军	天津市激光学会	副理事长	2009-2014
4	宋峰	中国仪器仪表学会光机电技术与系统集成分会	第一届常务理事	2006-2010
5	孔勇发	中国材料研究学会青年工作委员会	理事	2008－2011
6	孔勇发	天津市硅酸盐学会	晶体生长与材料专业委员会副主任	2006-2010
7	宋峰	中国仪器仪表学会光机电技术与系统集成分会	常务理事	
8	宋峰	天津市激光学会	副理事长	2009-2014
9	孙骞	天津市光电子学会	常委	2006-
10	宋峰	教育部高等学校物理基础课程教学指导分委员会	委员，高等学校文科类物理课程教学研究协作组成员	2006-2010
11	宋峰	教育部大学物理基础课程教指委暨医药类基础课程教指委 医药物理协作组	副组长	2008-2010
12	徐章程	中国教育技术协会多元智能专业委员会	主任	2008-2009
13	徐章程	中国电子学会半导体集成分会	委员	2006-2011
14	孙骞	中国光学学会光电技术委员会	委员	2006-
15	徐晓轩	中国仪器仪表学会分析仪器分会近红外光谱专业委员会	学术委员	2009-2013
16	宋峰	固体激光技术国防科技重点实验室	第三届学术委员会委员	2007-2010
17	宋峰	南京师范大学物理系	兼职教授	2006-2010
18	宋峰	德州学院物理系	兼职教授	2007-2011
19	宋峰	南通大学	兼职教授	2008-2012

学术组织与期刊任职/Academic Service

国内期刊任职/Service to the Domestic Journals

序号	姓名	任职机构	职位	任期
1	许京军	Frontiers of Physics in China	编委	2008-2011
2	宋峰	Applied Optics	编委	2009-2012
3	许京军	《光学学报》	副主编	2008-
4	宋峰	大学物理	副主编	2009.5-
5	许京军	《红外与毫米波学报》	编委	
6	许京军	《物理》	编委	2007-2011
7	许京军	《物理学进展》	编委	2009-2012
8	许京军	Chinese Physics Letters	编委	2009-
9	孔勇发	《激光技术》	编委	2007-2010
10	张国权	《激光技术》	编委	2007-2011
11	张国权	激光与光电子学进展	编委	2010-2013
12	孙骞	《激光技术》	编委	2006-2010

国内期刊任职/Service to the Domestic Journals

序号	姓名	任职机构	职位	任期

获奖情况/Awards & Honors

材料物理专业建设与人才培养
南开大学教学成果二等奖
获得者：孔勇发　孙同庆　李兵　刘宏德　许京军

小型自动光纤拉丝机和特种光纤的拉制
第十一届"挑战杯"全国大学生课外学术科技作品竞赛国家二等奖 2009.11
获得者：程振洲、朴文益、蔡莹莹、韩霈泽、杜鹏、韩冰、韦晨
指导教师：宋峰

获奖学生/Award for excellent students
南开大学三好学生：　　　　王俊俏　　　　　南开大学研究生优秀共产党员标兵：　李威
南开大学优秀学生干部：　　崔磊　　　　　　南开大学泰达学院优秀党员：　　王俊俏

南开大学奖学金：
特等奖：　　　栗建兴
一等奖学金：齐新元　张文定　胡　毅　鄢小卿
二等奖学金：刘建彬　祁轶舫　王俊俏　张雅婷　周波　程化　李亚东
三等奖学金：杨程亮　翟召辉　徐　雷　胡　男　张校亮　马雅盛

南开大学周恩来奖学金：　　祁轶舫
泰达奖教金：齐新元

获奖集体/Award for group
天津市优秀研究生集体：泰达应用物理学院

获奖情况/Awards & Honors

学位论文/Dissertations

1. 博士学位论文 Dissertation for Doctoral Degree

[1] 李威，光敏材料中若干弱光非线性光学效应研究；导师：许京军

[2] 潘雷霆，生物荧光成像与人嗜中性粒细胞信号转导动力学的研究；导师：许京军

[3] 蔡卫，若干小尺度体系中相干光学效应的研究；导师：许京军

[4] 宋道红，光诱导光子晶格中涡旋光传播特性的研究；导师：陈志刚

[5] 涂燕飞，$Pr^{3+}:Y_2SiO_5$ 晶体中基于电磁感应透明的光脉冲存储和角度复用；导师：许京军

[6] 陈树琪，光束在体材料和周期性微结构材料中的传播及应用研究；导师：田建国

[7] 韩琳，稀土掺杂激光晶体中无辐射机制的研究及其对离子发光性质的影响；导师：宋峰

[8] 于晓晨，稀土掺杂透明磷酸盐玻璃陶瓷的制备与发光特性研究；导师：宋峰

[9] 宋宁，非均匀介质红外光学及光谱学性质研究；导师：俞刚

[10] 曹永强，高活性 TiO_2 基光催化剂的制备及其活性机理研究；导师：曹亚安

2. 硕士学位论文 Dissertation for Master Degree

[1] 王慎之，金属微结构中光传播的 FDTD 研究；导师：孙骞

[2] 钱学波，双电荷注入法对铌酸锂晶体中的锂含量影响研究；导师：孙骞

[3] 刘龙昌，紫外光敏有机玻璃的制备和优化；导师：张心正

[4] 祁国春，基于光流体的染料激光器的基础研究；导师：禹宣伊

[5] 弭志强，表面等离子激元共振金属薄膜微结构制备及拉曼增强光谱研究；导师：徐晓轩

[6] 陈晨，MBE 生长短周期 InGaAs/GaAs 超晶格 VECSELs 有源区的结构和退火研究；导师：姚江宏

[7] 崔楠，光泵浦垂直外腔表面发射半导体激光器 InGaAs/GaAs 应变量子阱有源区的制备及研究；导师：姚江宏

[8] 罗青青，III-V 族半导体三元含磷化合物的 MBE 生长与拉曼光谱研究；导师：邢晓东

[9] 胡茜，铌酸锂晶体载流子的调控及其 pn 结的制备；导师：孔勇发

[10] 窦树岗，铌酸锂晶体缺陷结构的能学计算；导师：孔勇发

[11] 陈喜杰，溶胶-凝胶法制备长余辉发光材料及其发光机理研究；导师：徐章程

[12] 王磊磊，镶嵌在氧化铝纳米孔阵列中金属材料的光学性质；导师：徐章程

[13] 陈凯，宽带荧光和频效应的理论分析与模拟；导师：赵丽娟

[14] 詹鹤，铌酸锂周期极化工艺研究；导师：陈云琳

[15] 刘刚，掺镁近化学计量比铌酸锂全波长转换器的研究；导师：陈云琳

[16] 孙建成，深紫外非线性光学材料的探索与结构解析；导师：武莉

[17] 于晓明，新型稀土掺杂硼酸盐荧光粉结构和发光性质研究；导师：武莉

[18] 吕玮，稀土离子掺杂钨酸镧钾的合计及光谱性质；导师：孙同庆

[19] 付世鹏，周期性层状克尔介质的非线性光学调控研究；导师：田建国

[20] 杨一宏，透射增强机制及结构参数的研究；导师：田建国

[21] 李行，嵌入式光电成像系统的设计与调试；导师：田建国

[22] 邢冲，硅玻璃中飞秒激光微加工技术研究；导师：李玉栋

[23] 李腾，LD 抽运 1.54um 铒镱共掺磷酸盐玻璃激光器的上转换研究；导师：宋峰

[24] 曲菲菲，中药玄参荧光光谱研究；导师：宋峰

[25] 程振洲，超短长度铒镱共掺超荧光光纤光源的研究；导师：宋峰

Experimental observation of subluminal and superluminal light propagation in rhodamine 6G-doped polymethyl methacrylate

Wending Zhang,[1,2] Feng Gao,[1,2,a] Guoquan Zhang,[1,2] Wei Li,[1,2] Xinzheng Zhang,[1,2] and Jingjun Xu[1,2]

[1]*The MOE Key Laboratory of Weak Light Nonlinear Photonics, Nankai University, Tianjin 300457, People's Republic of China*
[2]*Photonics Center, School of Physics, Nankai University, Tianjin 300071, People's Republic of China*

Nondegenerate two-wave coupling process and group velocity change in the paraxial part of an intensity-modulated and focused transverse electromagnetic beam (TEM_{00} beam in the article) was observed in the rhodamine 6G(R6G)-doped polymethyl methacrylate (PMMA) but not in the pure PMMA. The typical superluminal result was -5.1 m/s and the subluminal result was 9.19 m/s, respectively. Furthermore, the results provide a support to our former conclusion that nondegenerate two-wave couplinglike mechanism could be used to change the group velocity of the paraxial part of a focused TEM_{00} beam in materials with nondegenerate two-wave coupling process. © *2009 American Institute of Physics*. [doi:10.1063/1.3254229]

Controlling the group velocity of a light pulse has already become the frontier of modern optics of various applications such as real-time optical delay lines and optical buffers. Several methods have been proposed to manipulate the material dispersion in order to control the group velocity of light pulse,[1–9] while most of them require a separated pump beam to get a large change in the group velocity. In 2003, Bigelow *et al.*[6] found self-induced subluminal light propagation in ruby by the creation of a spectral hole via coherent population oscillations. A detailed theoretical analysis of the propagation of a pulse composing different temporal frequencies showed the same result in the ruby[7] with only subluminal light propagation. Yet the ruby requires a strong beam to exploit the refractive index dispersion and a focused transverse-electromagnetic beam (usually TEM_{00} beam) is usually introduced other than a plane wave. In 2008, we observed self-induced superluminal propagation in the paraxial part of a focused TEM_{00} beam in ruby with little deformation, which was explained as the result via the coupling between different spatial frequencies in the modulated Gaussian beam, i.e., nondegenerate two-wave couplinglike mechanism (NDTWC-like mechanism).[8] This result extended the application of ruby for its pump-beam-free property in both the superluminal and the subluminal light fields. However, the preparation of the ruby is complicated and expensive. Cheap materials with good mechanical characteristics are needed for various applications and polymethyl methacrylate (PMMA) is one of the candidates. In this letter, we report our progress on the group velocity control in the PMMA doped with rhodamine 6G (R6G) of low concentrations. The energy transfer was observed with a standard NDTWC configuration and similar paraxial group velocity change as that in ruby was observed with a modulated and focused TEM_{00} beam by using the same configuration as that in ruby.[8] At the same time, these phenomena could not be observed in the pure PMMA. The results showed R6G-doped PMMA could be applied to control the group velocity via NDTWC-like mechanism, they also provided a support to our former conclusion that the NDTWC-like mechanism

should work in the material with a NDTWC process.[8]

Organic materials have been introduced in the area of photonics for a long time,[10–14] in which the PMMA is important for its excellent properties such as high transmittance, good mechanical characteristics, and low cost.[10] Many new materials have been developed from PMMA by doping different functional impurities such as photo initiator and fluorescent dye, depending on the requirements of concrete applications.[15–17] Because the ruby in which the group velocity control was realized via NDTWC-like mechanism belongs to saturable resonant media,[18] in the experiment, PMMA was doped with R6G of low concentration (0.0017 wt %) to adjust its absorption, and a sample which looks orange with $\alpha=1.856$ cm^{-1} at 532 nm and a thickness of 2.9 mm were prepared. Meanwhile, a pure PMMA sample which looks totally transparent with $\alpha=0.09$ cm^{-1} at 532 nm and the same thickness was also prepared for comparison.

Based on the fact that the NDTWC-like mechanism is the coupling between different angular frequency components at different spatial frequencies in a modulated and focused TEM_{00} beam and is of the same physics essence as the NDTWC process, we have made a conclusion in the former work that the NDTWC-like mechanism should work in the material with a NDTWC process.[8] Before the R6G-doped PMMA and the pure one were applied to control group velocity with the configuration of the NDTWC-like mechanism, the NDTWC process in both samples was measured first.

With a typical NDTWC configuration,[18] two beams at 532 nm with a 12 kHz frequency difference were interfered in the sample. The pump beam was 152.7 mW and the probe beam was 52.4 mW. The crossing angle between the two beams was 3.7 degree in air. The temporal traces of the transmitted pump beam, the transmitted probe beam, and the driving voltage of piezoelectric mirror providing the frequency shift in the two beams were all shown in Fig. 1. Energy transfer between two beams was observed in R6G-doped PMMA. The probe and the pump oscillated out of phase but with the same frequency as that of the driving ramp voltage, as shown in Fig. 1(a). This indicates clearly the existence of the NDTWC process in R6G-doped PMMA. No such energy

[a]Electronic mail: fenggao@nankai.edu.cn.
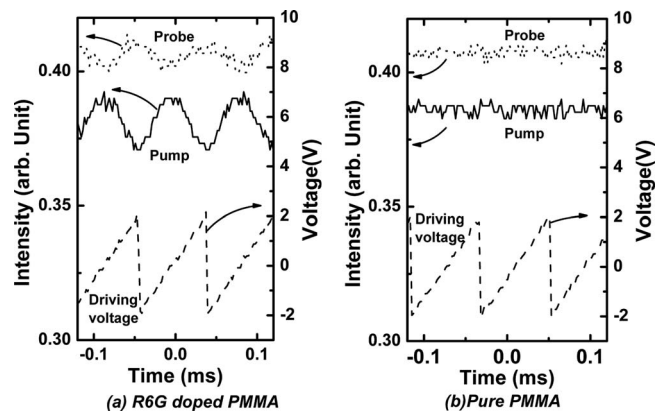
FIG. 1. The results of NDTWC-process in pure PMMA and R6G-doped PMMA. Obviously energy transfer could be observed in the R6G-doped PMMA. No NDTWC-process could be observed in the pure PMMA.

FIG. 3. Frequency response of the R6G-doped PMMA at $Z=300$ mm where the delay was positive and $Z=352$ mm where the delay was negative. Because the pulse introduced in the experiment was a Gaussian pulse, the frequency was defined as the reciprocal of the pulse width.

transfer and temporal oscillation were observed in pure PMMA. With a typical Z-scan setup, the nonlinearity was confirmed mainly from the thermally induced optical nonlinearity[19] and the thermo-optic nonlinear coefficient was measured to be 1.0×10^{-5} K^{-1}.

According to the former conclusion,[8] the NDTWC-like mechanism should work in the samples with a NDTWC process, for they were of the same physics essence. Thus the superluminal and subluminal propagation with the paraxial energy transfer in the focused TEM$_{00}$ beam should be observed in the R6G-doped PMMA, while not in the pure PMMA.

The configuration of measuring the group velocity due to the NDTWC-like mechanism is all the same as that in ruby.[8] The typical temporal traces of the transmitted paraxial signal beam with sample at different Zs indicating the distance between the sample and the focus lens are shown in Fig. 2 for both R6G-doped and pure PMMA. The modulated input pulse in the experiment was a 10 ms Gaussian pulse with a peak power of 113.5 mW and a background power of 32.8 mW. Obvious group velocity change could be observed in the R6G-doped PMMA which is presented in the Fig. 2(a) while not in the pure one shown in Fig. 2(b). In Fig. 2(a), both subluminal and superluminal light propagation could be observed. The deformation of the paraxial signal at different Zs was similar to that in ruby. Group velocities of 9.19 and -5.1 m/s were achieved at $Z=342$ and 346 mm where there

was almost no deformation of the pulse, respectively. The delay-bandwidth product of the sample is 0.016 at $Z=342$ mm and smaller than that of ruby (around 0.037),[6] but there is methods to increase it[20] in the applications. In Fig. 2(b), we only gave a typical result of pure PMMA with $Z=342$ mm, for there was no obvious deformation of the pulse and no group velocity change, and the results at other positions were the same. Obviously, the results of group velocity control in Fig. 2 were in accordance with the results of the NDTWC experiment in Fig. 1, which indicates the mechanism of the group velocity change is the NDTWC-like mechanism.

Further experiments showed that not only the deformations at different Zs but also the response behavior of the modulation frequency (where the modulation frequency was defined as the reciprocal of the pulse width of the Gaussian pulse) in the doped PMMA were similar to those of ruby. The modulation frequency responses at $Z=300$ mm with a positive delay and $Z=352$ mm with a negative delay were shown in Fig. 3. The absolute value of the time delay decreases rapidly to zero with the increase in the modulation frequency.

Since the phenomenon is based on the NDTWC-like mechanism and of the same physics essence of the NDTWC process, i.e., the thermo-optic effect in the doped PMMA, the very steep dispersion slope of the phase coupling coefficient makes the dispersion from the material and dopant negligible.[9] As the concentration of R6G increases, the absorption of the material with the thermo-optic nonlinearity would also increase. We could handle the phenomenon via changing the condition of the coupling such as intensity or modulation frequency of the beam. Changing the absorption of the sample, that is, adjusting the doping concentration of the sample or simply changing the working wavelength was also applicable.

The results presented above indicate that R6G-doped PMMA is one of the candidates to generate self-induced and pump-free subluminal and superluminal light propagation. The concentration of R6G determines its absorption and nonlinear effect. Therefore, one could easily adjust the characters of the doped PMMA by changing the R6G concentration, which provides additional agility to practical applications.

The above result also shows that, in the R6G-doped PMMA with a NDTWC process, group velocity control can be realized via NDTWC-like mechanism, while in the pure

FIG. 2. Temporal profiles of the transmitted paraxial pulses with different Zs in pure PMMA and R6G-doped PMMA.

PMMA where the NDTWC process does not exist, no group velocity change based on the NDTWC-like mechanism is observed. This is also a support to our former conclusion that the NDTWC-like mechanism should exist in the material with a NDTWC process.[8]

In conclusion, we found that R6G-doped PMMA was suitable to realize group velocity control via NDTWC-like mechanism. Both superluminal and subluminal results were achieved and the frequency response was similar to that of ruby. The NDTWC experiment in the two samples not only confirmed the existence of the NDTWC process in R6G-doped PMMA other than pure PMMA but also provided an experimental support to our former conclusions that NDTWC-like mechanism should exist in the material with a NDTWC process,[8] which will surely present us a basic principle to find more multifunctional nonlinear medium and to control the group velocity more conveniently.

[1] L. V. Hau, S. E. Harris, Z. Dutton, and C. H. Behroozi, Nature (London) **397**, 594 (1999).
[2] A. V. Turukhin, V. S. Sudarshanam, M. S. Shahriar, J. A. Musser, B. S. Ham, and P. R. Hemmer, Phys. Rev. Lett. **88**, 023602 (2001).
[3] C. P. Kuo, U. Osterberg, C. T. Seaton, G. I. Stegeman, and K. O. Hill, Opt. Lett. **13**, 1032 (1988).
[4] S. H. Lin, K. Y. Hsu, and P. Yeh, Opt. Lett. **25**, 1582 (2000).
[5] H. Su and S. L. Chuanga, Appl. Phys. Lett. **88**, 061102 (2006).
[6] M. S. Bigelow, N. N. Lepeshkin, and R. W. Boyd, Phys. Rev. Lett. **90**, 113903 (2003).
[7] Q. Yang, J. Seo, B. Tabibi, and H. Wang, Phys. Rev. Lett. **95**, 063902 (2005).
[8] F. Gao, J. Xu, G. Zhang, F. Bo, and H. Liu, Appl. Phys. Lett. **92**, 021121 (2008).
[9] G. Zhang, F. Bo, R. Dong, and J. Xu, Phys. Rev. Lett. **93**, 133903 (2004).
[10] W. J. Tomlinson, E. A. Chandross, H. P. Weber, and G. D. Aumiller, Appl. Opt. **15**, 534 (1976).
[11] S. Ducharme, J. C. Scott, R. J. Twieg, and W. E. Moerner, Phys. Rev. Lett. **66**, 1846 (1991).
[12] W. E. Moerner and S. M. Silence, Chem. Rev. (Washington, D.C.) **94**, 127 (1994).
[13] Y. Zhang, R. Burzynski, S. Ghosal, and M. Casstevens, Adv. Mater. **8**, 111 (1996).
[14] L. Yu, W. K. Chan, Z. H. Peng, and A. Gharavi, Acc. Chem. Res. **29**, 13 (1996).
[15] F. Havermeyer, C. Pruner, R. A. Rupp, D. W. Schubert, and E. Krätzig, Appl. Phys. B: Lasers Opt. **72**, 201 (2001).
[16] R. A. Rupp, B. Yao, Y. Zheng, N. Menke, Y. Wang, W. Dong, W. Zhao, Y. Chen, M. Fan, J. Xu, and M. Fally, Phys. Status Solidi B **244**, 2138 (2007).
[17] Y. Deng, Y. Sun, P. Wang, D. Zhang, X. Jiao, H. Ming, Q. Zhang, Y. Jiao, and X. Sun, Chin. Phys. Lett. **24**, 954 (2007).
[18] I. McMichael, P. Yeh, and P. Beckwith, Opt. Lett. **13**, 500 (1988).
[19] S. Sinha, S. Sasikumar, A. K. Ray, and K. Dasgupta, Appl. Phys. B: Lasers Opt. **87**, 145 (2007).
[20] Z. Deng, D. Qing, P. Hemmer, C. H. Raymond Ooi, M. S. Zubairy, and M. O. Scully, Phys. Rev. Lett. **96**, 023602 (2006).

Nonlinear optical properties of graphene oxide in nanosecond and picosecond regimes

Zhibo Liu,[1] Yan Wang,[2] Xiaoliang Zhang,[1] Yanfei Xu,[2] Yongsheng Chen,[2,a] and Jianguo Tian[1,b]

[1]*Key Laboratory of Weak Light Nonlinear Photonics, Ministry of Education, and Teda Applied Physics School, Nankai University, Tianjin 300071, People's Republic of China*
[2]*Key Laboratory for Functional Polymer Materials and Centre for Nanoscale Science and Technology, and Institute of Polymer Chemistry, College of Chemistry, Nankai University, Tianjin 300071, People's Republic of China*

The nonlinear optical properties of graphene oxide (GO) were investigated at 532 nm in nanosecond and picosecond regimes. Results show that two-photon absorption dominates nonlinear absorption process of GO in the case of picosecond pulses, while excited state nonlinearities play an important role in the case of nanosecond pulses. Additionally, we compared nonlinear optical properties of three different dimensional carbon-based materials (two-dimensional graphene, one-dimensional carbon nanotube, and zero-dimensional fullerene) in nanosecond and picosecond regimes, respectively. The nonlinear mechanism of GO is distinctly different from nonlinear scattering of carbon nanotube and excited state nonlinearity of fullerene. © 2009 American Institute of Physics. [DOI: 10.1063/1.3068498]

Carbon exists in various allotropes: three-dimensional (3D) diamond, two-dimensional (2D) graphene, one-dimensional (1D) nanotube, and zero-dimensional (0D) fullerene. Scientists are familiar with the 3D, 1D, and 0D carbon nanostructures owing to their outstanding properties and great potential applications in many fields.[1,2] Graphene, as a very recent rising star in materials science with atomically thin 2D structure consisting of sp^2-hybridized carbon, exhibits remarkable electronic and mechanical properties.[3–6] Theoretically, the molecules of other carbon allotropic forms can be built from graphene. For example, 1D carbon nanotubes (CNTs) can be built by rolling up graphene with different layers and 0D fullerenes can be built by wrapping up from a single layer of graphene. It is known that perfect graphene itself does not exist and the solubility and/or processability come as the first issue for many perspective applications of graphene-based materials. So far, chemical functionalization of graphene has been focusing on improving its solubility/processability in both water and organic solvents[7,8] using different soluble groups. The presence of oxygen-containing groups in graphene oxide (GO) makes it strongly hydrophilic and water soluble.[8]

Both 1D CNT and 0D fullerene have been reported to have good optical nonlinear properties.[9–12] Single-walled CNTs (SWCNTs) and multiwalled CNT suspensions have been reported to have strong optical limiting effects in nanosecond regime.[12–14] However, fullerenes have large excited state absorption in nanosecond and picosecond regimes, which is a different nonlinear absorption (NLA) mechanism from CNT.[10] It is essential for applications of materials to make clear the mechanism of nonlinear optical (NLO) properties. Due to unique and large 2D π-electron conjugation systems of graphene, much like that in fullerene and CNTs, we expect that GO would exhibit good NLO properties. In

this paper, we report the NLO properties of GO at 532 nm in nanosecond and picosecond regimes. Two-photon absorption dominates NLA process of GO in the case of picosecond pulse, which is distinctly different from CNT and fullerene.

GO was prepared by the modified Hummers method.[15] Atomic force microscopy (AFM) images confirmed that GO was comprised of isolated graphitic sheets. GO sample was prepared in the solution of DMF (*N*, *N*-Dimethylformamide). UV-visible (UV-vis) spectra were recorded on a VARIAN Cary 300 spectrophotometer using a quartz cell with a path length of 10 mm. Figure 1 shows the UV-vis absorption spectra of GO in DMF. GO shows a strong absorption band at 268 nm. The spectra are plotted in the wavelength range from 250 to 700 nm for DMF solution. Note that the bumpy plot in the short wavelength under ~270 nm is not reliable because of the strong absorption of solvent DMF and its unlikely complete compensation.[16] The inset in Fig. 1 is a typical tapping mode AFM image of GO sheets deposited on
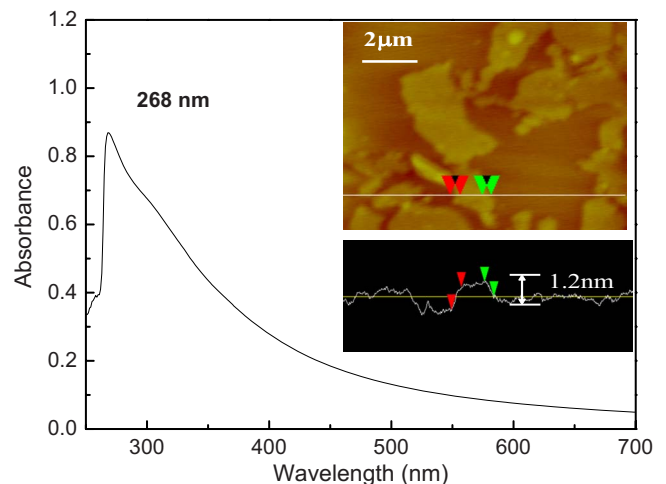
FIG. 1. (Color online) UV absorption of GO in DMF. The inset is an AFM image of GO sheets.

a)Electronic mail: yschen99@nankai.edu.cn.
b)Electronic mail: jjtian@nankai.edu.cn.
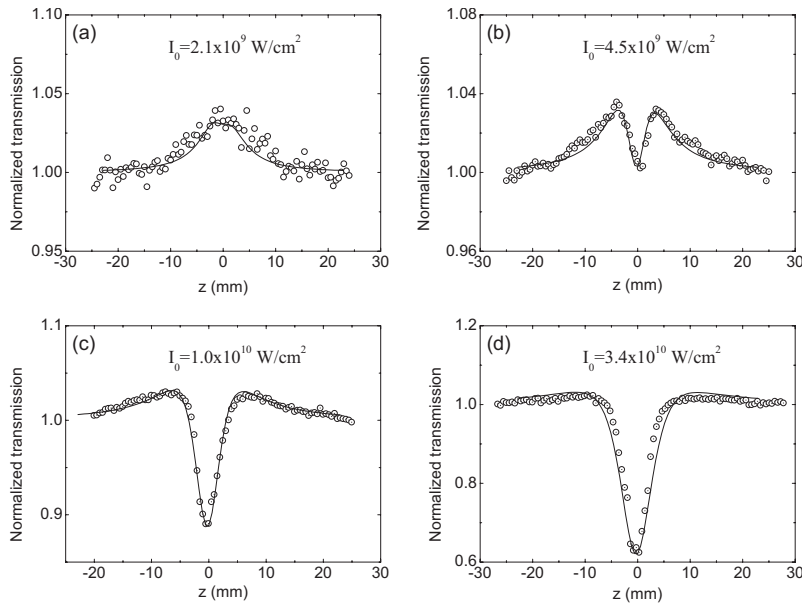
FIG. 2. Open aperture Z-scan curves of GO in DMF at different intensities. Solid lines represent theoretical fits obtained using Eqs. (1) and (2). I_0 is on-axis peak intensity at focus.

a mica substrate from a dispersion, and the height difference between arrows is ~1.2 nm, indicating an individual GO sheet. The average size of GO sheet is about 2 μm.

NLO properties of GO were measured by using Z-scan technique.[17] In Z-scan measurements, a Q-switched neodymium doped yttrium aluminum garnet (Nd:YAG) laser (Continuum Surelite-II) and a mode-locked Nd:YAG laser (Continuum model PY61) were used to generate 5 ns pulses and 35 ps pulses at 532 nm. The sample was filled in a 1-mm length quartz cell. The beam waist radius is about 20 μm. C_{60} was employed as a standard. No scattering signal was observed in the process of Z-scan measurements. Figure 2 gives open aperture picosecond Z-scan results of GO in DMF with concentration of 0.5 mg/ml at the input intensities of 2.1, 4.5, 10, and 34×10^9 W/cm^2, respectively. At the lowest input intensity of 2.1×10^9 W/cm^2, the normalized transmission curve in Fig. 2(a) shows a symmetrical peak with respect to the focus ($z=0$), indicating that saturable absorption (SA) in the sample dominates NLA mechanism. Remarkably, by increasing the input intensities to 4.5, 10, and 34×10^9 W/cm^2, as shown in Figs. 2(b)–2(d), a valley within the peak appears at the focus and becomes deeper increasingly, which implies that reverse saturable absorption (RSA) or two-photon absorption (TPA) appears following SA and finally a NLA transition occurs in GO.

Both SA and RSA originate from excited state absorption (ESA) process. When the absorption cross section of the excited state is smaller than that of the ground state, the transmission of the system will be increased when the system is highly excited. This process is called SA. ESA and TPA are the important processes leading to NLA behavior in organic materials. Under resonant and near resonant excitations, ESA is the dominant mechanism, whereas under nonresonant excitation TPA dominates the NLA behavior.[18] Under certain excitation conditions, both ESA and TPA may be operative simultaneously to lead to higher nonlinearities. From the abovementioned results, we can see two composite NLAs with opposite signs in the graphene solution at 532 nm. To interpret the flip of SA around the beam waist, we combine a SA coefficient and the TPA coefficient to yield the total absorption coefficient as[19]

$$\alpha(I) = \alpha_0 \frac{1}{1 + I/I_S} + \beta I, \tag{1}$$

where the first term describes SA and the second term describes positive NLA such as TPA. α_0 is the linear absorption coefficient, which is 789 m^{-1} for the graphene solution at 532 nm. I and I_S are laser radiation intensity and saturation intensity, respectively. β is TPA coefficient.

We theoretically fitted experimental results by solving the propagation equation of electric field envelope E:

$$\frac{1}{r}\frac{\partial}{\partial r}\left(r\frac{\partial E}{\partial r}\right) - 2ik\frac{\partial E}{\partial z} - ik\alpha E + \frac{2k^2}{n_0}n_2|E^2|E = 0, \tag{2}$$

where n_2 is nonlinear refractive index and k is wave vector. The numerical simulation of Eq. (2) was made by the Crank–Nicholson finite difference method. The best fit is obtained by using $I_s = 2.1 \times 10^9$ W/cm^2 and $\beta = 2.2 \times 10^{-9}$ cm/W. Theoretical simulations are in good agreement with the experimental results. This illustrates that the model we used is reasonable. The closed aperture Z-scan experiments showed that no obvious nonlinear refractive was observed.

In nanosecond regime, the origination of NLA will become more complicated due to participation of more excited state transitions.[20] Therefore, ESA will play a more important role in the case of nanosecond pulses. From nanosecond open aperture Z-scan results, we can see that TPA coefficient β changes as input intensity increases and $I_S = 1.2 \times 10^8$ W/cm^2 was obtained. The value of β is larger about one order of magnitude than that in picosecond regime, respectively, which indicates that NLA of GO is enhanced greatly because of the contribution of ESA in nanosecond regime. To illustrate the difference in mechanism of NLA in nanosecond and picosecond regimes, we give NLA coefficient β as a function of input intensities for two different pulse widths in Figs. 3(a) and 3(b). With the increasing in input intensity, the value of β keeps almost the constant of 2.2×10^{-9} cm/W for picosecond pulses [Fig. 3(b)], while a clear enhancement of β can be observed from 2.9 to 5.6 $\times 10^{-8}$ cm/W for nanosecond pulses [Fig. 3(a)]. The change
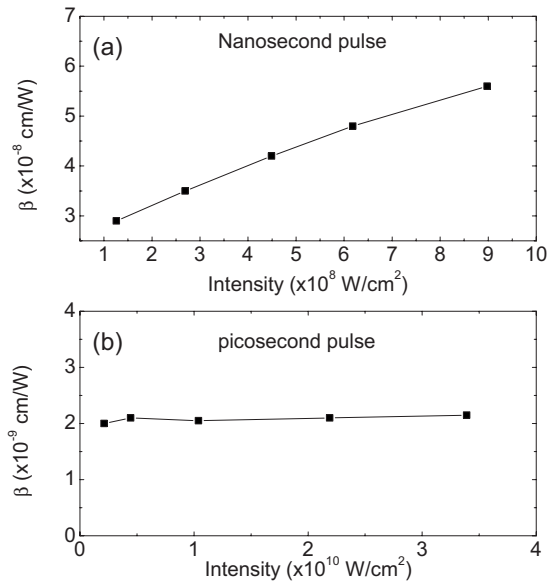
FIG. 3. NLA coefficient β as a function of input intensities for nanosecond and picosecond pulses.

in β with input intensity indicates that beside TPA, the contribution of ESA to NLA behavior of GO is also important in nanosecond regime.[20]

From the results mentioned above, GO in the DMF solution exhibits large TPA in picosecond regime and ESA in nanosecond regime. As the molecules of other carbon allotropic forms, fullerene and CNT have a different NLA process from graphene.[9,12] Although the mechanisms of NLA are different for these three carbon allotropic forms, to compare their optical nonlinearities qualitatively, we performed open aperture Z-scan measurements of GO, SWCNT in DMF, and C_{60} in toluene with same linear transmittance of 70% using picosecond and nanosecond pulses, as shown in Fig. 4. Since C_{60} has large singlet and triplet excited states
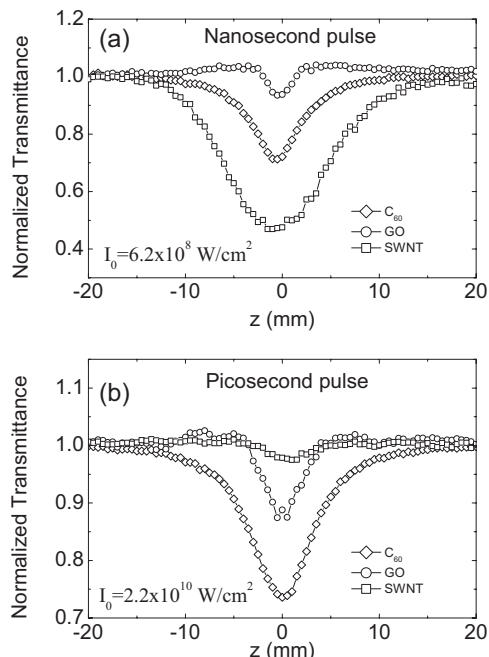
FIG. 4. Open aperture Z-scan curves of GO, SWCNT in DMF, and C_{60} in toluene for nanosecond pulses (a) and picosecond pulses (b).

absorption cross sections, it exhibits strong ESA for the two kinds of pulses. SWCNTs limiting action is strongest in the nanosecond time scale but is poorest in picosecond regime because strong nonlinear scattering happens in nanosecond regime. The 2D system exhibits much richer features of NLO response than 1D system. Therefore, the additional degrees of freedom associated with the 2D system may allow a finer modulation of the NLO response.[21]

In summary, we studied the NLA of GO in DMF using picosecond and nanosecond pulses. TPA and ESA were observed in picosecond and nanosecond regimes, respectively, and large TPA coefficient β was obtained. We compared the optical nonlinearities of three carbon nanomaterials, 0D fullerene, 1D CNT, and 2D graphene. Because graphene is lower cost and has different NLA mechanism from fullerene and CNT, we expect that graphene may bring a competitive entry into the realm of NLO materials for optoelectronic devices.

[1]P. M. Ajayan, Chem. Rev. (Washington, D.C.) **99**, 1787 (1999).
[2]N. Martin, L. Sanchez, B. Illescas, and I. Perez, Chem. Rev. (Washington, D.C.) **98**, 2527 (1998).
[3]D. Li and R. B. Kaner, Science **320**, 1170 (2008).
[4]D. A. Dikin, S. Stankovich, E. J. Zimney, R. D. Piner, G. H. B. Dommett, G. Evmenenko, S. T. Nguyen, and R. S. Ruoff, Nature (London) **448**, 457 (2007).
[5]J. S. Bunch, A. M. van der Zande, S. S. Verbridge, I. W. Frank, D. M. Tanenbaum, J. M. Parpia, H. G. Craighead, and P. L. Mceuen, Science **315**, 490 (2007).
[6]A. K. Geim and K. S. Novoselov, Nature Mater. **6**, 183 (2007).
[7]S. Niyogi, E. Bekyarova, M. E. Itkis, J. L. McWilliams, M. A. Hamon, and R. C. Haddon, J. Am. Chem. Soc. **128**, 7720 (2006).
[8]S. Stankovich, D. A. Dikin, G. H. B. Dommett, K. M. Kohlhaas, E. J. Zimney, E. A. Stach, R. D. Piner, S. T. Nguyen, and R. S. Ruoff, Nature (London) **442**, 282 (2006).
[9]L. W. Tutt and A. Kost, Nature (London) **356**, 225 (1992).
[10]D. G. McLean, R. L. Sutherland, M. C. Brant, D. M. Brandelik, P. A. Fleitz, and T. Pottenger, Opt. Lett. **18**, 858 (1993).
[11]Z. B. Liu, J. G. Tian, Z. Guo, D. M. Ren, F. Du, J. Y. Zheng, and Y. S. Chen, Adv. Mater. (Weinheim, Ger.) **20**, 511 (2008).
[12]L. Vivien, D. Riehl, F. Hache, and E. Anglaret, Physica B **323**, 233 (2002).
[13]P. Chen, X. Wu, X. Sun, J. Lin, W. Ji, and K. L. Tan, Phys. Rev. Lett. **82**, 2548 (1999).
[14]X. Sun, R. Q. Yu, G. Q. Xu, T. S. A. Hor, and W. Ji, Appl. Phys. Lett. **73**, 3632 (1998).
[15]H. A. Becerril, J. Mao, Z. F. Liu, R. M. Stoltenberg, Z. N. Bao, and Y. S. Chen, ACS Nano **2**, 463 (2008).
[16]J. I. Paredes, S. Villar-Rodil, A. Martinez-Alonso, and J. M. D. Tascon, Langmuir **24**, 10560 (2008).
[17]M. Sheikbahae, A. A. Said, T. H. Wei, D. J. Hagan, and E. W. Vanstryland, IEEE J. Quantum Electron. **26**, 760 (1990).
[18]P. P. Kiran, D. R. Reddy, A. K. Dharmadhikari, B. G. Maiya, G. R. Kumar, and D. N. Rao, Chem. Phys. Lett. **418**, 442 (2006).
[19]Y. Gao, X. Zhang, Y. Li, H. Liu, Y. Wang, Q. Chang, W. Jiao, and Y. Song, Opt. Commun. **251**, 429 (2005).
[20]R. L. Sutherland, *Handbook of Nonlinear Optics*, 2nd ed. (Dekker, New York, 2003).
[21]G. de la Torre, P. Vaquez, F. Agulló-Lopez, and T. Torres, Chem. Rev. (Washington, D.C.) **104**, 3723 (2004).

A Graphene Hybrid Material Covalently Functionalized with Porphyrin: Synthesis and Optical Limiting Property

By *Yanfei Xu, Zhibo Liu, Xiaoliang Zhang, Yan Wang, Jianguo Tian,* Yi Huang, Yanfeng Ma, Xiaoyan Zhang,* and *Yongsheng Chen**

Graphene, a very recent rising star in material science, with an atomically thin, 2D structure that consists of sp²-hybridized carbons, exhibits remarkable electronic and mechanical properties.[1–4] Theoretically, the molecules of other allotropic carbon forms can be built from graphene. For example, 1D carbon nanotubes (CNTs) can be built by rolling up graphene with different layers, and 0D fullerenes can be built by wrapping up a single layer of graphene. Graphene (or '2D graphite') is widely used to describe the properties of various carbon-based materials. With the numerous reports of the many exceptional properties and applications of carbon nanotubes[5] and fullerenes,[6] the intensive research of graphene and its use in many nanoelectronic and optoelectronic devices, and as a nanometer-scale building block for new nanomaterials, is expected. So far, different device applications, such as field-effect transistors,[7] resonators,[3] transparent anodes,[8] and organic photovoltaic devices have been reported.[9] It is known that perfect graphene itself does not exist, and the solubility and/or processability are the first issues for many perspective applications of graphene-based materials. So far, chemical functionalization of graphene has focused on improving its solubility/processability in both water and organic solvents using different soluble groups.[10–14] However, multifunctional hybrid materials that take advantage of both the superior properties of graphene and a functionalizing material have been largely unexplored.

The presence of oxygen-containing groups in graphene oxide renders it strongly hydrophilic and water soluble,[12] and also provides a handle for the chemical modification of graphene using known carbon surface chemistry. Porphyrins are 'the pigments of life',[15] with a large extinction coefficient in the visible-light region, predictable rigid structures, and prospective photochemical electron-transfer ability.[16] The extensive 2D 18 π-electron porphyrins and porphyrin-modified acceptor nanoparticles exhibit good optoelectronic properties.[17–22] Therefore, it is expected that, by combining 2D nanometer-scale graphene

with optoelectronically active porphyrin moelecules, multifunctional nanometer-scale materials for optical and/or optoelectronic applications may be generated. In this paper, we report the first organic-solution-processable functionalized-graphene (SPFGraphene) hybrid material with porphyrins, and its photophysical properties including optical-limiting properties.

The synthesis of the porphyrin–graphene nanohybrid, 5-4 (aminophenyl)-10, 15, 20-triphenyl porphyrin (TPP) and graphene oxide molecules covalently bonded together via an amide bond (TPP-NHCO-SPFGraphene, Scheme 1 and 2) was carried out using an amine-functionalized prophyrin (TPP-NH₂) and graphene oxide in *N,N*-dimethylformamide (DMF), following standard chemistry. Large-scale and water-soluble graphene oxide was prepared by the modified Hummers method.[8,9,23] Results of atomic force microscopy (AFM, see Supporting Information, Fig. S1), thermogravimetry analysis (TGA), and X-ray diffraction (XRD) characterization have confirmed that this graphene material can be easily dispersed at the state of complete exfoliation, which consists of almost entire single-layered graphene sheets in H₂O.[8,9] TPP-NH₂ and graphene oxide molecules are covalently bonded together by an amide bond. Much care has been taken to make sure all the unreacted TPP-NH₂ has been removed using extensive solvent washing, sonication, and membrane filtration. Details are given in the Experimental part. The attachment of organic molecules to graphene oxide has made TPP-NHCO- SPFGraphene soluble in DMF and other polar solvents.

Figure 1 shows FTIR spectra of TPP-NHCO-SPFGraphene, TPP-NH₂, and graphene oxide. In the spectrum of graphene oxide, the peak at 1730 cm⁻¹ is characteristic of the C=O stretch of the carboxylic group on the graphene oxide. In the spectrum

[*] Prof. J. Tian, Dr. Z. Liu, X. L. Zhang
Key Laboratory of Weak Light Non-linear Photonics
Ministry of Education and Teda Applied Physics School
Nankai University, Tianjin 300457 (P.R. China)
E-mail: jjtian@nankai.edu.cn
Prof. Y. Chen, Y. Xu, X. Zhang, Y. Wang, Prof. Y. Huang, Prof. Y. Ma
Key Laboratory for Functional Polymer Materials
and Centre for Nanoscale Science and Technology
Institute of Polymer Chemistry
College of Chemistry
Nankai University, Tianjin 300071 (P.R. China)
E-mail: yschen99@nankai.edu.cn

Scheme 1. Synthesis scheme of TPP-NHCO-SPFGraphene.

COMMUNICATION

Scheme 2. Schematic representation of part of the structure of the covalent TPP-NHCO-SPFGraphene.

blended sample of graphene oxide with TPP-NH$_2$ (as a control sample) in DMF. Graphene oxide shows a strong absorption band at 268 nm. The TPP-NH$_2$ spectrum exhibits a strong Soret absorption at 419 nm, and weak Q-bands between 500 and 700 nm, which are consistent with that of TPP-NH$_2$ analogues.[24] The control sample exhibits a broad absorption at 274 nm, while the hybrid TPP-NHCO- SPFGraphene exhibits a broad absorption at 280 nm, which should be the corresponding graphene oxide peak at 268 nm with a red-shift of 12 nm. A similar band is also observed for TPP-NHCO-SPFGraphene and the control sample at 419 nm, which corresponds to the Soret band of the TPP-NH$_2$ moiety, and no obvious shift is observed for either samples. These results indicate that in the ground state attachment of the TPP-NH$_2$ moiety has perturbed the electronic state of the graphene oxide, but no significant effect is observed on the TPP-NH$_2$ part.

The prevention of aggregation is of particular importance for graphene processability and applications, because most of their attractive properties are only associated with individual graphene sheets. Solution-phase UV-vis-NIR spectroscopy has been reported to demonstrate a linear relationship between the absorbance and the relative concentrations of single-walled carbon nanotubes (SWNTs) in different solvents, which obey Beer's law at low concentrations, and has been used to determine the solubility of SWNTs.[25] Figure 3 shows the absorption spectra of solutions of TPP-NHCO-SPFGraphene with different concentrations. The absorption values at 419 nm were plotted against concentration to generate a standard curve (in mg L^{-1}, Fig. 3 and the inset Fig. 3A). On the basis of the applicability of Beer's law,

of TPP-NHCO-SPFGraphene, the peak at 1730 cm^{-1} almost disappears, and a new broad band emerges at 1640 cm^{-1}, which corresponds to the C=O characteristic stretching band of the amide group.[10] The stretching band of the amide C–N peak appears at 1260 cm^{-1}. These results clearly indicate that the TPP-NH$_2$ molecules had been covalently bonded to the graphene oxide by the amide linkage. Transmission electron microscopy (TEM) was used to further characterize the TPP-NHCO-SPFGraphene (see Supporting Information, Fig. S2).

Figure 2 shows UV-vis absorption spectra of TPP-NHCO-SPFGraphene, TPP-NH$_2$, graphene oxide, and a physically

Figure 1. FTIR spectra of TPP-NHCO-SPFGraphene, TPP-NH$_2$, and graphene oxide. A band emerges at 1640 cm^{-1} that corresponds to the C=O stretch of the amide group, indicating that the TPP-NH$_2$ molecules have been covalently bonded to the graphene oxide by an amide linkage.
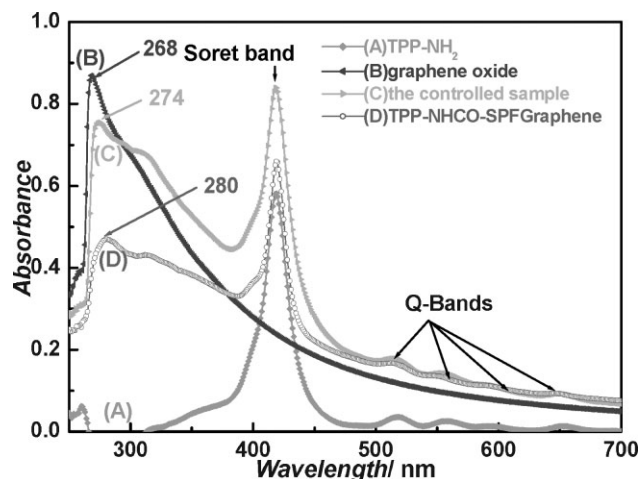
Figure 2. UV absorption of TPP-NHCO-SPFGraphene, TPP-NH$_2$, graphene oxide, and the control sample in DMF. Concentrations: TPP-NHCO-SPFGraphene, 27 mg L^{-1}; graphene oxide, 30 mg L^{-1}; the control sample (graphene oxide 31 mg L^{-1}, TPP-NH$_2$ 1.4 mg L^{-1}); TPP-NH$_2$, 1.4 mg L^{-1}. (Different concentrations with a maximum absorption of 0.3–0.9 were used for a better comparison.)
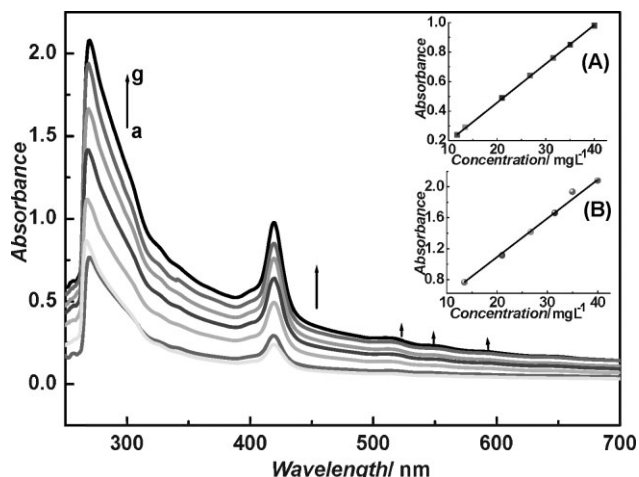
Figure 3. Concentration dependence of the UV absorption of TPP-NHCO-SPFGraphene in DMF (concentrations are 40, 35, 32, 27, 21, 14, and 12 mg L^{-1}, from a to g, respectively). The the plot of optical density at 419 nm versus concentration is shown in inset A) is, and inset B) is the plot of the absorption of the graphene moiety versus concentration. The straight line is a linear least-squares fit to the data, which indicates that the hybrid TPP-NHCO-SPFGraphene is homogeneously dissolved in the solvent.

we estimated the effective extinction coefficient of the TPP-NHCO-SPFGraphene from the slope of the linear least-squares fit to be 0.024 L mg^{-1} cm^{-1}, with an R value of 0.992. The absorbance of solutions of TPP-NHCO-SPFGraphene at other wavelengths was also in line with Beer's law. For example, the inset B) in Figure 3 shows that a linear relationship exists between the absorption and the concentrations measured at the maximal absorption position for the graphene moiety in the hybrid. These results demonstrate that the hybrid was homogeneously dispersed in DMF.

In order to probe the excited-state interactions of TPP-NH$_2$ and graphene in the hybrid, fluorescence spectra of TPP-NH$_2$, the control sample, and TPP-NHCO-SPFGraphene are compared in
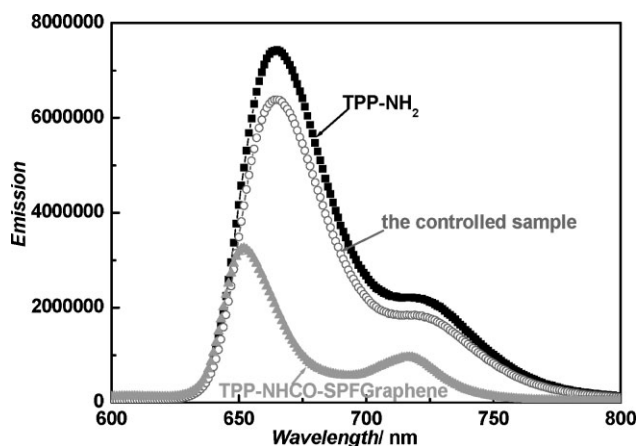
Figure 4. Fluorescence spectroscopic changes observed for TPP-NH$_2$, the control sample, and TPP-NHCO-SPFGraphene in DMF, with the normalization of the absorbance of the Soret band excitation wavelength (419 nm) to the same value (0.24).

Figure 4. Upon excitation of TPP-NH$_2$ at a Soret band of 419 nm, with the absorbance of TPP-NH$_2$, the control sample, and TPP-NHCO-SPFGraphene being the same value (0.24) at the excitation wavelength, the solution of the control sample Exhibits 14% quenching of the fluorescence emission, while a much stronger 56% quenching is observed for the hybrid TPP-NHCO-SPFGraphene. Excitation of TPP-NHCO-SPFGraphene and the control sample at other excitation wavelengths (400, 450, and 500 nm) shows a much stronger quenching (see Supporting information, Fig. S3–S5). The observed luminescence quenching indicates that there is a strong interaction between the excited state of TPP-NH$_2$ and graphene moieties in the hybrid. Possible pathways for the fluorescence quenching of the excited TPP-NH$_2$ may be attributed to two possible competitive processes: photoinduced electron transfer (PET) and energy transfer (ET). Similar luminescence quenching has been observed for the hybrids of CNTs with porphyrins, and a PET mechanism has been demonstrated for these hybrids.[26] Molecular-orbital theory and experimental results have shown that closed-cage carbon structures, such as fullerenes and carbon nanotubes, are favorable electron acceptors, because of their unique π-electron system when the two moieties are connected directly.[27] Thus, after photoexcitation, the intramolecular donor–acceptor interaction between the two moieties of TPP-NH$_2$ and graphene in our TPP-NHCO-SPFGraphene nanohybrid may have a charge transfer from the photoexcited singlet TPP-NH$_2$ to the graphene moiety, and this results in the observed fluorescence quenching and energy release. In this TPP-NHCO-SPFGraphene nanohybrid, the effective intramolecular energy quenching may also be facilitated by a through-bond mechanism, as a result of the direct linkage mode of the two moieties by the amide bond.[25]

With the efficient energy and/or electron transfer upon photoexcitation, and the reported excellent optical limiting properties of C$_{60}$, carbon nanotubes and their functionalized materials,[25,28,29] it would be both interesting and important to investigate the optical limiting properties of the TPP-NHCO-SPFGraphene. Optical limiting materials are materials that exhibit high transmittance of low-intensity light and attenuate intense optical beams.[30] They can be used to protect optical sensors, for example, eyes or charge-coupled device (CCD) cameras, from possible damage caused by intense laser pulses, and have potential applications in the field of optical switching and other areas.

Figure 5 shows open-aperture Z-scan[31] results of TPP-NHCO-SPFGraphene, TPP-NH$_2$, graphene oxide, a control blend sample of TPP-NH$_2$ with graphene oxide (1: 1 weight ratio), and C$_{60}$. The optical limiting properties of the solutions of these materials were investigated using 532 nm pulsed laser irradiation, and C$_{60}$ was employed as a standard. The details of the measurement are described in the Supporting Information. To compare the optical limiting effect, all of the sample concentrations were adjusted to have same linear transmittance of 75% at 532 nm in cells 1 mm thick.

The open-aperture Z-scan measures the transmittance of the sample as it translates through the focal plane of a tightly focused beam. As the sample is brought closer to focus, the beam intensity increases, and the nonlinear effect increases, which will lead to a decreasing transmittance for reverse saturatable absorption (RSA), two-photon absorption (TPA), and nonlinear

COMMUNICATION
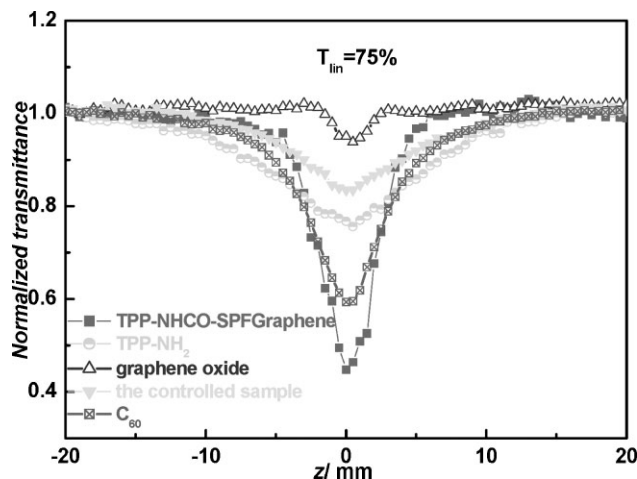
Figure 5. Open-aperture *Z*-scan results of TPP-NHCO-SPFGraphene, TPP-NH$_2$, graphene oxide, control sample, and C$_{60}$, with the same linear transmittance of 75% to 5 ns, 532 nm optical pulses.

scattering. As shown in Figure 5, the TPP-NHCO-SPFGraphene has the largest dip among the transmittance curves of the studied materials. Therefore, TPP-NHCO-SPFGraphene demonstrates much better optical limiting properties compared with the benchmark material (C$_{60}$), the control sample, and the individual components (TPP-NH$_2$ and graphene oxide) of the hybrid. Porphyrins are well known to exhibit RSA in the visible-wavelength range,[28] while graphene oxide has a TPA at 532 nm, which is used in our experiments because the linear absorption peak of graphene oxide is located at 268 nm. Considering the covalent donor–acceptor structure, and the efficient fluorescence quenching of this nanohybrid, we believe that the photoinduced electron and/or energy transfer from the electron donor TPP-NH$_2$ to the acceptor graphene should play an important role for the much-enhanced optical limiting performance.[29] Furthermore, during the *Z*-scan experiments, as shown in Figure 5, enhanced scattering could also be observed for the sample of TPP-NHCO-SPFGraphene moving towards the focus of the laser. This implies that the observed *Z*-scan curve is also influenced by nonlinear scattering. Therefore, the much-enhanced optical limiting performance of TPP-NHCO-SPFGraphene should arise from a combination of photoinduced electron and/or energy transfer, RSA, TPA, and nonlinear scattering mechanisms. Similar results have been observed for the hybrid materials of carbon nanotubes with porphyrins.[25,32]

In summary, we have reported the first covalently bonded and organic soluble graphene (SPFGraphene) hybrid with porphyrin. FTIR, UV-vis absorption, and TEM studies confirm the covalent functionalization of the graphene. Attachment of TPP-NH$_2$ significantly improves the solubility and dispersion stability of the graphene-based material in organic solvents. In this donor–acceptor nanohybrid, the fluorescence of photoexcited TPP-NH$_2$ is effectively quenched by a possible electron-transfer process. A superior optical limiting effect, better than the benchmark optical limiting material C$_{60}$ and the control sample, is observed. Photoinduced electron- and/or energy-transfer mechanisms play a significant role in the superior optical limiting performance. With the abundant and highly pure functionalized graphene

material readily available, its unique structure, and excellent electronic properties, we expect this organic solution-processable functionalized graphene material to be a competitive entry in the realm of light harvesting and solar-energy conversion materials for optoelectronic devices.

Experimental

Synthesis of TPP-NHCO-SPFGraphene: The synthesis of TPP-NHCO-SPFGraphene is shown in Scheme 1. TPP-NH$_2$ was synthesized according to the literature [33]. Graphene oxide (30 mg) was prepared using our modified Hummers method [8,9,23], and it was then refluxed in SOCl$_2$ (20 mL) in the presence of DMF (0.5 mL) at 70 °C for 24 h under argon atmosphere. At the end of the reaction, excess SOCl$_2$ and solvent were removed by distillation. In the presence of triethylamine (Et$_3$N, 0.5 mL), the above product was allowed to react with TPP-NH$_2$ (30 mg) in DMF (10 mL) at 130 °C for 72 h under argon. After the reaction, the solution was cooled to room temperature, and then poured into ether (300 mL) to precipitate the product. The product was isolated by filtration on a Nylon membrane (0.22 µm). The excess TPP-NH$_2$ and other impurities were removed through five washing cycles, which included sonication, filtration (discarding the filtrate), and re-suspension of the solid in tetrahydrofuran (50 mL). The precipitate was washed with CHCl$_3$ five times, following the above procedure. UV spectroscopy and thin-layer chromatography (TLC) were used to check the filtrate to ensure no TPP-NH$_2$ existed in the final washing. The TPP-NHCO-SPFGraphene was then washed with a small quantity of H$_2$O to remove Et$_3$N · HCl, and finally dried under vacuum to yield the hybrid TPP-NHCO-SPFGraphene.

Acknowledgements

[1] D. Li, R. B. Kaner, *Science* **2008**, *320*, 1170.

[2] D. A. Dikin, S. Stankovich, E. J. Zimney, R. D. Piner, G. H. B. Dommett, G. Evmenenko, S. T. Nguyen, R. S. Ruoff, *Nature* **2007**, *448*, 457.

[3] J. S. Bunch, A. M. van der Zande, S. S. Verbridge, I. W. Frank, D. M. Tanenbaum, J. M. Parpia, H. G. Craighead, P. L. Mceuen, *Science* **2007**, *315*, 490.

[4] A. K. Geim, K. S. Novoselov, *Nat. Mater.* **2007**, *6*, 183.

[5] P. M. Ajayan, *Chem. Rev.* **1999**, *99*, 1787.

[6] N. Martin, L. Sanchez, B. Illescas, I. Perez, *Chem. Rev.* **1998**, *98*, 2527.

[7] K. S. Novoselov, A. K. Geim, S. V. Morozov, D. Y. Jiang, Zhang, S. V. Dubonos, I. V. Grigorieva, A. A. Firsov, *Science* **2004**, *306*, 666.

[8] H. A. Becerril, J. Mao, Z. F. Liu, R. M. Stoltenberg, Z. N. Bao, Y. S. Chen, *ACS Nano* **2008**, *2*, 463.

[9] Z. F. Liu, Q. Liu, X. Y. Zhang, Y. Huang, Y. F. Ma, S. G. Yin, Y. S. Chen, *Adv. Mater.* **2008**, *20*, 3924.

[10] S. Niyogi, E. Bekyarova, M. E. Itkis, J. L. McWilliams, M. A. Hamon, R. C. Haddon, *J. Am. Chem. Soc.* **2006**, *128*, 7720.

[11] Y. X. Xu, H. Bai, G. W. Lu, C. Li, G. Q. Shi, *J. Am. Chem. Soc.* **2008**, *130*, 5856.

[12] S. Stankovich, D. A. Dikin, G. H. B. Dommett, K. M. Kohlhaas, E. J. Zimney, E. A. Stach, R. D. Piner, S. T. Nguyen, R. S. Ruoff, *Nature* **2006**, *442*, 282.

[13] S. Stankovich, R. D. Piner, S. T. Nguyen, R. S. Ruoff, *Carbon* **2006**, *44*, 3342.

[14] Y. C. Si, E. T. Samulski, *Nano Lett.* **2008**, *8*, 1679.

[15] A. Rieder, B. Krautler, *J. Am. Chem. Soc.* **2000**, *122*, 9050.

[16] D. M. Guldi, M. Prato, *Acc. Chem. Res.* **2000**, *33*, 695.

[17] A. Baev, O. Rubio-Pons, F. Gel'mukhanov, H. Agren, *J. Phys. Chem. A* **2004**, *108*, 7406.

[18] M. O. Liu, C. H. Tai, W. Y. Wang, J. R. Chen, A. T. Hu, T. H. Wei, *J. Organomet. Chem.* **2004**, *689*, 1078.

[19] R. B. Martin, H. P. Li, L. R. Gu, S. Kumar, C. M. Sanders, Y. P. Sun, *Opt. Mater.* **2005**, *27*, 1340.

[20] M. Calvete, G. Y. Yang, M. Hanack, *Synth. Met.* **2004**, *141*, 231.

[21] P. P. Kiran, D. R. Reddy, B. G. Maiya, A. K. Dharmadhikari, G. R. Kumar, D. N. Rao, *Opt. Commun.* **2005**, *252*, 150.

[22] K. Sendhil, C. Vijayan, M. P. Kothiyal, *Opt. Mater.* **2005**, *27*, 1606.

[23] W. S. Hummers, Jr., R. E. Offeman, *J. Am. Chem. Soc.* **1958**, *80*, 1339.

[24] T. Umeyama, M. Fujita, N. Tezuka, N. Kadota, Y. Matano, K. Yoshida, S. Isoda, H. Imahori, *J. Phys. Chem. C* **2007**, *111*, 11484.

[25] Z. Guo, F. Du, D. M. Ren, Y. S. Chen, J. Y. Zheng, Z. B. Liu, J. G. Tian, *J. Mater. Chem.* **2006**, *16*, 3021.

[26] D. Baskaran, J. W. Mays, X. P. Zhang, M. S. Bratcher, *J. Am. Chem. Soc.* **2005**, *127*, 6916.

[27] P. W. Fowler, A. Ceulemans, *J. Phys. Chem.* **1995**, *99*, 508.

[28] M. O. Senge, M. Fazekas, E. G. A. Notaras, W. J. Blau, M. Zawadzka, O. B. Locos, E. M. N. Mhuircheartaigh, *Adv. Mater.* **2007**, *19*, 2737.

[29] W. Wu, S. Zhang, Y. Li, J. X. Li, L. Q. Liu, Y. J. Qin, Z. X. Guo, L. M. Dai, C. Ye, D. B. Zhu, *Macromolecules* **2003**, *36*, 6286.

[30] S. A. O'Flaherty, R. Murphy, S. V. Hold, M. Cadek, J. N. Coleman, W. J. Blau, *J. Phys. Chem. B* **2003**, *107*, 958.

[31] M. Sheikbahae, A. A. Said, T. H. Wei, D. J. Hagan, E. W. Vanstryland, *IEEE J. Quantum Electron.* **1990**, *26*, 760.

[32] Z. B. Liu, J. G. Tian, Z. Guo, D. M. Ren, F. Du, J. Y. Zheng, Y. S. Chen, *Adv. Mater.* **2008**, *20*, 511.

[33] W. J. Kruper, T. A. Chamberlin, M. Kochanny, *J. Org. Chem.* **1989**, *54*, 2753.

WILEY
InterScience®
DISCOVER SOMETHING GREAT

NANO LETTERS

Letter

Efficient Generation of Propagating Plasmons by Electron Beams

Wei Cai, Rebecca Sainidou, Jingjun Xu, A. Polman, and F. Javier Garci#a de Abajo
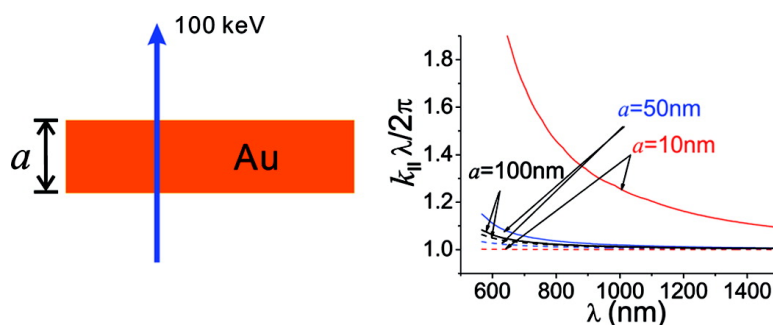
More About This Article

Additional resources and features associated with this article are available within the HTML version:

- Supporting Information
- Access to high resolution figures
- Links to articles and content related to this article
- Copyright permission to reproduce figures and/or text from this article

View the Full Text HTML

Efficient Generation of Propagating Plasmons by Electron Beams

Wei Cai,[†,‡] Rebecca Sainidou,[†,§] Jingjun Xu,[‡] A. Polman,[‖] and F. Javier García de Abajo*,[†]

Instituto de Óptica—CSIC, Serrano 121, 28006 Madrid, Spain, The Key Laboratory of Weak-Light Nonlinear Photonics, Ministry of Education and TEDA Applied Physics School, Nankai University, Tianjin 300457, China, Laboratoire d'Ondes et Milieux Complexes FRE CNRS 3102, Université du Havre, Place R. Schuman, 76610 Le Havre, France, and Center for Nanophotonics, FOM Institute AMOLF, Kruislaan 407, 1098 SJ Amsterdam, The Netherlands

ABSTRACT

We report highly efficient generation of propagating plasmons by electron beams in planar films, planar dielectric cavities, metallic wires, and nanoparticle waveguides. Electron-induced plasmon excitation is investigated in (1) gold thin films, both free-standing or supported on a silica substrate, (2) gold—silica—gold planar cavities, (3) gold nanowires, and (4) gold nanoparticle arrays. We obtain excitation yields as high as 10^{-2} plasmons per incoming electron over the visible and near-infrared range. Symmetric and antisymmetric plasmon modes are found to be more easily excited in thick and thin films, respectively, and in particular leaky plasmons in supported films are shown to be excited with very large probability exceeding one plasmon per electron. Generation of guided plasmons in metallic particle arrays is also proved to be attainable by aiming the electron at one end of the waveguide. The temporal evolution and spectral distribution of excited plasmons are discussed as well. Our results provide full support for the application of electron bombardment to excite propagating plasmons with high efficiency, thus solving the standing problem of plasmon generation at designated locations.

Propagating plasmons are becoming an essential ingredient in the design of optical devices at nanometer scales, in which the long propagation distances characterizing these excitations are combined with large confinement in the direction perpendicular to the metal surface.[1,2] Plasmon waveguiding has been experimentally demonstrated in a variety of systems, including planar metal films,[3–5] grooves patterned in metal surfaces,[6] surface-plasmon polariton (SPP) crystals,[7] and coupled nanoparticle arrays.[8,9] SPPs are actually a subject of increasing activity, with exciting results such as new designs capable of improving the compromise between propagation distances and lateral confinement, particularly in metallic wedges,[10] closely spaced wires,[11] and metallo-dielectric hybrid structures.[12]

The generation of SPPs at designated positions in a customizable fashion remains a standing problem in plasmonics. Recent studies have suggested that fast electrons provide a good solution to this problem by aiming an electron beam at the desired position on a metal surface, thus

generating SPPs.[13–15] The generation of these plasmons has been monitored through the cathodoluminescence (CL) emission that they produce when SPPs are decoupled from the metal by a grating. Pioneering research on the use of CL to retrieve surface plasmon dispersion relations can be traced back to Ritchie *et al.*[16] and Heitmann,[17] followed by successful SPP dispersion mapping obtained from energy-loss and deflection-angle distributions of fast electrons traversing thin films.[18,19] More recently, the interference between directly generated light (transition radiation)[20,21] and SPPs outcoupled by a grating has been used to measure the SPP excitation yield in a planar surface.[22] Incidentally, CL has been employed to obtain snapshots of plasmons confined in metallic nanoparticles,[23–27] as well as standing waves of propagating plasmons in finite SPP resonant cavities,[28,29] while electron energy-loss spectroscopy (EELS) performed in thin samples can also reveal plasmon mode patterns with nanometer spatial resolution.[30,31]

In this paper, we discuss the generation of propagating plasmons in various systems, including free-standing and supported metallic thin films, metal—insulator—metal waveguides, metallic wires, and particle arrays. The plasmon excitation probability is calculated analytically for planar interfaces and using numerical methods for more complicated systems (nanowires and particle arrays). We quantitatively assess the plasmon

* Corresponding author, jga@cfmac.csic.es.
† Instituto de Óptica—CSIC.
‡ The Key Laboratory of Weak-Light Nonlinear Photonics, Ministry of Education and TEDA Applied Physics School, Nankai University.
§ Laboratoire d'Ondes et Milieux Complexes FRE CNRS 3102, Université du Havre.
‖ Center for Nanophotonics, FOM Institute AMOLF.
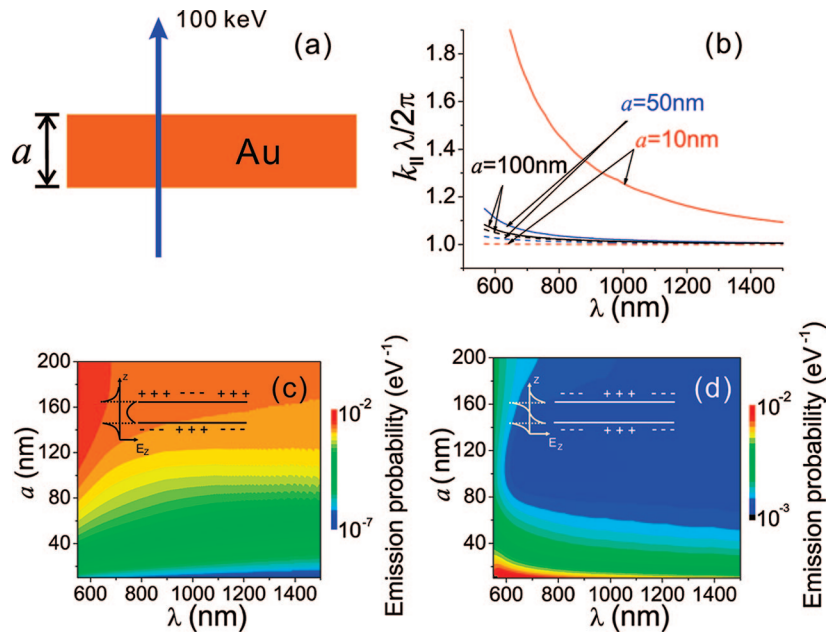
Figure 1. Plasmon generation in metallic thin films by an electron beam. (a) We consider a 100 keV electron traversing a free-standing gold thin film of thickness a. (b) Gold-film plasmon dispersion curves for thicknesses $a = 10$, 50, and 100 nm: parallel wavevector $k_{\parallel}$ versus vacuum wavelength λ. Symmetric and antisymmetric plasmon modes are represented by dashed and solid curves, respectively. (c, d) Probability that an electron creates a surface plasmon as a function of film thickness and vacuum wavelength. The probability is normalized per unit of plasmon energy range and it is separately given for symmetric (c) and antisymmetric (d) plasmon modes. The schematic insets in (c) and (d) show the induced charges (+ and − signs) and the normal electric field profile of these modes. Note the different color scales in (c) and (d).
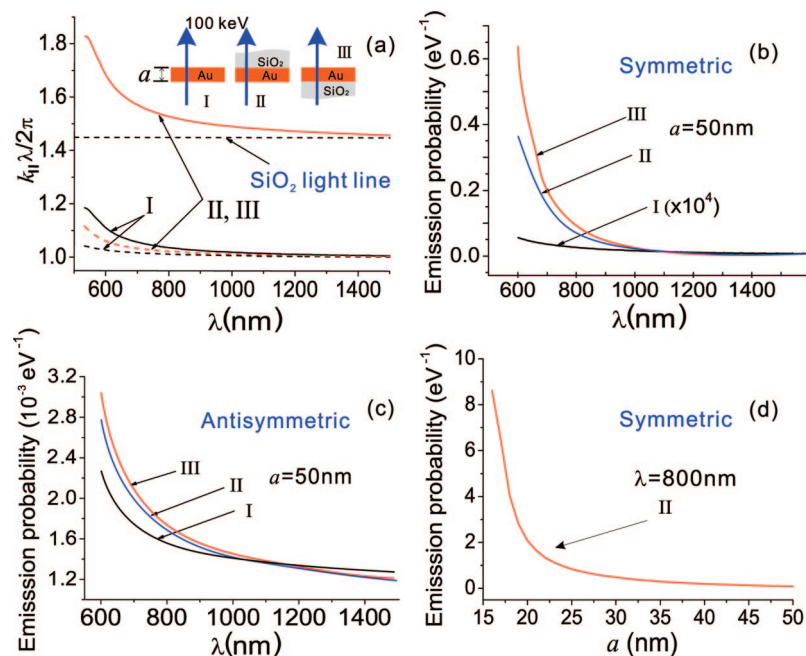
Figure 2. Plasmon generation in supported metal films. (a) Dispersion relation of plasmons in the structures I, II, and III, shown in the insets, for a gold thickness $a = 50$ nm. Symmetric and antisymmetric plasmon modes are represented by dashed and solid curves, respectively. (b, c) Probability of coupling to symmetric (b) and antisymmetric (c) plasmon modes in these structures. Note the different vertical scale in (c). The probability of curve I in (b) has been multiplied by a factor of 10^4. (d) Probability of exciting symmetric plasmon modes corresponding to a free-space wavelength of 800 nm in the structure II as a function of metal film thickness.

excitation yield in these systems and conclude that electron bombardment is a practical way of generating plasmons with high efficiency at positions controlled with nanometer precision through focused electron-beam bombardment.

We discuss first metal films and metal−insulator−metal (MIM) waveguides. Electron-beam excitation of plasmons

in these systems can be studied by considering the electric field set up by an electron crossing two parallel interfaces with constant velocity v under normal incidence. We have worked out a quasi-analytical expression for the excitation probability that we use to obtain the results presented in Figures 1−3. The actual expression and its derivation are
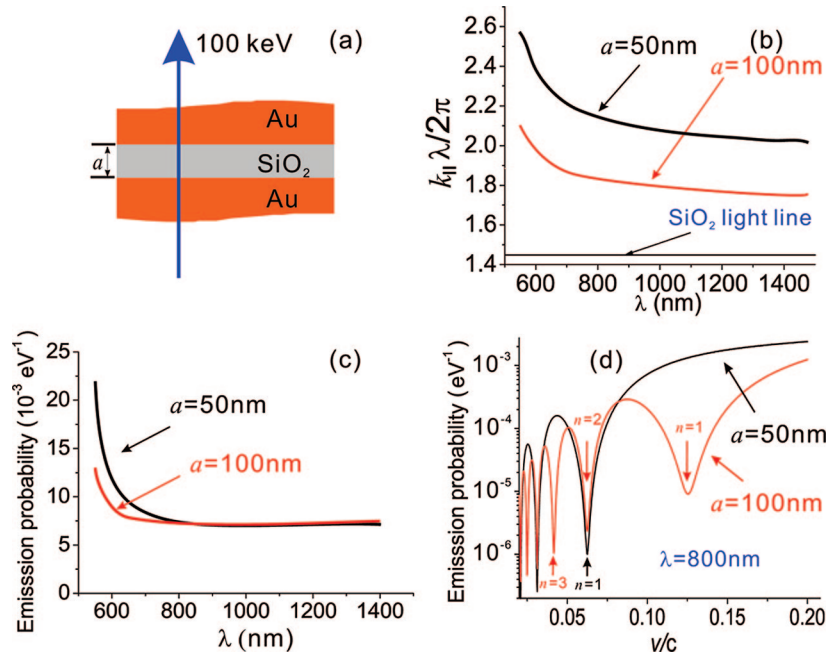
Figure 3. Plasmon generation in planar dielectric cavities. Only the symmetric plasmon mode is well-defined for the $a = 50-100$ nm cavities under consideration (b) (the antisymmetric mode is strongly attenuated). The plasmon generation probability per incoming electron and unit of plasmon energy range is given in (c) as a function of free-space wavelength for 100 keV electrons ($v = 0.55c$) and in (d) as a function of electron velocity for emission of plasmons corresponding to a free-space light wavelength of 800 nm. The arrows in (d) represent the predicted dip positions according to eq 1.

given in the Supporting Information. It is based upon a closed expansion of the electromagnetic field in the space of the parallel wavevector $\mathbf{k}_\parallel$ ($\perp \hat{\mathbf{z}}$) and frequency ω, so that the electric field is written as

$$\mathbf{E}(\mathbf{r}, t) = \int \frac{d^2\mathbf{k}_\parallel \, d\omega}{(2\pi)^3} e^{i\mathbf{k}_\parallel \cdot (x,y) - i\omega t} \mathbf{E}(\mathbf{k}_\parallel, z, \omega)$$

The final expression for the probability (eq 2 in Supporting Information) is written for each plasmon mode n, defined by its dispersion relation $k_\parallel = k_{\parallel,n}$.

Figure 1 illustrates the excitation of SPPs in a free-standing gold film by 100 keV electrons (we take the dielectric function of gold from tabulated optical data).[32] Thin films have two types of SPP modes characterized by symmetric and antisymmetric distributions of both the normal electric field and the magnetic field across the film.[4,5,33] The former are less localized to the surface, as indicated by their parallel momentum, which is closer to the light cone $k_\parallel = k$. In the thin-film limit, the probability of exciting symmetric modes is very low because there is charge cancelation in the interaction of the electron with opposite induced charges associated to these modes on each side of the film[33] (see inset in Figure 1c). In contrast, charges contribute constructively in both sides for antisymmetric modes, to which the electron therefore couples strongly in thin films. For thick films, both symmetric and antisymmetric modes are excited with similar probability, which eventually converges to the probability for creating plasmons in a semi-infinite metal. The excitation yield exhibits a slow decrease with wavelength in all cases, so that the electron is acting as a relatively smooth supercontinuum plasmon source.

A gold film in an asymmetric environment presents an interesting scenario in which the symmetric plasmon branch becomes leaky, since it lies inside the light cone of the substrate.[5] Leaky modes are in fact infinitely delocalized, and one expects this to result in stronger coupling to the electron over an extended path length along its trajectory. This is actually the case, as shown in Figure 2 for gold films supported on silica (the dielectric function of silica is taken from ref 34 in this work). The excitation yield of leaky modes is several orders of magnitude larger compared to antisymmetric modes (cf. parts b and c of Figure 2). This strong coupling grows with decreasing metal film thickness, in accordance with the increasing degree of delocalization in that limit (Figure 2d), and because, unlike the symmetric environment situation, charge cancelation in the upper and lower interfaces is prevented by the breaking of symmetry produced by the substrate. The antisymmetric mode shows a similar trend of increasing excitation probability with decreasing metal film thickness similar to the free-standing film of Figure 1d.

Buried structures such as MIM cavities have attracted much interest in recent years due to their ability to produce extreme confinement[35] and effective negative index of refraction[36] of guided surface plasmons. Any excitation created in a MIM structure must be either absorbed by the metal or propagated as a cavity plasmon until it reaches its ends or is absorbed as well. The excitation yield takes values similar to that for the modes of the complementary metal film (cf. Figures 1c,d and 3c).

An interesting aspect of electron-induced plasmon excitation in MIM cavities is that the electron crosses a
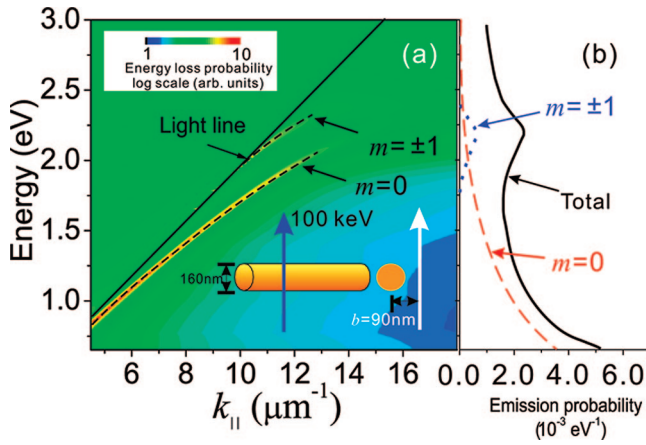
Figure 4. Coupling of an electron beam to metallic-wire plasmons. (a) Energy-loss probability of electrons passing at a distance of 10 nm from the surface of an infinitely long free-standing gold wire of 160 nm in diameter. The probability is decomposed into contributions arising from different values of the wavevector transfer along the wire axis $k_{||}$, according to eq 2. The probability exhibits maxima corresponding to excitation of plasmon modes with $m = 0, \pm 1$ azimuthal symmetry. The dispersion relation of $m = 0$ and $m = \pm 1$ guided plasmons is superimposed for comparison (dashed curves). (b) EELS probability integrated over parallel momentum (solid curve), and partial contributions of $m = 0$ and $m = \pm 1$ plasmon modes (dashed and dotted curves, respectively).

metal–insulator interface twice (on entrance to and exit from the cavity) with a delay determined by the ratio of the cavity width to the electron velocity, a/v. These two points of crossing act as localized sources of transition radiation[20,21] that can interfere with each other, thus producing oscillations of the symmetric-plasmon excitation yield with varying electron velocity (and also with varying angle of the trajectory for oblique incidence, which affects the noted delay as well). This prediction is fully confirmed by the calculations presented in Figure 3d, in which the dips are signaled by out-of-phase interference corresponding to the geometrical condition

$$\frac{(a/v)}{(\lambda/c)} = n \qquad (1)$$

where n is an integer. The dips predicted by this formula (arrows in Figure 3d) are remarkably close to the actual dips of the full calculation. Notice that n rather than $n + 1/2$ enters this equation, leading to dips corresponding to in-phase contributions from both interface crossings. This apparent contradiction stems from the fact that the polarization produced by the electron in the metal is opposite in direction for exit and entrance crossings, which explains the half-period term missing in the above formula (cf. the electron charge distribution for the symmetric mode in the inset of Figure 1c). Further support for this interpretation comes from the fact that a cavity of width $a = 50$ nm shows only half as many dips as a cavity with $a = 100$ nm (Figure 3d).

Fast electrons can also launch plasmons in laterally confined waveguides, for instance in a metallic wire.[25,26] We consider in Figure 4 the plasmon generation probability for an electron passing near an infinite gold wire of circular cross section and 160 nm in diameter. Plasmon excitation produces a relevant contribution to the electron energy loss. It is useful to consider the full EELS probability

$$\Gamma(\omega) = \int_0^\infty dk_{||} \, \Gamma(k_{||}, \omega)$$

which we decompose here into contributions arising from different energy losses $\hbar\omega$ and wavevector components $k_{||}$ along the metal wire. This probability is obtained from the retarding force produced by the induced electric field acting back on the electron as[37]

$$\Gamma(k_{||}, \omega) = \frac{e}{\pi^2 \hbar \omega} \int dt \, \mathrm{Re}\{e^{-i\omega t} \mathbf{v} \cdot \mathbf{E}^{\mathrm{ind}}(k_{||}, b, vt, \omega)\} \qquad (2)$$

where

$$E^{\mathrm{ind}}(k_{||}, b, vt, \omega) = \int dx \, e^{-ik_{||}x} E^{\mathrm{ind}}(x, b, vt, \omega)$$

is the Fourier transform of the induced field along the direction x parallel to the wire, the electron trajectory is described by $z = vt$, and b is the *impact parameter* of the electron beam relative to the wire axis. $\Gamma(k_{||}, \omega)$ is directly related to the photonic local density of states in the vicinity of the wire.[38] Figure 4 shows that the electron is efficiently exciting plasmons with $m = 0$ symmetry (i.e., with $\exp(im\phi)$ dependence on the azimuthal angle ϕ). Also, $m = \pm 1$ modes are excited with smaller probability at higher energies as compared to the $m = 0$ modes. The plasmon-generation yield is shown in Figure 4b as obtained from the integral of $\Gamma(k_{||}, \omega)$ over $k_{||}$ in the region near the $m = 0$ (dashed curve) and $m = \pm 1$ (dotted curve) modes, and compared to the total loss probability (solid curve). Incidentally, these results are not very sensitive to the actual value of b, although grazing trajectories (b close to the radius) can provide the necessary large $k_{||}$ components to efficiently excite plasmons near the dispersion cutoff.

Coupling between plasmons in neighboring metallic particles has been the source of intense research for its application to waveguiding.[8,9,39] We discuss next the excitation of plasmon signals in particle arrays. Figure 5 represents the electric field produced by an electron passing near one end of 51 gold particles with a diameter of 160 nm spaced by a center-to-center distance of 165 nm. We obtain the induced electric field $E^{\mathrm{ind}}(x, \omega)$ from a multiple elastic scattering of multipolar expansions (MESME) formalism,[40] with converged results achieved after inclusion of multiples of orders $l \leq 12$. The field is strongly peaked near $\hbar\omega = 2$ eV (see Figure 5b), and it extends along the entire string (the total array length $\overline{AB}$ is 8.25 μm). It is instructive to examine the time evolution of the field (Figure 5c), which we obtain from the Fourier transform $E^{\mathrm{ind}}(x, t) = (2\pi)^{-1} \int d\omega \exp(-i\omega t) E^{\mathrm{ind}}(x, \omega)$. The electron interacts strongly with the string end as it passes nearby, but the induced field evolves along the string creating a pulse with central speed $\sim 0.75c$ (see dashed line in Figure 5c, drawn along the centroid of the pulse) in excellent agreement with the group velocity at the maximum intensity of the light dispersion curve (dashed curve in Figure 5d); although a wide spectral range of plasmons is excited, there is a preferred energy around 1.9 eV.

A similar analysis can be performed for nanowires of finite length (Figure 6). In particular, Figure 6b shows the propagation of the plasmon launched by the passing electron and successively reflected at the ends of a 160 nm diameter, 3 μm long gold wire (Figure 6c). Similar to the particle chain,
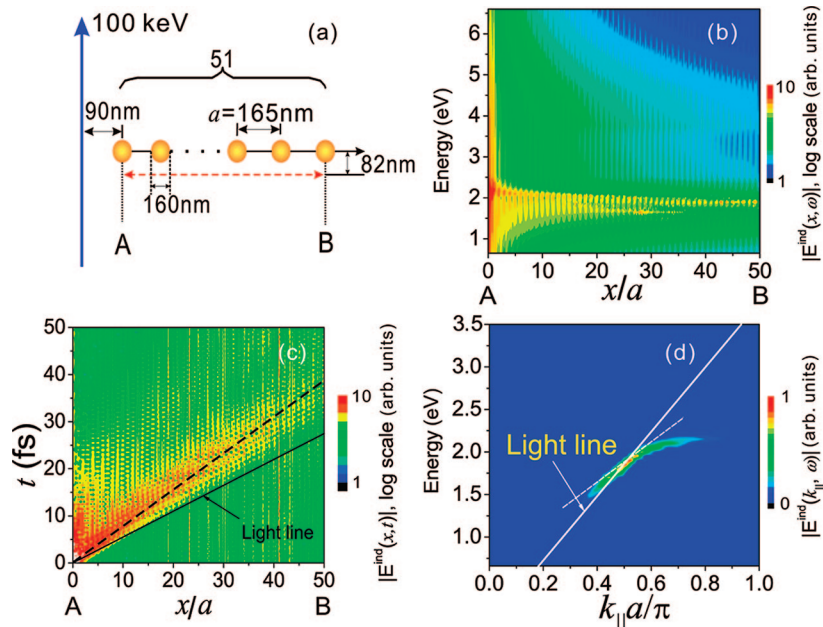
Figure 5. Electron-beam-induced plasmon generation in nanoparticle chains. (a) Scheme of the structure and geometry under consideration. (b) Induced electric field $E^{ind}(x, \omega)$ (in frequency space ω) produced by the electron along the points of the $\overline{AB}$ segment (see red double arrow in (a)). (c) Same as (b), in the time domain: $E^{ind}(x, t)$. (d) Fourier transform of $E^{ind}(x, \omega)$ with respect to x, showing the dispersion relation of plasmons excited by the electron and propagating along the chain. The velocity of the launched pulse is found to be ∼0.75c (dashed line in (c)), in good agreement with the group velocity at the maximum of excitation probability along the guided-mode dispersion curve (dashed line in (d)).
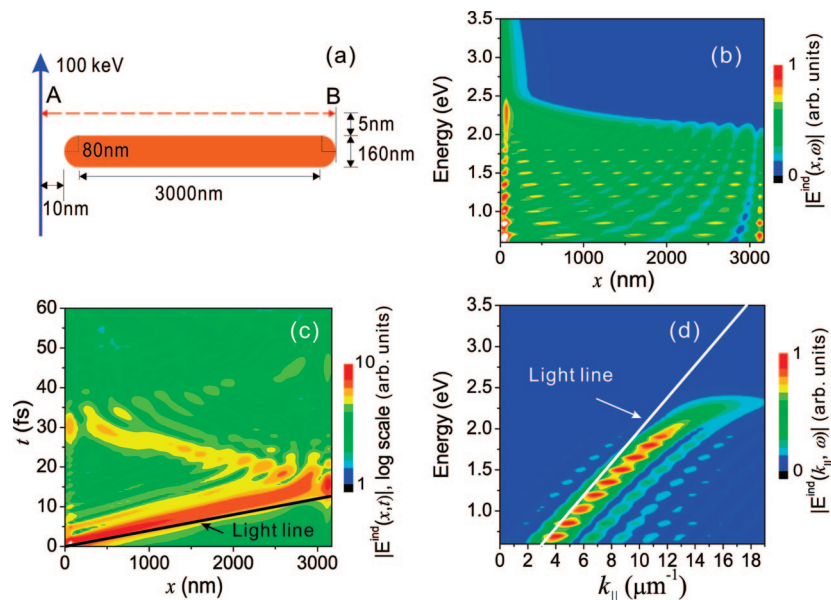
Figure 6. Temporal evolution of plasmons in finite nanowires. (a) Sketch of the geometry considered for excitation of nanowire plasmons by a 100 keV electron beam passing near one of the ends of a gold wire. (b) Induced electric field $E^{ind}(x, \omega)$ (in frequency space ω) produced by the electron along the points of the $\overline{AB}$ segment (see red double arrow in (a)). (c) Same as (b), in the time domain: $E^{ind}(x, t)$. (d) Fourier transform of $E^{ind}(x, \omega)$ with respect to x, showing the dispersion relation of plasmons excited by the electron and propagating along the nanowire.

the plasmon wavepacket evolves with a distinct group velocity ($v \sim 0.8c$), but the propagation distance is much larger in this case, leading to standing waves that are best resolved in Figure 6b: see the intensity maxima that are aligned along horizontal lines in the plot, corresponding to the quantization condition $\Delta k_{\parallel} = \pi/L = 1.0 \ \mu m^{-1}$, where L = 3160 nm is the wire length. The same maxima show up in the dispersion relation of the $m = 0$ plasmon line in Figure

6d at equally spaced intervals in $k_{\parallel}$. The number of maxima along the rod increases with energy according to the same quantization condition. Modes with 4, 5,..., 11 antinodes are clearly discernible in Figure 6b. Furthermore, replicas of the plasmon mode dispersion can be observed in Figure 6d, separated by $\Delta k_{\parallel} \sim \pi/L$.

In conclusion, we have shown that fast electrons passing near nanostructured metals or crossing their boundaries can

generate propagating surface plasmons with high efficiency. Electrons can be actually regarded as a source of evanescent optical fields that are ideally suited to couple to trapped modes such as plasmons, because those modes are also evanescent in the direction of confinement. These ideas are clearly illustrated in the generation of metallic-thin-film plasmons. In particular, the excitation of leaky plasmons in a metal film supported on an insulator leads to very intense leaky-plasmon emission, which eventually decays into light in the insulator, thus providing an efficient mechanism for supercontinuum light emission at subluminal velocities (i.e., at electron energies below the Cherenkov threshold in the insulator) assisted by the metal film. The efficient coupling between electron beams and SPPs is a universal phenomenon that can be exploited to generate plasmons in systems such as nanowires, particle arrays, and any other plasmon-supporting metal structures. We have followed the temporal evolution of the electron-generated plasmon pulses in particle arrays and nanorods of finite length, which move with principal velocity components that are well described by the plasmon group velocity, as calculated for infinitely long particle arrays and nanowires, respectively. In brief, our study reveals high yields of plasmon excitation by fast electrons, thus showing that electron bombardment constitutes a practical solution to the standing problem of plasmon generation at designated positions with high efficiency.

Supporting Information Available: Analytical formalism for plasmon creation in thin films and buried planar cavities. This material is available free of charge via the Internet at http://pubs.acs.org.

References

(1) Barnes, W. L.; Dereux, A.; Ebbesen, T. W. *Nature* **2003**, *424*, 824–830.
(2) Zia, R.; Schuller, J. A.; Chandran, A.; Brongersma, M. L. *Mater. Today* **2006**, *9*, 20–27.
(3) Sarid, D. *Phys. Rev. Lett.* **1981**, *47*, 1927–1930.
(4) Berini, P. *Phys. Rev. B* **2000**, *61*, 10484–10503.
(5) Berini, P. *Phys. Rev. B* **2001**, *63*, 125417.
(6) Bozhevolnyi, S. I.; Volkov, V. S.; Devaux, E.; Laluet, J. Y.; Ebbesen, T. W. *Nature* **2006**, *440*, 508–511.
(7) Bozhevolnyi, S. I.; Erland, J.; Leosson, K.; Skovgaard, P. M. W.; Hvam, J. M. *Phys. Rev. Lett.* **2001**, *86*, 3008–3011.
(8) Quinten, M.; Leitner, A.; Krenn, J. R.; Aussenegg, F. R. *Opt. Lett.* **1998**, *23*1331–1333.
(9) Maier, S. A.; Kik, P. G.; Atwater, H. A.; Meltzer, S.; Harel, E.; Koel, B. E.; Requicha, A. A. G. *Nat. Mater.* **2003**, *2*, 229–232.
(10) Moreno, E.; Rodrigo, S. G.; Bozhevolnyi, S. I.; Martín-Moreno, L.; García-Vidal, F. J. *Phys. Rev. Lett.* **2008**, *100*, 023901.
(11) Manjavacas, A.; García de Abajo, F. J. *Nano Lett.* DOI 10.1021/nl802044t.
(12) Oulton, R. F.; Sorger, V. J.; Genov, D. A.; Pile, D. F. P.; Zhang, X. *Nat. Photonics* **2008**, *2*, 496–500.
(13) Bashevoy, M. V.; Jonsson, F.; Krasavin, A. V.; Zheludev, N. I.; Chen, Y.; Stockman, M. I. *Nano Lett.* **2006**, *6*, 1113–1115.
(14) van Wijngaarden, J. T.; Verhagen, E.; Polman, A.; Ross, C. E.; Lezec, H. J.; Atwater, H. A. *Appl. Phys. Lett.* **2006**, *88*, 221111.
(15) Peale, R. E.; Lopatiuk, O.; Cleary, J.; Santos, S.; Henderson, J.; Clark, D.; Chernyak, L.; Winningham, T. A.; Del Barco, E.; Heinrich, H.; Buchwald, W. R. *J. Opt. Soc. Am. B* **2008**, *25*, 1708–1713.
(16) Ritchie, R. H.; Ashley, J. C.; Emerson, L. C. *Phys. Rev.* **1964**, *135*, A759–A763.
(17) Heitmann, D. *J. Phys. C* **1977**, *10*, 397–405.
(18) Chen, C. H.; Silcox, J. *Phys. Rev. Lett.* **1975**, *35*, 390–393.
(19) Pettit, R. B.; Silcox, J.; Vincent, R. *Phys. Rev. B* **1975**, *11*, 3116–3123.
(20) Ginzburg, V. L.; Frank, I. M. *Zh. Eksp. Teor. Fiz. [Sov. Phys. JETP]* **1946**, *16*, 15–28.
(21) Landau, L. D.; Lifshitz, E. M.; Pitaevskii, L. P. *Electrodynamics of Continuous Media*; Pergamon Press: Oxford, 1984.
(22) Kuttge, M.; Vesseur, E. J. R.; Koenderink, A. F.; Lezec, H. J.; Atwater, H. A.; García de Abajo, F. J.; Polman, A. *Phys. Rev. B* **2009**, in press.
(23) Yamamoto, N.; Araya, K.; García de Abajo, F. J. *Phys. Rev. B* **2001**, *64*, 205419.
(24) Yamamoto, N.; Nakano, M.; Suzuki, T. *Surf. Interface Anal.* **2006**, *38*, 1725–1730.
(25) Vesseur, E. J. R.; de Waele, R.; Kuttge, M.; Polman, A. *Nano Lett.* **2007**, *7*, 2843–2846.
(26) Gómez-Medina, R.; Yamamoto, N.; Nakano, M.; García de Abajo, F. J. *New J. Phys.* **2008**, *10*, 105009.
(27) Bashevoy, M. V.; Jonsson, F.; MacDonald, K. F.; Chen, Y.; Zheludev, N. I. *Opt. Express* **2007**, *15*, 11313–11320.
(28) Hofmann, C. E.; Vesseur, E. J. R.; Sweatlock, L. A.; Lezec, H. J.; García de Abajo, F. J.; Polman, A.; Atwater, H. A. *Nano Lett.* **2007**, *7*, 3612–3617.
(29) Vesseur, E. J. R.; de Waele, R.; Lezec, H. J.; Atwater, H. A.; García de Abajo, F. J.; Polman, A. *Appl. Phys. Lett.* **2008**, *92*, 083110.
(30) Nelayah, J.; Kociak, M.; Stéphan, O.; García de Abajo, F. J.; Tencé, M.; Henrard, L.; Taverna, D.; Pastoriza-Santos, I.; Liz-Marzán, L. M.; Colliex, C. *Nat. Phys.* **2007**, *3*, 348–353.
(31) Bosman, M.; Keast, V. J.; Watanabe, M.; Maaroof, A. I.; Cortie, M. B. *Nanotechnology* **2007**, *18*, 165505.
(32) Johnson, P. B.; Christy, R. W. *Phys. Rev. B* **1972**, *6*, 4370–4379.
(33) Raether, H. *Surface Plasmons on Smooth and Rough Surfaces and on Gratings*; Springer Tracks in Modern Physics, 111; Springer-Verlag: Berlin, 1988.
(34) Palik, E. D. *Handbook of Optical Constants of Solids*; Academic Press: New York, 1985.
(35) Miyazaki, H. T.; Kurokawa, Y. *Phys. Rev. Lett.* **2006**, *96*, 097401.
(36) Lezec, H. J.; Dionne, J. A.; Atwater, H. A. *Science* **2007**, *316*, 430–432.
(37) Ritchie, R. H. *Phys. Rev.* **1957**, *106*, 874–881.
(38) García de Abajo, F. J.; Kociak, M. *Phys. Rev. Lett.* **2008**, *100*, 106804.
(39) Koenderink, A. F.; Polman, A. *Phys. Rev. B* **2006**, *74*, 033402. Koenderink, A. F.; de Waele, R.; Prangsma, J. C.; Polman A., *Phys. Rev. B* **2007**, *76*, 201403.
(40) García de Abajo, F. J. *Phys. Rev. Lett.* **1999**, *82*, 2776–2779. García de Abajo, F. J. *Phys. Rev. B* **1999**, *60*, 6103–6112.

NL803825N

Observation of nonlinear surface waves in modulated waveguide arrays

Xinyuan Qi,[1,2,*] Ivan L. Garanovich,[1] Zhiyong Xu,[1] Andrey A. Sukhorukov,[1] Wieslaw Krolikowski,[1] Arnan Mitchell,[3] Guoquan Zhang,[2] Dragomir N. Neshev,[1] and Yuri S. Kivshar[1]

[1]*Nonlinear Physics Centre and Laser Physics Centre, Research School of Physics and Engineering, Australian National University, Canberra, ACT 0200, Australia*
[2]*The Key Laboratory of Weak Light Nonlinear Photonics, Ministry of Education, Nankai University, Tianjin 300457, China*
[3]*School of Electrical and Computer Engineering and Centre for Ultra-high Bandwidth Devices for Optical Systems (CUDOS), Royal Melbourne Institute of Technology University, Melbourne, VIC 3001, Australia*
*Corresponding author: qixycn@gmail.com

We describe theoretically and study experimentally nonlinear surface waves at the edge of a modulated waveguide array with a surface defect and a self-defocusing nonlinearity. We fabricate such structures in a LiNbO$_3$ crystal and demonstrate the beam switching to different output waveguides with a change of the light intensity due to nonlinear coupling between the linear surface modes supported by the array. © 2009 Optical Society of America

OCIS codes: 190.0190, 240.6690, 190.6135.

The study of surface waves in periodic photonic structures such as photonic crystals or optical lattices is attracting increasing attention. Their basic properties have many similarities to the physics of electrons localized at crystalline surfaces, which were first discussed by Tamm [1] and Shockley [2]. The direct observations of such states have been performed only in photonic systems [3,4], such as periodic waveguide arrays. It was found that strong surface localization is possible when the edge waveguide is modified and the defect strength exceeds a certain threshold, in agreement with original predictions by Tamm [1]. Such a surface defect can also be induced through optical nonlinearity, resulting in the formation of surface lattice solitons [5–11]. On the other hand, it was recently demonstrated that arrays of periodically curved waveguides can support a novel type of linear surface modes without any surface defects [12,13].

In this Letter, we describe theoretically and observe experimentally nonlinear surface waves at the edge of modulated waveguide arrays. We demonstrate nontrivial beam dynamics due to an interplay between three mechanisms of surface localization: (i) waveguide bending, (ii) fabricated surface defect, and (iii) nonlinear beam self-action. First, we present the theoretical classification of linear surface modes supported by the curved arrays with a surface defect. Next, we demonstrate experimentally that nonlinear beam self-action can provide effective control of the output beam profile, including switching between different waveguides near the surface.

We fabricate arrays of modulated waveguides by titanium indiffusion in a 50-mm-long X-cut LiNbO$_3$ crystal with defocusing photorefractive nonlinearity [14], featuring a transverse refractive index profile containing a negative surface defect (lower refractive index value at the first waveguide) [see Fig. 1(a)]. We choose the waveguide bending profile composed of sinusoidal sections, $x_0(z) = A[\cos(4\pi z/L) - 1]$ for $0 < z$

$< L/2$, $x_0(z) = -x_0(z - L/2)$ for $L/2 < z < L$, and $x_0(z) = x_0(z-L)$ for $z > L$ [see sketch in Fig. 1(a)]. Here x_0 is the transverse waveguide shift, z is the longitudinal coordinate, and A and L are the waveguide axes bending amplitude and period, respectively. Two curved arrays with different bending amplitudes ($A = 21.5$ μm and $A = 24.5$ μm) are fabricated. Both samples contain one full bending period of $L = 50$ mm.

It was shown that, away from the boundaries, the linear beam diffraction in a curved array appears the same after each bending period as in a straight array with the effective coupling coefficient C_e [15–18]. For our bending profile, $C_e = C J_0[\xi A/A_0]$, where C is the
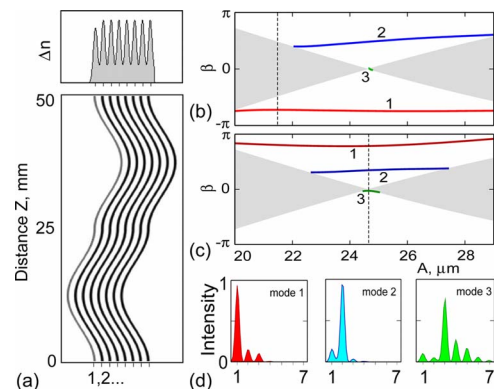
Fig. 1. (Color online) Linear surface modes in a curved waveguide array with a surface defect. (a) Schematic of the array (bottom) and index change (top). (b), (c) Propagation constants of linear surface modes versus waveguide bending amplitude A for surface defects (b) $\rho_1 = -0.52$ and (c) $\rho_1 = -0.56$. Gray shading marks the array transmission band, and the vertical dashed line corresponds to (b) $A = 21.5$ μm and (c) $A = 24.5$ μm. (d) Intensity profiles at $z = 0, L$ of three different surface modes for $A = 24.5$ μm, corresponding to mode dispersion lines marked 1–3 in (c).

coupling coefficient in the absence of bending [12], J_0 is the Bessel function of first kind of order 0, $\xi \simeq 2.40$ is its first root, $A_0 = \xi \lambda L / 8\pi^2 n_0 d = 24.6$ μm, $\lambda = 532$ nm is the laser wavelength used in the experiments, $n_0 = 2.35$ is the refractive index of LiNbO$_3$ substrate, and $d = 14$ μm is the spacing between the centers of the adjacent waveguides. Note that the average beam diffraction is completely suppressed ($C_e = 0$) for a set of bending amplitudes including $A = A_0$, analogous to the effect of dynamic localization for electrons in crystals with an applied ac bias field [16].

The curved waveguide arrays can support linear surface modes even in the absence of surface defects [12]. We consider here a more general case when the edge waveguide is modified [Fig. 1(a)]. We use coupled-mode equations to model the beam dynamics [12,16], $i \, da_n/dz + C \exp[-i\dot{x}_0(z)]a_{n+1} + C \exp[i\dot{x}_0(z)]a_{n-1} + \rho_n a_n + \gamma|a_n|^2 a_n = 0$, where $a_n(z)$ are the normalized mode amplitudes, $n = 1, 2 \ldots$ is the waveguide number, and $a_{n \leq 0} \equiv 0$ is due to the structure termination. The value of ρ_1 defines the detuning of the surface waveguide, while $\rho_{n>1} \equiv 0$. We take the value of the normalized nonlinear coefficient $\gamma = -1$ to account for the defocusing photorefractive nonlinearity of LiNbO$_3$. By matching the experimentally measured discrete diffraction pattern in a straight waveguide array, we determine the value of the coupling coefficient $C \simeq 0.09$ mm^{-1}. By measuring the beam propagation close to the boundaries of the curved arrays we estimate the defect strengths as $\rho_1 = -0.52$ in the fabricated sample with $A = 21.5$ μm and $\rho_1 = -0.56$ for the sample with $A = 24.5$ μm.

First, we perform theoretical analysis of the linear surface modes, extending the methods described in [12]. We characterize the mode dispersion with the phase β accumulated over one modulation period and present the mode tuning on the modulation amplitude in Figs. 1(b) and 1(c) for both parameter values of ρ_1. We find that the profiles of the three fundamental modes (marked 1–3) are similar for $\rho_1 = -0.56$ [shown in Fig. 1(d)] and $\rho_1 = -0.52$ (not shown) owing to their common physical origin. Mode 1 is supported by the surface defect, similar to Tamm states [5]; it exists for a wide range of bending amplitudes and has a profile with intensity maximum at the first waveguide [Fig. 1(d), left]. Modes 2 and 3 exist owing to waveguide bending, similar to the defect-free surface states [12]. The input and output mode profiles (at $z = 0, L$) have intensity maxima at the second and third waveguides, respectively [Fig. 1(d), middle and right].

Next, we simulate the beam dynamics under the effect of nonlinear self-action, when light is coupled to a single waveguide number n at the input with the normalized intensity $I = |a_n(0)|^2$. We show the simulated beam evolution in an array with $A = 24.5$ μm in Fig. 2. In Figs. 2(a)–2(d) we excite the first waveguide ($n = 1$). At low powers, in the essentially linear propagation regime, the first (defect) surface mode [Fig. 1(d), left] is excited. At higher input powers, the defocusing nonlinearity increases the strength of the
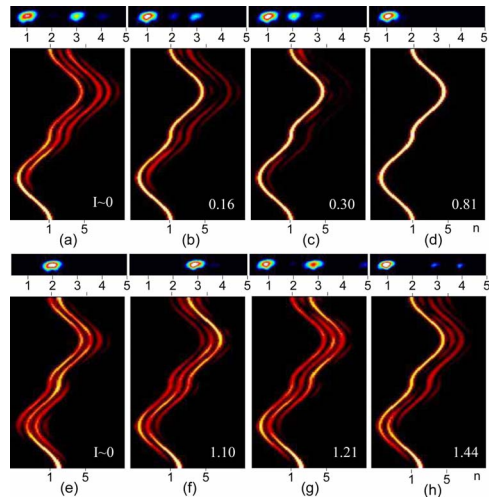
Fig. 2. (Color online) Surface waves in a modulated waveguide array ($A = 24.5$ μm). In each block: top images, experimental results for different illumination times; bottom images, numerical simulations. In (a)–(d) the beam is launched into the first waveguide; in (e)–(h) the second waveguide is excited. (a), (e) Linear propagation: input power 1 μW; illumination time 5 s. In (b)–(d) the illumination times are 0.50, 1.25, and 4.25 min; in (f)–(h) the illumination times are 10.92, 17.67, and 18.42 min, respectively. Input power in (b)–(d) and (f)–(h) is 4 mW. In the numerical calculations the normalized input intensity I is marked in the corners.

negative defect in the first waveguide, and eventually the entire beam becomes trapped in the first waveguide [see Figs. 2(c) and 2(d)].

In Figs. 2(e)–2(h) we excite the second waveguide ($n = 2$). At low light intensity, the second surface mode [Fig. 1(d), middle] is excited. However, at higher intensity, nonlinear coupling and interaction between different linear modes is present. We note that even away from the surface, the nonlinear beam dynamics is highly nontrivial at these power levels [19–22]. We observe switching of the output beam position between the second, third, and first waveguides as we increase the intensity [Figs. 2(f) and 2(g)]. As the input intensity grows further, the beam becomes localized at the edge waveguide [Fig. 2(h)], indicating the formation of a self-trapped nonlinear surface wave. At even higher intensities (not shown) the nonlinearity completely detunes the input channel, and the light becomes trapped back to the second waveguide.

In our experiments, we use the beam from a cw laser ($\lambda = 532$ nm). The beam is ordinary polarized, perpendicularly to the plane of the array, to minimize bending losses and radiation. The nonlinear refractive index change in the photorefractive LiNbO$_3$ depends on the input power and slowly increases with illumination time. We therefore monitor the output intensity distribution onto a CCD camera with increasing illumination until a steady state is reached. We focus the beam to the first and second waveguides and for each case show the output intensity profiles at four different illumination times in Figs. 2(a)–2(h), top images. We observe that as the nonlinear response increases, the output beam switches between the different waveguides. There is good agreement
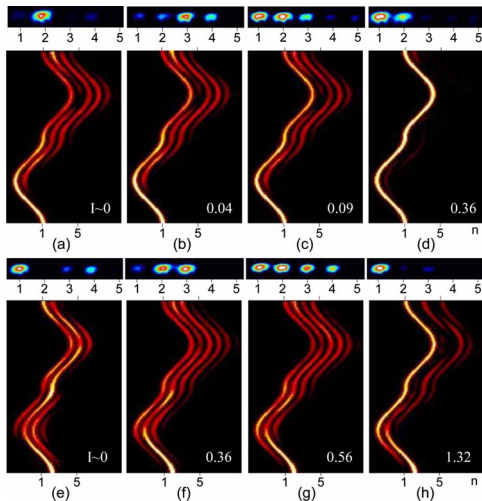
Fig. 3. (Color online) The same as in Fig. 2 but for $A = 21.5$ μm. (a), (e) Linear propagation: power 1 μW; illumination time 5 s. In (b)–(d) and (f)–(h) input power is 4 mW. In (b)–(d) illumination time is 0.33, 4.50, and 7.33 min; in (f)–(h) illumination time is 1.00, 3.08, and 13.33 min, respectively.

between the experiments and numerical simulations, except at very high input powers, when we register a slow oscillatory beam motion between the first two waveguides owing to the charge dynamics in photorefractive crystal, which is not described by the coupled-mode equations.

Figure 3 shows numerical and experimental results for the second sample with bending amplitude $A = 21.5$ μm. In this case a band of extended linear states coexist together with a single linear surface mode [see dashed line in Fig. 1(b)]. Therefore we also identify the presence of leaky surface modes, which remain quasi localized for our sample length. Beating between all these modes determines beam propagation in the linear regime, as shown in Figs. 3(a) and 3(e). As we increase the input powers/illumination times, we observe complex beam reshaping and switching, which depends on the nonlinearity strength; see Figs. 3(b)–3(d) and Figs. 3(f)–3(h). We note that in Fig. 3(b) the experimental intensity distribution is affected by the transient beam dynamics owing to the short illumination time.

In conclusion, we have studied surface modes in modulated waveguide arrays, which demonstrate the features of both optical Tamm states and discrete surface solitons. We have shown that the interplay of different surface modes types enables novel means of light shaping and switching between different output waveguides.

References

1. I. E. Tamm, Z. Phys. **76**, 849 (1932).
2. W. Shockley, Phys. Rev. **56**, 317 (1939).
3. P. Yeh, A. Yariv, and A. Y. Cho, Appl. Phys. Lett. **32**, 104 (1978).
4. N. Malkova, I. Hromada, X. S. Wang, G. Bryant, and Z. G. Chen, Opt. Lett. **34**, 1633 (2009).
5. K. G. Makris, S. Suntsov, D. N. Christodoulides, G. I. Stegeman, and A. Hache, Opt. Lett. **30**, 2466 (2005).
6. S. Suntsov, K. G. Makris, D. N. Christodoulides, G. I. Stegeman, A. Hache, R. Morandotti, H. Yang, G. Salamo, and M. Sorel, Phys. Rev. Lett. **96**, 063901 (2006).
7. Y. V. Kartashov, V. A. Vysloukh, and L. Torner, Phys. Rev. Lett. **96**, 073901 (2006).
8. G. A. Siviloglou, K. G. Makris, R. Iwanow, R. Schiek, D. N. Christodoulides, G. I. Stegeman, Y. Min, and W. Sohler, Opt. Express **14**, 5508 (2006).
9. E. Smirnov, M. Stepic, C. E. Ruter, D. Kip, and V. Shandarov, Opt. Lett. **31**, 2338 (2006).
10. C. R. Rosberg, D. N. Neshev, W. Krolikowski, A. Mitchell, R. A. Vicencio, M. I. Molina, and Yu. S. Kivshar, Phys. Rev. Lett. **97**, 083901 (2006).
11. W. H. Chen, Y. J. He, and H. Z. Wang, Opt. Express **14**, 11271 (2006).
12. I. L. Garanovich, A. A. Sukhorukov, and Yu. S. Kivshar, Phys. Rev. Lett. **100**, 203904 (2008).
13. A. Szameit, I. L. Garanovich, M. Heinrich, A. A. Sukhorukov, F. Dreisow, T. Pertsch, S. Nolte, A. Tunnermann, and Yu. S. Kivshar, Phys. Rev. Lett. **101**, 203902 (2008).
14. M. Matuszewski, C. R. Rosberg, D. N. Neshev, A. A. Sukhorukov, A. Mitchell, M. Trippenbach, M. W. Austin, W. Krolikowski, and Yu. S. Kivshar, Opt. Express **14**, 254 (2006).
15. H. S. Eisenberg, Y. Silberberg, R. Morandotti, and J. S. Aitchison, Phys. Rev. Lett. **85**, 1863 (2000).
16. S. Longhi, M. Marangoni, M. Lobino, R. Ramponi, P. Laporta, E. Cianci, and V. Foglietti, Phys. Rev. Lett. **96**, 243901 (2006).
17. I. L. Garanovich, A. A. Sukhorukov, and Yu. S. Kivshar, Phys. Rev. E **74**, 066609 (2006).
18. R. Iyer, J. S. Aitchison, J. Wan, M. M. Dignam, and C. M. de Sterke, Opt. Express **15**, 3212 (2007).
19. V. V. Konotrup, O. A. Chubykalo, and L. Vazquezet, Phys. Rev. E **48**, 563 (1993).
20. D. Cai, A. R. Bishop, N. Gronbech-Jensen, and M. Salerno, Phys. Rev. Lett. **74**, 1186 (1995).
21. I. L. Garanovich, A. A. Sukhorukov, and Yu. S. Kivshar, Opt. Express **15**, 9547 (2007).
22. A. Szameit, I. L. Garanovich, M. Heinrich, A. Minovich, F. Dreisow, A. A. Sukhorukov, T. Pertsch, D. N. Neshev, S. Nolte, W. Krolikowski, A. Tunnermann, A. Mitchell, and Yu. S. Kivshar, Phys. Rev. A **78**, 031801 (2008).

Orientation-dependent excitations of lattice soliton trains with hybrid nonlinearity

Yi Hu,[1] Cibo Lou,[1] Sheng Liu,[2] Peng Zhang,[1,2,3] Jianlin Zhao,[2] Jingjun Xu,[1] and Zhigang Chen[1,3,*]

[1]*The Key Laboratory of Weak-Light Nonlinear Photonics, Ministry of Education and TEDA Applied Physics School, Nankai University, Tianjin 300457, China*
[2]*Shaanxi Key Laboratory of Optical Information Technology, School of Science, Northwestern Polytechnical University, Xi'an 710072, China*
[3]*Department of Physics and Astronomy, San Francisco State University, San Francisco, California 94132, USA*
*Corresponding author: zhigang@sfsu.edu

We demonstrate selective excitation of soliton trains residing in different gaps or within the same Bloch band of a new type of photonic lattice merely by changing the orientation of an input probe beam. A self-focusing and -defocusing hybrid nonlinearity as established in a nonconventionally biased photorefractive crystal leads to controlled soliton transitions from different band edges or subband edges, in good agreement with our theoretical analysis. © 2009 Optical Society of America

OCIS codes: 190.6135, 190.5330, 350.4238.

Wave propagation in optical periodic structures has been studied extensively [1], including various types of lattice solitons [2–13]. In general, lattice solitons have been generated with either a self-focusing or de-focusing nonlinearity, which in photorefractive (PR) materials was established simply by changing the polarity of the bias field [4]. Recently, we demonstrated that in a nonconventionally biased (NCB) PR crystal self-focusing and -defocusing nonlinearities coexist, leading to unusual excitation of spatial solitons in the same nonlinear material [14,15].

In this Letter, we demonstrate quasi-1D soliton trains in a new type of photonic lattice induced with periodic positive and negative index changes in a NCB PR crystal. Solely by changing the orientation of an input stripe beam, selective excitation of the soliton trains arising from different gaps or within the continuum spectrum of the Bloch band is realized. We show that the self-focusing and -defocusing *hybrid nonlinearity* supported by the NCB condition is the key for in-band or in-gap soliton excitations and demonstrate for the first time to our knowledge the embedded solitons under a self-focusing nonlinearity.

The theoretical model for nonlinear propagation of a light beam in a 2D photonic lattice under the NCB condition was developed earlier [15]. Different from the conventional bias condition [4–8], here we keep the bias field perpendicular to the crystalline c-axis ($E \perp c$), i.e., $\theta_e = 3\pi/4$, $\theta_c = \pi/4$ as shown in Fig. 1(a). Thus, the dimensionless equations become [15,16]

$$\left(\frac{\partial}{\partial z} - \frac{i}{2}\nabla^2\right)B(\vec{r}) = i\frac{\sqrt{2}}{2}\left(\frac{\partial\varphi}{\partial x} + \frac{\partial\varphi}{\partial y}\right)B(\vec{r}), \quad (1a)$$

$$\nabla^2\varphi + \nabla\varphi\cdot\nabla\ln(1+I) = -\frac{\sqrt{2}}{2}E_0\left(\frac{\partial}{\partial x} - \frac{\partial}{\partial y}\right)\ln(1+I),$$
$$(1b)$$

where $\nabla = \hat{x}(\partial/\partial x) + \hat{y}(\partial/\partial y)$, $B(\vec{r})$ is the amplitude of the probe beam, φ is the light-induced electrostatic

potential, E_0 is the bias field, $I = V(x,y) + |B(\vec{r})|^2$ is the normalized total intensity, and $V(x,y) = \cos^2(\pi x/\Lambda)\cos^2(\pi y/\Lambda)$ is the intensity of the lattice-inducing beam with a spatial period Λ. Solving Eq. (1) yields the induced refractive index changes (lattice) depicted in Fig. 1(b), dramatically different from the intensity pattern of the lattice-inducing beam [Fig. 1(a)]. In fact, the index lattice has both periodic positive and negative index changes, akin to a typical ionic lattice structure in solids. Figure 1(c) shows the first Bloch band structure with marked high-symmetry points within the first Brillouin zone corresponding to the 2D lattice of Fig. 1(b).

Although in-gap and in-band soliton trains have been observed before under different conventional bias conditions, they were generated in 2D lattices with either all-positive or all-negative index changes under a fixed self-focusing or -defocusing nonlinearity. Different from the fixed type of nonlinearity [8,12,13] under the conventional bias condition, a 1D stripe beam can experience self-focusing or
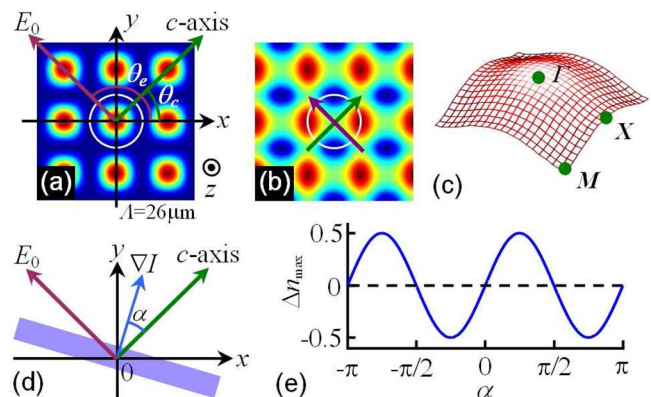
Fig. 1. (Color online) (a) Illustration of the bias condition with respect to the lattice-inducing beam; (b) induced refractive index pattern; (c) first Bloch band diagram with marked high-symmetry points; (d) illustration of the bias condition with respect to the input stripe beam (shaded); (e) normalized maximum light-induced index change versus α at $E_0 = 1$.

-defocusing nonlinearity in our NCB bias condition, depending on the relative orientation (angle α) of its intensity gradient ∇I with respect to the c axis [Fig. 1(d)]. The strongest self-focusing or -defocusing nonlinearity occurs at $\alpha = \pi/4$ or $\alpha = -\pi/4$, where the stripe beam is oriented horizontally (parallel to the x axis) or vertically, inducing the maximum positive or negative index change [Fig. 1(e)] [14]. We shall use this orientation-dependent hybrid nonlinearity for excitation of different types of soliton train in the same 2D lattice of Fig. 1(b).

The soliton solution of Eq. (1) can be found in the form $B(x,y,z) = b(x,y) \exp(i\beta z)$, where β is the propagation constant and the envelope function $b(x,y)$ satisfies the following equation:

$$\left(\beta - \frac{1}{2} \nabla^2 \right) b(x,y) = \frac{\sqrt{2}}{2} \left(\frac{\partial \varphi}{\partial x} + \frac{\partial \varphi}{\partial y} \right) b(x,y). \quad (2)$$

Solving Eq. (1) and (2) yields solutions for soliton trains of different orientations as bifurcated from different high-symmetry points of the first Bloch band. Figures 2(a) and 2(b) depict the power curves of these soliton trains, where the power is defined over one period along the train direction [12,13]. Figure 2(a) corresponds to soliton solutions in the semi-infinite gap (curve labeled c) and those in the first photonic gap (curve labeled d). These are in-gap solitons with modes bifurcated from the band edges (corresponding to points Γ and M). In contrast, Fig. 2(b) shows soliton solutions with modes bifurcated from the subband edges (corresponding to interior points X). These are in-band or embedded solitons [13,17]. In Figs. 2(c)–2(f), we depict the intensity patterns, phase structures, and **k**-space spectra of typical soliton solutions corresponding to the marked points in

Figs. 2(a) and 2(b). Although the intensity patterns look somewhat similar, the phase structures and spectra indicate that they have different origins under different nonlinearities. Specifically, Figs. 2(c) represent a discrete soliton train bifurcated from point Γ under a self-focusing nonlinearity, and Figs. 2(d) and 2(f) represent an in-gap and in-band soliton train bifurcated from points M and X under a self-defocusing nonlinearity, respectively, all established with the same lattice structure under the same bias condition. Furthermore, the soliton train shown in Figs. 2(e) represents an embedded soliton train bifurcated from the X points under a self-focusing nonlinearity. Comparing Figs. 2(e) and 2(f), not only the orientations but also the spectra near the two points X are different owing to different initial excitations. Since the diffraction curve at points X has a saddle shape [13], the normal (anomalous) diffraction along a specific direction at point X can be balanced by the self-focusing (-defocusing) nonlinearity experienced by the soliton stripe, provided that it has the right orientation. Thus, embedded solitons can be supported by hybrid nonlinearity.

Our experimental setup is similar to those used in [8,12], except that we now use the NCB condition $(E \perp c)$ for inducing the lattice structure shown in Fig. 1(b). A partially spatially incoherent beam ($\lambda = 532$ nm) created by a rotating diffuser is used to image a periodic amplitude mask into a SBN:60 PR crystal as the lattice-inducing beam shown in Fig. 1(a). A coherent Gaussian beam ($\lambda = 532$ nm) focused by a cylindrical lens is used as the probe beam. The polarization of the probe (lattice) beam is always kept parallel (perpendicular) to the c axis. For the experiments below, the only thing we change is the probe beam orientation. Results for the transition between semi-infinite gap to first photonic gap soliton trains bifurcated from points Γ and M are shown in Fig. 3. To obtain the semi-infinite gap soliton, the stripe beam is oriented horizontally and launched collinearly (without input tilt) with the lattice beam as shown in Fig. 3(a). When the diffraction is balanced by self-focusing, the stripe beam evolves into a discrete soliton train [Figs. 3(b)–3(d)]. To obtain the first

Fig. 2. (Color online) Numerical results of existence curves for soliton trains bifurcated from band edges (a) and subband edge (b) of the first Bloch band. The power P is defined over one period along the train direction. (c)–(f) Soliton solutions at corresponding marked points in (a) and (b), showing the soliton intensity patterns (1), phase structures (2), and Fourier spectra (3). Added squares in the last row depict the boundary of the first Brillouin zone.

Fig. 3. (Color online) Experimental results of discrete (a)–(d) and gap (e)–(h) soliton trains corresponding to Figs. 2(c) and 2(d) obtained in the same lattice setting. From left to right, superimposed input intensity pattern of probe and lattice beams (insets show the spectra of probe beam excitation), output intensity pattern of the soliton trains, interferograms from two orthogonal directions, and soliton output spectra.

photonic gap soliton, the stripe beam is oriented vertically and launched off-site with an input tilt at a Bragg angle as shown in Fig. 3(e). In this case, the self-defocusing nonlinearity experienced by the probe beam balances anomalous diffraction to form a gap soliton train [Fig. 3(f)] with a characteristic staggered phase structure [Fig. 3(g)] and reshaped **k**-space spectrum [12]. These observations are in good agreement with the theoretical results presented in Figs. 2(c) and 2(d).

Finally, we present our experimental results for excitation of in-band soliton trains supported by the hybrid nonlinearity (Fig. 4). To selectively excite the in-band solitons with a self-focusing nonlinearity, the stripe beam is oriented horizontally but launched with an input tilt at a Bragg angle into the lattice as shown in Fig. 4(a). Now the probe beam excites the modes at point X rather than point Γ and thus evolves into an embedded soliton train [Fig. 4(b)], shown also from the phase structure [Fig. 4(c)] and the **k**-space spectrum [Fig. 4(d)]. In this case, the normal diffraction of the stripe beam along the y direction is balanced by the self-focusing nonlinearity, so the soliton is quasi-1D in the x direction. Likewise, the in-band soliton train supported by the self-defocusing nonlinearity can be generated by off-site excitation of a vertically oriented stripe beam but without input tilt as shown in Fig. 4(e). Again the excitation of modes from the points X is evident in both phase and spectrum measurement, but now the soliton is quasi-1D in the y direction. We mention that, as the soliton power increases, the embedded soliton will turn into a semi-infinite gap soliton under self-focusing nonlinearity [moving right to out of the band along branch e in Fig. 2(b)] but into a photonic gap soliton under the self-defocusing nonlinearity [moving left to out of the band along branch f in Fig. 2(b)]. These solitons have also been observed, and we have found their solutions as well.
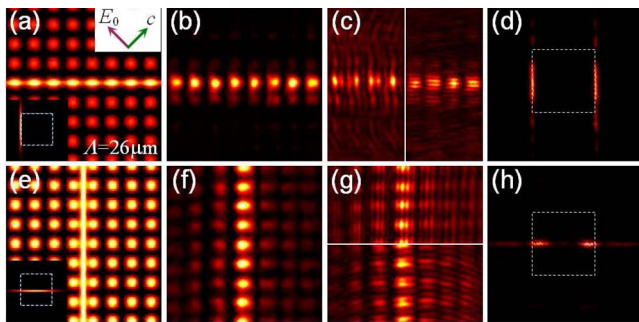
Fig. 4. (Color online) Experimental results of in-band soliton trains bifurcated from point X under self-focusing (a)–(d) and -defocusing (e)–(h) nonlinearity, corresponding to Figs. 2(e) and 2(f). Other descriptions are the same as in Fig. 3.

We have demonstrated selective excitation of soliton trains associated with Bloch modes from different band edges as well as from subband edges in a 2D ionic-type photonic lattice solely by changing the orientation of an input probe beam. Our results may prove relvant to other discrete systems where saddle-shaped dispersion and hybrid nonlinearity are yet to be explored.

References

1. D. N. Christodoulides, F. Lederer, and Y. Silberberg, Nature **424**, 817 (2003).
2. D. N. Christodoulides and R. I. Joseph, Opt. Lett. **13**, 794 (1988).
3. H. S. Eisenberg, Y. Silberberg, R. Morandotti, A. R. Boyd, and J. S. Aitchison, Phys. Rev. Lett. **81**, 3383 (1998).
4. J. W. Fleischer, T. Carmon, M. Segev, N. K. Efremidis, and D. N. Christodoulides, Phys. Rev. Lett. **90**, 023902 (2003).
5. J. W. Fleischer, M. Segev, N. K. Efremidis, and D. N. Christodoulides, Nature **422**, 147 (2003).
6. D. Neshev, E. Ostrovskaya, Y. Kivshar, and W. Królikowski, Opt. Lett. **28**, 710 (2003).
7. H. Martin, E. D. Eugenieva, Z. Chen, and D. N. Christodoulides, Phys. Rev. Lett. **92**, 123902 (2004).
8. Z. Chen, H. Martin, E. D. Eugenieva, J. Xu, and A. Bezryadina, Phys. Rev. Lett. **92**, 143902 (2004).
9. D. Neshev, A. A. Sukhorukov, B. Hanna, W. Krolikowski, and Y. S. Kivshar, Phys. Rev. Lett. **93**, 083905 (2004).
10. Y. S. Kivshar, Opt. Lett. **18**, 1147 (1993).
11. F. Chen, M. Stepić, C. Rüter, D. Runde, D. Kip, V. Shandarov, O. Manela, and M. Segev, Opt. Express **13**, 4314 (2005).
12. C. Lou, X. Wang, J. Xu, Z. Chen, and J. Yang, Phys. Rev. Lett. **98**, 213903 (2007).
13. X. Wang, Z. Chen, J. Wang, and J. Yang, Phys. Rev. Lett. **99**, 243901 (2007).
14. P. Zhang, S. Liu, J. Zhao, C. Lou, J. Xu, and Z. Chen, Opt. Lett. **33**, 878 (2008).
15. P. Zhang, J. Zhao, F. Xiao, C. Lou, J. Xu, and Z. Chen, Opt. Express **16**, 3865 (2008).
16. A. A. Zozulya and D. Z. Anderson, Phys. Rev. A **51**, 1520 (1995).
17. J. Yang, B. A. Malomed, and D. J. Kamp, Phys. Rev. Lett. **83**, 1958 (1999).

Fast responsive nonvolatile holographic storage in LiNbO$_3$ triply doped with Zr, Fe, and Mn

Yongfa Kong,[1,*] Fucai Liu,[2] Tian Tian,[2] Shiguo Liu,[2] Shaolin Chen,[1] Romano Rupp,[1] and Jingjun Xu[1,2]

[1]*The MOE Key Laboratory of Weak-Light Nonlinear Photonics and TEDA Applied Physical School, Nankai University, Tianjin 300457, China*
[2]*School of Physics, Nankai University, Tianjin 300071, China*
Corresponding author: kongyf@nankai.edu.cn

Iron and manganese doubly doped LiNbO$_3$ (LN:Fe,Mn) has been suggested for nonvolatile photorefractive recording; however, its response time is still of the order of minutes. Here we present results on LiNbO$_3$ triply doped with zirconium, iron, and manganese (LN:Zr,Fe,Mn). The codoping with Zr eliminates undesirable intrinsic traps, which strongly enhances the charge transition speed. The response time of LN:Zr,Fe,Mn for nonvolatile holographic storage shortens to only 0.95 s (wavelength of 532 nm and intensity of 400 mW/cm^2), and the sensitivity reaches 1.31 cm/J. Thus it seems that we have found an excellent recording medium for practical holographic storage devices. © 2009 Optical Society of America

OCIS codes: 210.2860, 160.5320, 160.3730.

For many years holographic data storage has been promising to become the next-generation optical storage technology [1–3]. But still this technology has not matured to commercialization. The main obstacle is the lack of an ideal medium [4]. Although lithium niobate [LiNbO$_3$, (LN)] went on to be the mainstay of holographic data storage efforts, several problems—such as low response speed, strong light-induced scattering, and volatility—impede it from becoming a commercial recording medium. Buse *et al.* achieved a nonvolatile two-color recording based on LN doubly doped with iron and manganese (LN:Fe,Mn) that provide shallower and deeper traps [5]. However, the sensitivity of LN:Fe,Mn remains very low, with the response time being of the order of minutes, which is too slow for practical use. To realize a real-time nonvolatile read-write memory, shortening of the response time and improving the sensitivity seem to be the critical challenges.

Recently we reported that when tetravalent ions, such as hafnium (Hf^{4+}) and zirconium (Zr^{4+}), are codoped into iron-doped LN (LN:Fe) crystals above a certain doping threshold, the response time is strongly shortened while the saturation diffraction efficiency remains high, which causes the photorefractive sensitivity to increase abruptly [6,7]. Based on these findings we explore and analyze in this Letter the possibility to improve the response speed and the sensitivity of LN:Fe,Mn crystals by additional tetravalent dopants.

LN:Zr,Fe,Mn crystals were grown along the *c* axis by the conventional Czochralski method. The [Li]/[Nb] composition was selected as 48.38/51.62, and 0.075 wt. % Fe$_2$O$_3$, 0.01 wt. % MnO, and 2 mol. % ZrO$_2$ were doped into the melt. After an annealing treatment and polarization, the crystal was cut to 3-mm-thick plates along the *y* faces and optically polished for the characterization by a two-color holographic recording. A nonvolatile holographic storage was investigated by the experimental setup illustrated schematically in Fig. 1. An extraordinarily po-

larized beam from a cw frequency-doubled solid-state laser was split into two beams of equal intensity (intensity per beam being 200, 300, and 400 mW/cm^2), which were incident symmetrically on the sample at an angle of incidence of 30°. The grating vector was aligned along the *c* axis to exploit the largest electro-optic coefficient γ_{33}. We used an A400 mercury lamp as the UV light source with a wavelength centered at 365 nm. The LN:Zr,Fe,Mn specimens were preexposed to the UV light for at least 1 h. Then the hologram was recorded using the two coherent beams at 532 nm with the sensitizing UV beam on, until the saturation was reached. A third beam from a He–Ne laser (632.8 nm) with a weak intensity ($\sim$0.5 mW/cm^2) was used at its appropriate Bragg angle to measure the diffraction efficiency. For the fixation the holograms were illuminated by one single green beam after the recording (same intensity as for the recording).

Figure 2 shows the measured diffraction efficiency as a function of time. It proves that a nonvolatile holographic recording has indeed been achieved. The saturation and the nonvolatile diffraction efficiencies are 53.2% and 7.5%, respectively, while the response time shortens to only 2.3 s. When fixing the holograms, the diffraction efficiency does not monotonously decrease, but increases first and then de-
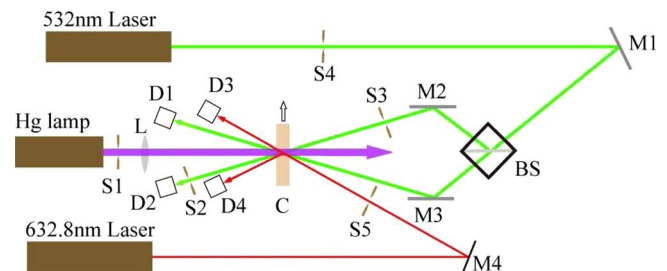
Fig. 1. (Color online) Experimental setup for experiments on nonvolatile holographic storage: M1–M4, mirrors; BS, beam splitter; S1–S5, shutters; D1–D4, detectors; L, lens; C, crystal.
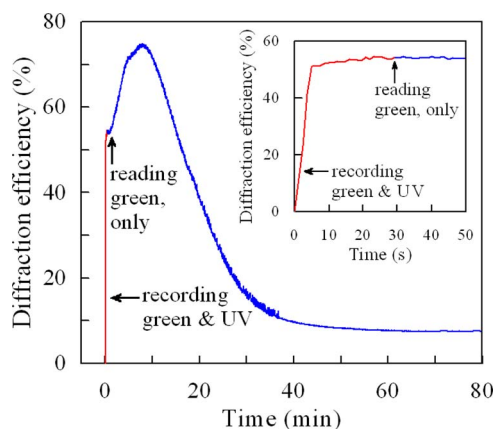
Fig. 2. (Color online) Holographic recording and fixing characteristics of LN:Zr,Fe,Mn. Recording time is 30 s; readout time is about 80 min. The inset shows the recording process (0–30 s).

creases, which can be explained by self-enhancement during the readout. While the recording time is only some seconds, the erasing time is in the range of some tens of minutes. This read-write asymmetry is an important advantage for huge data storage and long-time writing. The extrapolation of this readout experiment shows that the diffraction efficiency drops to approximately 7.4% for a continuous readout over one week. The holographic storage properties of this triply doped LN were investigated for different oxidation states and for different ratios of recording (sum of the signal and reference beams) and sensitizing intensities (I_{rec}/I_{sen}). Results on the saturation and fixed diffraction efficiencies, response time, and sensitivity are listed in Table 1. From Table 1 one sees that the response time shortens down to 0.95 s for a sample oxidized for 20 h at a ratio of I_{rec}/I_{sen} $=400/40$. Although the oxidation treatment in general increases the response time, it rises only to 2.3 s for a sample oxidized in air at 700 °C for 48 h, while the saturation and nonvolatile diffraction efficiencies still stay at a high level.

Generally, the photorefractive sensitivity (S) is calculated as $S=(1/I_{rec}L)(\partial\sqrt{\eta}/\partial t)|_{t=0}$, where η, t, I_{rec}, and L represent the diffraction efficiency, the time, the total recording intensity, and the sample thickness, respectively. Although this equation is a good measure of the sensitivity for a normal holographic

Table 1. Two-Color Holographic Storage for Different Oxidation States and Light Intensities[a]

Oxidation Time (h)	I_{rec}/I_{sen} (mW/cm^2)	η_s (%)	η_f (%)	S (cm/J)	S' (cm/J)	τ_r (s)
24	800/40	53.8	9.5	0.86	0.36	2.8
24	600/40	52.7	8.1	1.05	0.41	2.6
24	400/40	57.6	7.8	2.73	1.01	1.4
48	400/40	53.2	7.5	1.59	0.59	2.3
20	400/40	56.4	8.0	3.47	1.31	0.95

[a] η_s, saturation diffraction efficiency; η_f, fixed diffraction efficiency; S, photorefractive sensitivity, S', modified sensitivity for nonvolatile storage; τ_r, response time.

recording, it does not take the effect of partial erasure during the readout in a two-color holographic recording into account. In the latter case it is better to use $S'=\beta S=\beta(1/I_{rec}L)(\partial\sqrt{\eta}/\partial t)|_{t=0}$ as a figure of merit, where β is the ratio of $\sqrt{\eta}$ for after a sufficient readout and before any readout. Up until now, the best results for the sensitivities S and S' achieved in LN:Fe,Mn have been 0.15 and 0.08 cm/J, respectively [8]. From Table 1, we can see that the sensitivities of LN:Zr,Fe,Mn are appreciably improved, being 3.47 and 1.31 cm/J, respectively.

Another figure of merit for holographic storage is the dynamic range ($M/\#$), defined as the number of holograms that can be multiplexed in a given crystal. The dynamic range of two-color recording can be calculated by [9] $M/\# = \beta A_0(\tau_e/\tau_r)$, where A_0 is the saturation grating strength and τ_r and τ_e are the recording and erasure time constants, respectively. To obtain the erasure time constant, we fitted the readout curve to an exponential function $\sqrt{\eta}=A \exp(-t/\tau_e)$. Because there is strong self-enhancement and scattering grating, the fitting process starts from where the diffraction efficiency equals to the difference between the saturation and self-enhanced efficiencies. During the readout only half of the former recording intensity is used; thus the fitted time constants are divided by a factor of 2. $M/\#$ was calculated as 35.7 for a 3-mm-thick sample that had been oxidized for 48 h. As $M/\#$ is proportional to the thickness of the recording material, we have $M/\# \approx 11.9$, which is over ten times larger than former results [5].

There are plenty of intrinsic defects in commercial congruent LiNbO$_3$ (CLN): the deficiency of Li$_2$O induces Li-site vacancies (V_{Li}^-) and charge compensated antisite Nb^{5+} (Nb$_{Li}^{5+}$) ions [10]. Part of the Nb$_{Li}^{5+}$ ions forms small polarons (Nb$_{Li}^{4+}$) by trapping electrons, and some Nb$_{Li}^{5+}$ ions with neighboring normal-site Nb ions (Nb$_{Nb}^{5+}$) form bipolarons (Nb$_{Li}^{4+}$ Nb$_{Nb}^{4+}$) by trapping a pair of electrons with opposite spins. Bipolarons and small polarons can transform into each other by illumination with suitable light or by heat treatment. Hesselink et al. utilized these bipolarons and small polarons to achieve nonvolatile holographic storage in pure LN [11]. Therefore the band diagram given by Buse et al. [5] for the photorefractive centers in congruent LN:Fe,Mn crystal should at least include the energy levels of Fe$^{2+/3+}$, Mn$^{2+/3+}$, Nb$_{Li}^{4+}$ Nb$_{Nb}^{4+}$, and Nb$_{Li}^{4+}$ as shown in Fig. 3(a). When electrons are excited from Mn^{2+} ions into the conduction band by UV light or from Fe^{2+} ions by visible light, excitation from Nb$_{Li}^{4+}$ Nb$_{Nb}^{4+}$ and Nb$_{Li}^{4+}$ can take place, too. These electrons can recombine not only with Fe^{3+} and Mn^{3+} but also with Nb$_{Li}^{4+}$ Nb$_{Nb}^{5+}$ and Nb$_{Li}^{5+}$. Because there are about 1 mol. % Nb$_{Li}^{5+}$ ions in the CLN, the excited electrons have a much higher probability to get trapped by intrinsic defects rather than extrinsic Fe^{3+} and Mn^{3+} ions. This process slows down the electron mobility for nonvolatile storage appreciably. Therefore, to increase the sensitivity of the LN:Fe,Mn crystal, intrinsic defects should be elimi-
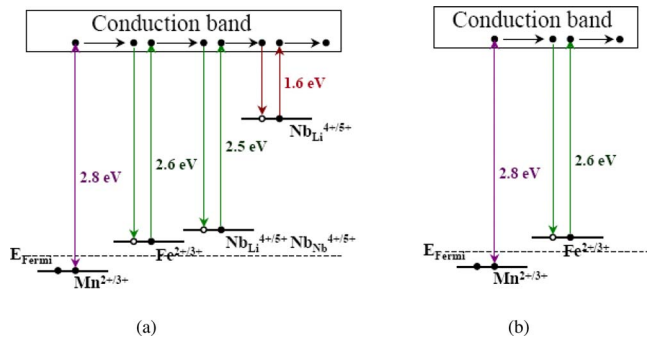
Fig. 3. (Color online) Energy level diagram of dopants and intrinsic defects in the forbidden gap of LN. (a) Normal congruent LN, doubly doped with iron and manganese; (b) ideal doubly doped LN.

nated, such that a real two energy level system is obtained as shown in Fig. 3(b).

One way to solve this problem is to grow stoichiometric LN:Fe,Mn crystals. However, this is difficult to achieve. Up until now, even without dopants, strictly stoichiometric pure LN (Li/Nb = 50/50) single crystals of practical size and quality have not been grown. As to doubly doped LN, we even do not know where the stoichiometric melt composition is. Zhang *et al.* reported that doping optical damage resistant elements, such as Mg, Zn, or In, into LN:Fe above a certain threshold concentration can strongly shorten the photorefractive response time [12], because all Nb_{Li}^{5+} ions are pushed to normal Nb-sites by the doping ions. Unfortunately Fe^{3+} and part of the Fe^{2+} ions are thereby also pushed into Nb-sites [13]. This causes these $Fe^{2+/3+}$ ions to loose their function as photorefractive centers. Thus the photorefractive efficiency decreases, and there is no obvious increase in the photorefractive sensitivity. In former investigations we found that when tetravalent ions are codoped into LN:Fe, they only push Nb_{Li}^{5+} ions to Nb-sites and do not affect the site occupation of $Fe^{2+/3+}$ ions thus resulting in a significant shortening of the response time [6,7]. As $Mn^{2+/3+}$ ions have the same valence as $Fe^{2+/3+}$ ions, all lower than +4, it is reasonable to assume that tetravalent ions do not affect the site occupation of $Mn^{2+/3+}$ ions. Therefore, tetravalent doping ions not only shorten the response time but also improve the sensitivity of LN:Fe,Mn crystals.

It should be pointed out that the sensitivity depends on the intensity ratio of recording and sensitizing light. Experimental results had suggested that a sensitizing beam with a higher intensity than the recording intensities is needed to achieve a high sensitivity [14]. Hence higher sensitivities can be achieved for triply doped LN crystals by decreasing I_{rec}/I_{sen}. The high absorption of LN in the UV light results in a decrease in the UV intensity with the sample thickness; larger sensitivities can be obtained for thinner samples [8]. Triple-doped crystals with Hf, Fe, and Mn have also been grown. Although the saturation diffraction efficiency can reach 50%, the response time turned out to be about 10 s, i.e., the sensitivity is lower than that of LN:Zr,Fe,Mn. Mg or In, Fe, and Mn triply doped LN crystals were also investigated. As expected, they do not exhibit any nonvolatile holographic storage.

The material issue has always been the obstacle for holographic data storage moving to the market. In this study, we tried what we believe to be a new approach by growing Zr, Fe, and Mn triply doped LN crystals. The codoping of Zr eliminates undesired intrinsic electron traps, which greatly enhances the charge transition speed for nonvolatile holographic storage. As a result, the response time of LN:Zr,Fe,Mn for nonvolatile holographic storage became smaller than 1.0 s, and the measured sensitivity S' became as high as 1.31 cm/J. In summary, LN:Zr,Fe,Mn crystals combine the advantages of high diffraction efficiency, long storage lifetime, fast response speed, strong resistance to light-induced scattering, and nonvolatility.

References

1. D. Psaltis and F. Mok, Sci. Am. **273**, 70 (1995).
2. M. Haw, Nature **422**, 556 (2003).
3. L. Dhar, K. Curtis, and T. Fäcke, Nat. Photonics **2**, 403 (2008).
4. A. Hellemans, Science **286**, 1502 (1999).
5. K. Buse, A. Adibi, and D. Psaltis, Nature **393**, 665 (1998).
6. S. Li, S. Liu, Y. Kong, J. Xu, and G. Zhang, Appl. Phys. Lett. **89**, 101126 (2006).
7. Y. Kong, S. Wu, S. Liu, S. Chen, and J. Xu, Appl. Phys. Lett. **92**, 251107 (2008).
8. O. Momtahan, G. H. Cadena, and A. Adibi, Opt. Lett. **30**, 2709 (2005).
9. A. Adibi, K. Buse, and D. Psaltis, Opt. Lett. **24**, 652 (1999).
10. P. Lerner, C. Legras, and J. P. Dumas, J. Cryst. Growth **3–4**, 231 (1968).
11. L. Hesselink, S. Orlov, A. Liu, A. Akella, D. Lande, and R. Neurgaonkar, Science **282**, 1089 (1998).
12. G. Zhang, J. Xu, S. Liu, Q. Sun, and G. Zhang, Proc. SPIE **2529**, 14 (1995).
13. G. Zhang, Y. Kong, and J. Xu, OSA Trends Opt. Photonics Ser. **62**, 166 (2001).
14. O. Momtahan and A. Adibi, J. Opt. Soc. Am. B **20**, 449 (2003).

Angular multiplexing storage of light pulses and addressable optical buffer memory in Pr^{3+}:Y$_2$SiO$_5$ based on electromagnetically induced transparency

Yanfei Tu, Guoquan Zhang,[*] Zhaohui Zhai, and Jingjun Xu

The MOE Key Laboratory of Weak Light Nonlinear Photonics, Nankai University, Tianjin 300457, China and Photonics Center, School of Physics, Nankai University, Tianjin 300071, China

We observed angular multiplexing storage of multiple light pulses in a Pr^{3+}:Y$_2$SiO$_5$ crystal based on electromagnetically induced transparency. Addressable routing of stored light pulses with an angular resolution of ~1° and without cross-talk between two neighboring channels, which serves as an addressable optical buffer memory, was demonstrated experimentally in a 3-mm Pr^{3+}:Y$_2$SiO$_5$ crystal. Angular multiplexing storage of light pulses opens a way to manipulate light pulses selectively and in parallel, and therefore, is of important potential applications in quantum information processing and addressable all-optical delay lines and buffers.

I. INTRODUCTION

Slow light was demonstrated in various systems employing electromagnetically induced transparency (EIT) [1,2], coherent population oscillation [3,4], stimulated Brillouin [5] or Raman scatterings [6], dispersive nonlinear wave coupling [7], and artificial resonance in structured materials such as photonic crystal waveguides and microring resonators [8–11]. It has been studied intensively not only for the underlying fundamental physics but also for its many important potential applications on nonlinear optics [12–14], quantum information processing [15,16], optical switching [17], highly sensitive interferometry or sensor [18], optical storage [2,19–21], and especially the optical delay lines and buffers in the next-generation telecommunication networks [22,23]. The delay-bandwidth product (DBP) estimated as the time delay in unit of the pulse duration is a key parameter for various slow light applications. For example, a large DBP corresponds to a large capacity for optical storage and buffer memory [22]. The DBP around 80 was reported in hot cesium vapor by the use of a double absorption resonance [24] and in optical fiber based on wavelength conversion [25], respectively. Nevertheless, tunable delay with larger DBP and fast reconfiguration rate in solids is desirable to meet the requirement of practical buffer applications. Angular multiplexing is a technique to multiplex many storage channels in a same spatial position on the basis of angular selectivity of the stored information. It offers an effective way to manipulate the stored information in parallel and in an addressable way. This technique has been demonstrated in holographic data storage system to achieve large storage capacity [26].

Coherent interaction between light and matter based on quantum interference effects, such as EIT [27–29], provides a powerful way to manipulate light propagation dynamics and optical information. The achievement on slow light with a group velocity of 17 m/s in an ultracold gas of sodium atoms based on EIT by Hau *et al.* [1] dramatically stimulated the investigation on slow light and its possible applications.

Impressive progresses on the slowdown and storage of light pulses [30–34], even encoded with images [35–37], have been made recently. Yet the small DBP of slow light achieved experimentally in EIT media, especially in solids, inhibits its progress to practical applications.

In this paper, we studied the angular selectivity of the light pulse storage and retrieval in Pr^{3+}:Y$_2$SiO$_5$ (hereafter, Pr:YSO) crystals based on the EIT effect. Angular multiplexing storage of multiple light pulses and addressable optical routing were demonstrated experimentally, which provides an effective way to route light pulses in parallel and in an addressable way. The erasing effect induced by the storage processes in the subsequent channels and its influences on the practical storage capacity are discussed.

II. EXPERIMENTAL SETUP

The experimental setup scheme is shown in Fig. 1. A 3-mm Pr:YSO crystal of 0.05% Pr^{3+} was held at 3.4 K in a cryostat. A single frequency laser radiation at 605.78 nm from a coherent 899–29 dye laser was split into four beams. Two stronger beams C1 and C2 served as the coupling beams, while the other two weaker beams P1 and P2 were the probe beams in the experiment of angular multiplexing storage of light pulses. Each beam can be modulated in intensity and shifted in frequency independently by the corresponding accousto-optical modulator (AOM) with a frequency sweeping range of ±25 MHz. All beams were polarized linearly and in parallel to yield maximal absorption in the Pr:YSO crystal. The beams were focused into the Pr:YSO crystal with a 160 μm diameter through a lens of a 30-cm-focal length, and the beam spots in the crystal were monitored by a charge-coupled device (CCD) camera to ensure a perfect beam overlap. The two probe beams were partially reflected by two glass slides just before being focused into the crystal, and the temporal traces were monitored by two photomultiplier tubes (PMTs) as references. The transmitted intensities of two probe beams after the crystal were measured by PMT1 and PMT2, respectively.

III. SLOWDOWN AND STORAGE OF LIGHT PULSES

A spectrally isolated Λ-type three-level ensemble in an initial state with all population in level $|1\rangle$ was prepared

---
*zhanggq@nankai.edu.cn
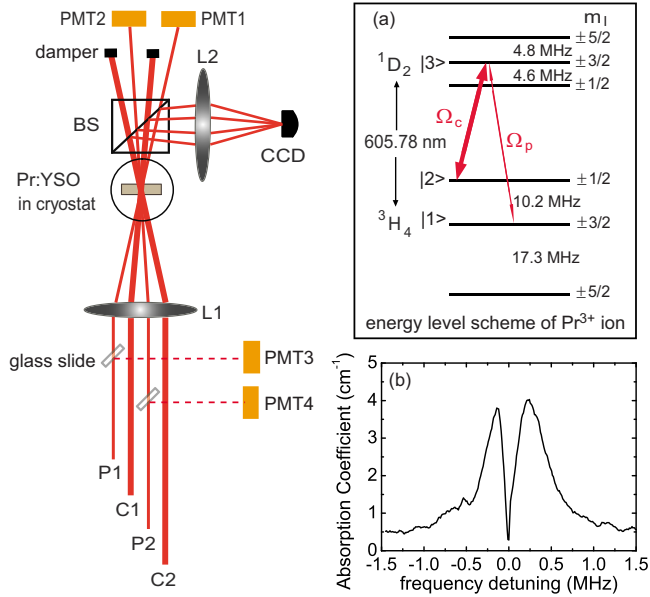
FIG. 1. (Color online) Experimental setup scheme. Here, L: lens, BS: beam splitter, PMT: photomultiplier tube, and CCD: charge-coupled device camera. The dampers were used to block the laser beams when necessary. Note that the intensity and the frequency shift of each beam were controlled independently through AOMs, which are not shown in the figure. The inset (a) shows the hyperfine energy-level structure of the transition $^3H_4 \leftrightarrow {}^1D_2$ of Pr^{3+} ion in YSO crystal, where Ω_c and Ω_p are the Rabi frequencies of the coupling and the probe fields, respectively. In the inset (b), a transparency dip in the antihole absorption spectrum indicates the EIT effect, which appeared when a 10-μW-probe beam swept over a spectral range of ± 1.5 MHz with the central frequency resonant at the transition $|1\rangle \leftrightarrow |3\rangle$, while a 5-mW-coupling beam drove resonantly the transition $|2\rangle \leftrightarrow |3\rangle$.

following the procedures in Refs. [38,39] by combining the optical pumping and spectral hole-burning techniques. This technique permits selective addressing of well-defined transition in a single ensemble of ions. The Pr:YSO crystal was pumped optically by a 90-ms-preparation pulse (beam C1, 7.5 mW) sweeping over a frequency range of -12.7 MHz–5.3 MHz for ten times to create a broad spectral hole. This was followed by a 50-μs 7.5-mW-repumping pulse with a relative frequency shift of 17.3 MHz to create spectral antiholes within the just burned spectral hole. After a 100 μs delay, a series of 200-μs, 1.2-mW-cleaning pulses with a periodical time of 400 μs and a relative frequency shift of -10.2 MHz were applied for 8 ms to prepare the initial state with all population in level $|1\rangle$. Robust coherence between levels $|1\rangle$ and $|2\rangle$ was achieved by applying a coupling field along C1 and a probe field along P1 driving the transitions $|2\rangle \leftrightarrow |3\rangle$ and $|1\rangle \leftrightarrow |3\rangle$, respectively. EIT was observed under the two-photon resonance condition of the Λ-type ensemble, as shown in the inset (b) of Fig. 1.

Slowdown and storage of light pulses were demonstrated under the EIT condition. A time delay of ~ 0.7 μs, corresponding to a DBP of ~ 0.14, was achieved with a 5-μs, 0.5-mW-Gaussian probe pulse and a 5-mW-coupling beam driving resonantly the Λ-type ensemble. Light pulses were stored in Pr:YSO by mapping the optical information onto a
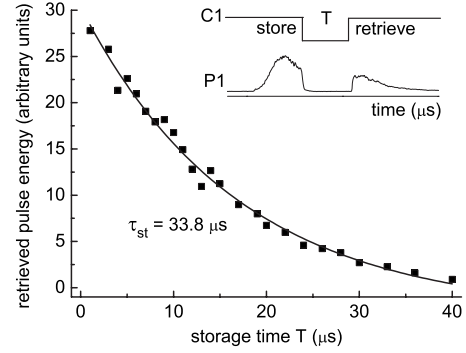
FIG. 2. The retrieved pulse energy as a function of the storage time T in Pr:YSO crystal at 3.4 K. A 5-μs, 0.5-mW-Gaussian probe pulse was stored in the crystal by switching off the 5-mW-coupling beam adiabatically. The crossing angle between the coupling and the probe was 1.8° in air. After a certain storage time T, the stored pulse was retrieved by a 5-mW-phase-matched retrieval beam at the same frequency as the coupling beam. The solid squares are the measured data, in which each point represents an average over 100 measurements, while the curve is a least-square fit to the experimental data by the use of an exponential decay dynamics as $\exp(-2T/\tau_{st})$ with $\tau_{st}=33.8$ μs. The inset shows the time sequence of the coupling and the retrieval (along beam C1) and the probe and the retrieved pulses (along beam P1), respectively.

dark state, a coherent superposition of levels $|1\rangle$ and $|2\rangle$ [19,31], when the coupling beam was switched off adiabatically. The stored pulses were retrieved with an exactly phase-matched retrieval pulse after a certain storage time T, as shown in the inset of Fig. 2. The dark state is immune to spontaneous emission of the excited level $|3\rangle$, and the relaxation rate between the ground-state hyperfine levels is much smaller than the decay rate of the atomic coherence in Pr:YSO crystal [31,39]. In this case, the retrieved pulse energy (i.e., the area of the retrieved pulse) is proportional to the square of the stored coherence, which was measured to decay exponentially with a storage lifetime τ_{st} of 33.8 μs at 3.4 K, as shown in Fig. 2. It is evident that the DBP can be extended to be more than 6 by means of the light pulse storage technique. Longdell *et al.* [40] reported stopped light pulses with a storage time longer than 1 s, indicating that much larger DBP is achievable in Pr:YSO based on the EIT effect.

IV. ANGULAR SELECTIVITY AND ADDRESSABLE OPTICAL BUFFER MEMORY

More interestingly, we found that the pulse retrieval is of high angular selectivity due to the requirement of phase-matching condition. Figure 3 shows a typical angular detuning rocking curve of the retrieved pulse energy efficiency η defined as the energy ratio of the retrieved to the incident pulses. In this experiment, a 5-μs, 0.5-mW-Gaussian pulse along beam P1 was stored in the Λ-type ensemble by turning adiabatically off a 5-mW-coupling beam along beam C1. The crossing angle between the probe and the coupling was 1.8° in air. After a storage time $T=5$ μs in dark, the stored pulse was retrieved by a 5-mW-retrieval beam along beam C2,
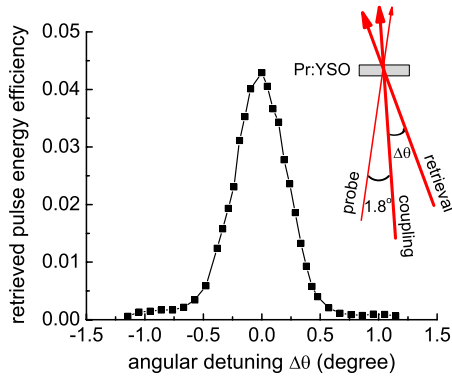
FIG. 3. (Color online) A typical angular detuning rocking curve of the retrieved pulse energy efficiency for light pulses stored in Pr:YSO based on the EIT effect. The inset shows the relative angular positions among the probe, the coupling, and the retrieval beams.

which was of the same frequency as the coupling beam but was detuned angularly from the coupling beam by an angle $\Delta\theta$. As expected, η is peaked at the exact phase-matching position, i.e., when the retrieval beam propagates collinearly with the coupling beam, while it decreases rapidly to zero with the increase in the angular detuning $\Delta\theta$. The retrieved pulses may experience the electromagnetically induced focusing or defocusing effect induced by the radial intensity profile of the retrieval beam [41]. This electromagnetically induced focusing or defocusing effect may deflect the retrieved pulse and therefore destroy the phase-matching condition during the retrieval process. We verified experimentally that the retrieved pulses were deflected by an angle on the order of $\sim 0.06°$ in our case by the electromagnetically induced focusing or defocusing effect. This may modify the angular detuning rocking curve profile in Fig. 3 by up to $\sim 10\%$ but is not large enough to destroy the phase-matching condition during the retrieval. The rocking curve of η is characterized by an angular resolution of $\sim 1°$. This property makes it possible to store multiple light pulses at the same spatial position of the crystal by means of angular multiplexing technique and then to read out selectively and in parallel the stored light pulses at desired time delays without crosstalk among different channels, which may serve as an addressable all-optical buffer memory.

Figure 4 shows a proof-of-principle demonstration of an addressable two-channel all-optical buffer memory based on the angular multiplexing storage of multiple light pulses using the setup shown in Fig. 1. Two 5-μs, 0.5-mW light pulses were stored in sequence in two different channels but in the same spatial position of the crystal by means of angular multiplexing. The crossing angle between the probe and the coupling was 1.8° in air for both channels. The angular distance between two coupling beams was 3.9° in air, which is larger than the angular selectivity resolution $\sim 1°$ in air determined by the rocking curve in Fig. 3. After a dark storage time, for example, $T=1.25$ μs, the pulse stored in channel 1 (by the coupling C1 and the probe P1) was retrieved by a phase-matched 4-μs-retrieval pulse along beam C1. With an additional dark storage time of 2.5 μs, the pulse stored in channel 2 was also retrieved by the corresponding phase-
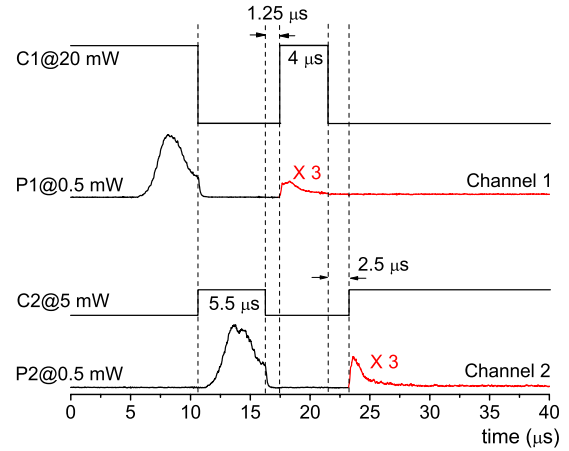
FIG. 4. (Color online) Proof-of-principle demonstration of an addressable two-channel all-optical buffer memory. Note that the strength of the retrieved signal pulses in both channels is multiplied by a factor of 3 for clarity.

matched retrieval beam along beam C2. No cross-talk between channels was found during the retrieval processes, as shown in Fig. 4.

Note that we used a 20-mW-retrieval pulse in channel 1 to get stronger retrieved signal. This is because the coherence stored in channel 1 decreases significantly due to the erasing effect induced by the subsequent storage process in channel 2. Such an erasing effect can be clearly seen in Fig. 5, where we show the decay time constant τ_e of the stored coherence in Pr:YSO under the illumination of phase-mismatched erasing beam of different intensities. The stored coherence in Pr:YSO crystal decays exponentially, as shown in the inset (b) in Fig. 5. As expected, the decay time constant is smaller at a higher erasing intensity I, which can be well described
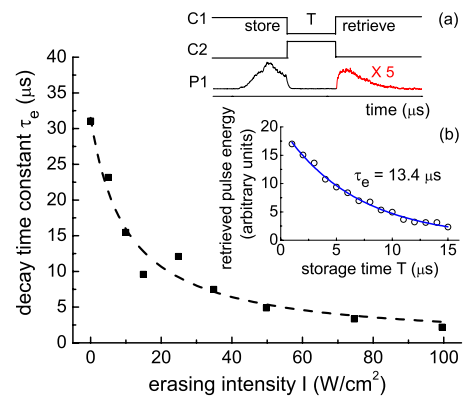
FIG. 5. (Color online) Decay time constant τ_e as a function of the erasing intensity I. The dashed curve is a least-square fit to the experimental data using a formula $\tau_e = \tau_{st}/(1+\beta I)$. The inset (a) shows the time sequence of the coupling and the retrieval pulses (beam C1), the erasing pulse (beam C2), and the probe and the retrieved pulses (beam P1), respectively. The retrieved light pulse strength is multiplied by a factor of 5 for clarity. The inset (b) shows the typical decay dynamics of the retrieved light pulse energy with a 25 W/cm^2 erasing beam; the curve is a least-square fit to the experimental data by the use of an exponential function $\exp(-2T/\tau_e)$.

by the relationship $\tau_e = \tau_{st}/(1 + \beta I)$, where β is a fitting parameter. We employed a 5-mW-coupling beam for the pulse storage in channel 2 in order to reduce the erasing effect.

The storage capacity in one channel for the Λ-type ensemble based on EIT can be estimated roughly by DBP [22]. A larger value of DBP means more pulses can be stored in one channel in the ensemble. When the DBP in a single channel is maximized in a crystal with a finite thickness [42,43], it is still possible to increase the capacity of a buffer memory by using angular multiplexing technique, while at the same time providing the advantage of parallelism and selectivity in routing the stored light pulses. The strength of the stored pulses in a channel will be reduced due to the erasing effect induced by the subsequent storage processes in other channels, and the stored pulses also decay due to various decay processes such as the decay of the ground states of the ensemble. These effects will reduce the efficiency of the multiplexing technique, and the number of channels that can be multiplexed will be limited on the requirement of an acceptable signal-to-noise ratio of the retrieved signal pulses in each channel. For quantum applications, such as quantum memories of single-photon states, the loss due to the erasing directly impacts the performance of angular multiplexing. On the other hand, the full storage capacity of the EIT media is determined by the number density of active Pr^{3+} ions in the crystal that contribute to the EIT effect, while only a fraction of active Pr^{3+} ions, which is determined by the Rabi frequency ratio Ω_p/Ω_c, are consumed in a single-channel storage [31]. Therefore, a lower Rabi frequency ratio Ω_p/Ω_c but large enough to keep an acceptable signal-to-noise ratio

in each channel will allow one to multiplex more channels in the crystal.

V. CONCLUSION

In conclusion, we found that for the light pulses stored in EIT media, the retrieval process is of high angular selectivity. With this angular selectivity, one can store multiple light pulses in Pr:YSO crystal by angular multiplexing and achieve addressable all-optical delay lines and buffer memories without cross-talk among different channels. Various decay processes of the EIT ensemble and the erasing effect during the multiplexing process will limit the number of channels that can be multiplexed on the requirement of an acceptable signal-to-noise ratio in each channel. Due to the possibility to store light pulses on the order of 1 s in Pr:YSO crystals based on the EIT effect, an all-optical buffer memory with many addressable channels, in which each channel with a desired reasonable time delay, seems to be feasible.

[1] L. V. Hau, S. E. Harris, Z. Dutton, and C. H. Behroozi, Nature (London) **397**, 594 (1999).

[2] A. V. Turukhin, V. S. Sudarshanam, M. S. Shahriar, J. A. Musser, B. S. Ham, and P. R. Hemmer, Phys. Rev. Lett. **88**, 023602 (2002).

[3] M. S. Bigelow, N. N. Lepeshkin, and R. W. Boyd, Phys. Rev. Lett. **90**, 113903 (2003).

[4] M. S. Bigelow, N. N. Lepeshkin, and R. W. Boyd, Science **301**, 200 (2003).

[5] K. Y. Song, M. G. Herráez, and L. Thévenaz, Opt. Express **13**, 82 (2005).

[6] J. E. Sharping, Y. Okawachi, and A. L. Gaeta, Opt. Express **13**, 6092 (2005).

[7] G. Zhang, F. Bo, R. Dong, and J. Xu, Phys. Rev. Lett. **93**, 133903 (2004).

[8] M. F. Yanik and S. Fan, Phys. Rev. Lett. **92**, 083901 (2004).

[9] M. F. Yanik, W. Suh, Z. Wang, and S. Fan, Phys. Rev. Lett. **93**, 233903 (2004).

[10] Y. A. Vlasov, M. O' Boyle, H. F. Hamann, and S. J. McNab, Nature (London) **438**, 65 (2005).

[11] Q. Xu, P. Dong, and M. Lipson, Nat. Phys. **3**, 406 (2007).

[12] S. E. Harris, J. E. Field, and A. Imamoğlu, Phys. Rev. Lett. **64**, 1107 (1990).

[13] S. E. Harris and L. V. Hau, Phys. Rev. Lett. **82**, 4611 (1999).

[14] H. Wang, D. Goorskey, and M. Xiao, Phys. Rev. Lett. **87**, 073601 (2001).

[15] M. D. Lukin and A. Imamoğlu, Phys. Rev. Lett. **84**, 1419 (2000).

[16] K. Surmacz, J. Nunn, K. Reim, K. C. Lee, V. O. Lorenz, B. Sussman, I. A. Walmsley, and D. Jaksch, Phys. Rev. A **78**, 033806 (2008).

[17] D. M. Beggs, T. P. White, L. O'Faolain, and T. F. Krauss, Opt. Lett. **33**, 147 (2008).

[18] Z. Shi, R. W. Boyd, D. J. Gauthier, and C. C. Dudley, Opt. Lett. **32**, 915 (2007).

[19] C. Liu, Z. Dutton, C. H. Behroozi, and L. V. Hau, Nature (London) **409**, 490 (2001).

[20] D. F. Phillips, A. Fleischhauer, A. Mair, R. L. Walsworth, and M. D. Lukin, Phys. Rev. Lett. **86**, 783 (2001).

[21] Z. Zhu, D. J. Gauthier, and R. W. Boyd, Science **318**, 1748 (2007).

[22] R. W. Boyd, D. J. Gauthier, and A. L. Gaeta, Opt. Photonics News **17**, 18 (2006).

[23] F. Xia, L. Sekaric, and Y. Vlasov, Nat. Photonics **1**, 65 (2007).

[24] R. M. Camacho, M. V. Pack, J. C. Howell, A. Schweinsberg, and R. W. Boyd, Phys. Rev. Lett. **98**, 153601 (2007).

[25] J. E. Sharping, Y. Okawachi, J. van Howe, C. Xu, Y. Wang, A. E. Willner, and A. L. Gaeta, Opt. Express **13**, 7872 (2005).

[26] G. Barbastathis and D. Psaltis, in *Holographic Data Storage*, edited by H. J. Coufal, D. Psaltis, and G. T. Sincerbox

(Springer-Verlag, Berlin, 2000), pp. 21–62.

[27] K.-J. Boller, A. Imamoğlu, and S. E. Harris, Phys. Rev. Lett. **66**, 2593 (1991).

[28] S. E. Harris, Phys. Today **50**(7), 36 (1997).

[29] B. S. Ham, P. R. Hemmer, and M. S. Shahriar, Opt. Commun. **144**, 227 (1997).

[30] M. D. Lukin and A. Imamoğlu, Nature (London) **413**, 273 (2001).

[31] M. Fleischhauer and M. D. Lukin, Phys. Rev. Lett. **84**, 5094 (2000).

[32] M. Fleischhauer, A. Imamoğlu, and J. P. Marangos, Rev. Mod. Phys. **77**, 633 (2005).

[33] P. Arve, P. Jänes, and L. Thylén, Phys. Rev. A **69**, 063809 (2004).

[34] G. Nikoghosyan, Eur. Phys. J. D **36**, 119 (2005).

[35] R. M. Camacho, C. J. Broadbent, I. Ali-Khan, and J. C. Howell, Phys. Rev. Lett. **98**, 043902 (2007).

[36] M. Shuker, O. Firstenberg, R. Pugatch, A. Ron, and N. Davidson, Phys. Rev. Lett. **100**, 223601 (2008).

[37] P. K. Vudyasetu, R. M. Camacho, and J. C. Howell, Phys. Rev. Lett. **100**, 123903 (2008).

[38] F. Beil, J. Klein, G. Nikoghosyan, and T. Halfmann, J. Phys. B **41**, 074001 (2008).

[39] M. Nilsson, L. Rippe, S. Kröll, R. Klieber, and D. Suter, Phys. Rev. B **70**, 214116 (2004).

[40] J. J. Longdell, E. Fraval, M. J. Sellars, and N. B. Manson, Phys. Rev. Lett. **95**, 063601 (2005).

[41] R. R. Moseley, S. Shepherd, D. J. Fulton, B. D. Sinclair, and M. H. Dunn, Phys. Rev. Lett. **74**, 670 (1995).

[42] R. W. Boyd, D. J. Gauthier, A. L. Gaeta, and A. E. Willner, Phys. Rev. A **71**, 023801 (2005).

[43] R. S. Tucker, P.-Ch. Ku, and C. J. Chang-Hasnain, J. Lightwave Technol. **23**, 4046 (2005).

Optical trapping and manipulation of metallic micro/nanoparticles via photorefractive crystals

Xinzheng Zhang, Junqiao Wang, Baiquan Tang, Xinhui Tan, Romano A. Rupp, Leiting Pan, Yongfa Kong, Qian Sun, and Jingjun Xu*

MOE Key Laboratory of Weak-Light Nonlinear Photonics, TEDA Applied Physics School and Institute of Physics, Nankai University, Tianjin 300457, China
*jjxu@nankai.edu.cn

Abstract: A simple method to trap and manipulate metallic micro/nano-particles on the surface of photorefractive crystals is proposed. After inducing inhomogeneous charge density and space-charge fields in photorefractive crystals by non-uniform illumination, both uncharged and charged metallic particles can be trapped on the illuminated surface due to dielectrophoretic force and electrophoretic force, respectively. A transition from dielectrophoresis to electrophoresis is observed when manipulating nano-silver particles with high surface space-charge field. Our results show that this method is simple and effective to form surface microstructures of metallic particles.

OCIS codes: (350.4855) optical manipulation; (220.4000) Microstructure fabrication (190.5330) Photorefractive optics

References and links

1. H. R. Stuart, and D. G. Hall, "Absorption enhancement in silicon-on-insulator waveguides using metal island films," Appl. Phys. Lett. **69**(16), 2327–2329 (1996).
2. H. R. Stuart, and D. G. Hall, "Enhanced dipole–dipole interaction between elementary radiators near a surface," Phys. Rev. Lett. **80**(25), 5663–5666 (1998).
3. A. Tao, F. Kim, C. Hess, J. Goldberger, R. He, Y. Sun, Y. Xia, and P. Yang, "Langmuir-Blodgett silver nanowire monolayers for molecular sensing using surface-enhanced Raman spectroscopy," Nano Lett. **3**(9), 1229–1233 (2003).
4. L. Eurenius, C. Hägglund, E. Olsson, B. Kasemo, and D. Chakarov, "Grating formation by metal-nanoparticle mediated coupling of light into waveguided modes," Nat. Photonics **2**(6), 360–364 (2008).
5. D. G. Grier, "A revolution in optical manipulation," Nature **424**(6950), 810–816 (2003).
6. K. C. Neuman, and S. M. Block, "Optical trapping," Rev. Sci. Instrum. **75**(9), 2787–2809 (2004).
7. A. Ashkin, J. M. Dziedzic, J. E. Bjorkholm, and S. Chu, "Observation of a single-beam gradient force optical trap for dielectric particles," Opt. Lett. **11**(5), 288–290 (1986).
8. P. Y. Chiou, A. T. Ohta, and M. C. Wu, "Massively parallel manipulation of single cells and microparticles using optical images," Nature **436**(7049), 370–372 (2005).
9. H. A. Pohl, "The motion and precipitation of suspensoids in divergent electric fields," J. Appl. Phys. **22**(7), 869 (1951).
10. H. A. Pohl, "Some effects of nonuniform fields on dielectrics," J. Appl. Phys. **29**(8), 1182 (1958).
11. R. Pethig, and G. H. Markx, "Applications of dielectrophoresis in biotechnology," Trends Biotechnol. **15**(10), 426–432 (1997).
12. P. R. Gascoyne, and J. Vykoukal, "Particle separation by dielectrophoresis," Electrophoresis **23**(13), 1973–1983 (2002).
13. G. Hu, and D. Li, "Multiscale phenomena in microfluidics and nanofluidic," Chem. Eng. Sci. **62**(13), 3443–3454 (2007).
14. R. Pethig, and G. H. Markx, "Applications of dielectrophoresis in biotechnology," Trends Biotechnol. **15**(10), 426–432 (1997).
15. M. P. Hughes, "Dielectrophoretic behavior of latex nanospheres: low-frequency dispersion," J. Colloid Interface Sci. **250**(2), 291–294 (2002).
16. A. Iuga, R. Morar, A. Samuila, and L. Dascalescu, "Electrostatic separation of metals and plastics from granular industrial wastes," IEE Proc. Sci. Meas. Technol. **148**(2), 47–54 (2001).
17. S. S. Sarkisov, M. J. Curley, N. V. Kukhtarev, A. Fields, G. Adamovsky, C. C. Smith, and L. E. Moore, "Holographic surface gratings in iron-doped lithium niobate," Appl. Phys. Lett. **79**(7), 901–903 (2001).
18. H. A. Eggert, F. Y. Kuhnert, K. Buse, J. R. Adleman, and D. Psaltis, "Trapping of dielectric particles with light-induced space-charge fields," Appl. Phys. Lett. **90**(24), 241909 (2007).
19. P. Yeh, "Introduction to photorefractive nonlinear optics," (Wiley, New York, 1993).

20. K. Buse, "Light induced charge transport processes in photorefractive crystals I: Models and experimental methods," Appl. Phys. B **64**(3), 273–291 (1997).
21. E E. Serrano, V. Lopez, M. Carrascosa, and F. Agullo-Lopez, "Steady-state photorefractive gratings in LiNbO/sub 3/ for strong light modulation depths," IEEE J. Quantum Electron. **30**, 875–880 (1994).
22. B. Khusid, and A. Acrivos, "Effects of interparticle electric interactions on dielectrophoresis in colloidal suspensions," Phys. Rev. E Stat. Phys. Plasmas Fluids Relat. Interdiscip. Topics **54**(5), 5428–5435 (1996).
23. X. Shen, J. Zhao, R. Wang, X. Yi, P. Yeh, and H. Chen, "Recording of second-harmonic index gratings in photorefractive $(K_{(0.5)} Na_{(0.5)})_{(0.2)} (Sr_{(0.75)} Ba_{(0.25)})_{(0.9)} Nb_{(2)}O_{(6)}$ crystals," Opt. Lett. **24**(5), 312–314 (1999).
24. F. Vachss, and L. Hesselink, "Nonlinear photorefractive response at high modulation depths," J. Opt. Soc. Am. A **5**(5), 690–701 (1988).
25. A. Bledowski, J. Otten, and K. H. Ringhofer, "Photorefractive hologram writing with modulation 1," Opt. Lett. **16**(9), 672–674 (1991).
26. P. Vaveliuk, B. Ruiz, and N. Bolognini, "Analysis of the steady-state photorefractive harmonic gratings," Phys. Rev. B **59**(16), 10985–10991 (1999).
27. P. M. Johansen, "Photorefractive space-charge field formation: linear and nonlinear effects," J. Opt. A, Pure Appl. Opt. **5**(6), S398–S415 (2003).
28. A. M. Glass, D. von der Linde, and T. J. Negran, "High-voltage bulk photovoltaic effect and the photorefractive process in $LiNbO_3$," Appl. Phys. Lett. **25**(4), 233–235 (1974).
29. R. S. Weis, and T. K. Gaylord, "Lithium niobate: Summary of physical properties and crystal structure," Appl. Phys., A Mater. Sci. Process. **37**(4), 191–203 (1985).

1. Introduction

Manipulation of micro- and nanometer particles such as dielectric spheres, viruses, bacteria, living cells, organelles, small metallic particles, and even strands of DNA, plays a more and more important role in biology, physics, chemistry and material science. These tools are used to perform important functions such as the sorting, addressing, transporting, and trapping of cells and particles in these fields. The number of potential applications of nanoscopic metallic particles is growing rapidly because of their unique electronic structures, extremely large specific surface areas and unique optical property. Therefore, many researchers pay more attention to manipulate metallic nanoparticles to form different kinds of microstructures and nanostructures (such as metal islands [1,2], metal wires [3] and metal gratings [4]) by physical or chemic methods. Metal island films could couple incident light into the waveguide modes of the detector, resulting in increased absorption and enhanced the sensitivity of very thin semiconductor photodetector [1]. Silver nanowires were of special importance and could significantly enhance the Raman scattering signal of molecules adsorbed on the surface [3], because silver possessed the highest electrical conductivity among metals. Eureniusl et al. [4] demonstrated patterning with subwavelength periodicity through interference between incoming light and light coupled into the waveguided modes of a thin membrane. The grating structure was formed by single-laser-pulse irradiation of disordered, evaporated gold (or silver) films of discrete island on a 40-nm-thick, square membrane.

Micro- and nanometer particles can be trapped optically [5–8] or electrokinetically [9–13]. In general, optical trapping and manipulation are derived from optical tweezers, which were first introduced and realized in experiment by Ashkin in the early 1970s [7]. Conventional optical tweezers rely on the field gradients near the focus of a laser beam which give rise to a trapping force towards the focus. Optical tweezer can trap objects as small as 5 nm and can exert forces exceeding 100 pN with resolutions as fine as 100 aN [5]. Optical manipulation techniques apply to particles as diverse as atoms, large molecules, small dielectric spheres in the size range of tens of nanometers to tens of micrometers. Electrokinetic trapping includes two mechanisms: dielectrophoresis and electrophoresis. While uncharged particles are driven by electric forces via dielectrophoresis from nonuniform electric fields, charged particles can be manipulated via electrophoresis and thus by uniform as well as nonuniform electric fields [14–16].

Optical trapping provides highly accurate manipulation, but requires high light illumination intensities and the number of particles that can be manipulated in parallel is limited. Electrokinetic methods can drive large and a mess of particles, but demand external voltage supplies. There is another choice, namely combining optical with electrokinetic methods using photorefractive crystals [17,18]. Spatially inhomogenous illumination excites and redistributes the charge carriers in photorefractive crystals to form space-charge fields

which modulate the refractive index via the electro-optic effect [19,20]. The light-induced space-charge fields not only affect the refractive index but also provide near-surface lateral forces to manipulate small particles. Sarkisov et al. demonstrated the principle of trapping of micron-size dielectric particles by near-surface electric forces on lithium niobate (LN) crystals [17]. Polystyrene spheres of 2.6μm diameter in colloidal water suspension were successfully deposited on the surface and formed periodical distributions of the particles. Recently, Eggert et al. continued these studies: dielectric particles, e.g. chalk particles in air and silicon carbide particles in paraffin oil were trapped on the surface of photorefractive crystals [18]. The grating period of the dielectric particles was half of the one of the space-charge field.

This method is attractive since it neither requires high light intensity nor external voltage supply. The space-charge fields of photorefractive crystals can manipulate the uncharged particles via dielectrophoresis and charged particles via electrophoresis in the same way as the external electric field does. Dielectrophoresis [9–12] is defined as the motion imparted on uncharged particles by polarization and by action of the so-called electric field gradient. The direction of motion of the particle is independent of the direction of the electric field. The magnitude of the dielectrophoretic force depends on the size and shape of the particles, on the conductivity and permittivities of the particles and their suspending medium, and on the magnitude and gradient of the applied electric field. Electrophoresis [12] is the motion of charged particles relative to the surrounding liquid under the influence of an electric field. Particles dispersed in solution almost always carry an electric surface charge, hence an electrostatic Coulomb force is exerted on the dispersed particles from an external electric field. Negatively charged particles move towards the positive electrode and vice versa. The electrophoretic force is proportional to the product of the charge of the particles and the magnitude of the applied electric field.

When a particle is placed in an electrical field, it experiences a lateral force $\vec{F}_{elec}$ given by [12]

$$\vec{F}_{elec} = q\vec{E} + (\vec{m} \cdot \nabla)\vec{E} + \frac{1}{6}\nabla(\vec{Q} : \nabla\vec{E}) + \cdots \tag{1}$$

The first term embodies all electrophoretic phenomena while other terms contain all dielectrophoretic phenomena. The first term describes the Coulomb interaction between the net charge q of the particles and the electric field E. This term vanishes in the absence of a net charge on the particle or in an alternating field, whose time average is zero. The rest terms in Eq. (1) arise from the interaction of the dielectric polarization components induced in the particle by the spatially inhomogeneous electric field including the dipole ($\vec{m}$), the quadrupole ($\vec{Q}$) and higher order phenomena.

The dielectrophoretic force on a polarizable particle in a non-uniform field can be written as [11]

$$F_{DEP} = 2\pi\varepsilon_m r^3 \alpha \nabla E^2 \tag{2}$$

Where r is the particle radius, α is a parameter defining the effective polarizability of the particle, and ε_m is the complex permittivitiy of the surrounding medium.

In this paper, we investigate the trapping of metallic micro and nanoparticles and the formation of metallic microstructures by light-induced space-charge fields on the surface of LN crystals. Our results show that uncharged metallic particles can be manipulated via the dielectrophoretic effect, and charged ones via the electrophoretic effect. Moreover, a transformation from dielectrophoresis to electrophoresis is observed when manipulating nano-silver particles with strong space-charge fields.

2. Experimental results and discussion

Two LN crystals (*y*-cut) were used in our experiments both with the dimensions of $x \times y \times z(c)$ = $10.0 \times 1.0 \times 21.0$ mm^3. Sample I and Sample II were doped with 0.025 wt.% iron and with

0.05 wt.% iron, respectively. Two extraordinary polarized coherent beams from an Argon ion laser (wavelength λ = 488 nm) overlapped to form a light pattern with a sinusoidal intensity distribution in the sample. The light modulation depth m was approximately 1. A Mach-Zehnder interferometer was employed in our optical system to obtain the inhomogeneous light pattern, the periods of the light patterns were several hundreds of micrometers. The grating vector of the light pattern was parallel to the c-axis of the crystal. Charge carriers redistributed under the illumination and built up space-charge fields with the same fringe spacing. Metallic or non-metallic nanoparticles were dispersed into silicon oil by ultrasonic dispersion to form a colloidal solution. The colloid was dripped onto the surface of the modulated crystal, which was inclined so that the colloidal drop could pass through the illuminated area. A Zeiss microscope was used to observe the distribution of particles on the surface of the crystal.

Charged particles can be trapped by electrophoretic force from the space-charge fields. Firstly, aluminum particles with an average diameter of 1.52 μm, which were positively charged, were dispersed into silicone oil by ultrasonic dispersion. Holographic gratings with a period of 250 μm were recorded in Sample I without application of an external voltage. Then a drop of silicone oil with the suspended particles was brought onto the illuminated region of the inclined sample. Most of the particles were trapped onto the surface of the sample, the distribution of the particles result is shown in Fig. 1. The period of the particle distribution was the same as that of the interference pattern.
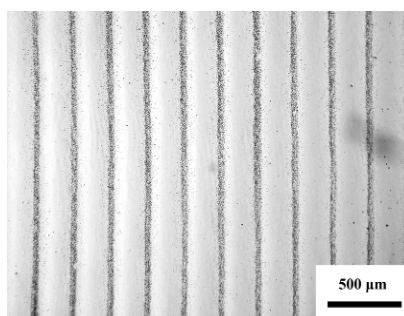
Fig. 1. Charged aluminum particles were trapped by electrophoretic forces. The period of particle grating was 250 μm, which was the same as that of light pattern.

In a second experiment, we used negatively charged non-metallic particles as well as aluminum particles to form particles lines. The non-metallic particles chosen here were carbon particles, the ones of a carbon powder for HP laser printers, which could easily be negatively charged. The diameter of those carbon particles was about 8~16 μm. The period of the light pattern, i.e. the space-charge field, was 400 μm. We dropped both the silicone oil with suspended toner particles and the silicone oil with suspended aluminum particles on the recorded grating region. Clear particle lines were established after several seconds on the inclined Sample I as shown in Fig. 2. The black large particles were toner particles, and the gray small particles were aluminum powder. Carbon and aluminum particles were trapped in different locations, i.e. the carbon particles lines and the aluminum particles lines appeared alternately. Carbon and aluminum particle gratings had the same period as the light pattern. The distance between adjacent carbon and aluminum particle lines was about 200 μm, which was the half of the period of the recorded holographic grating.
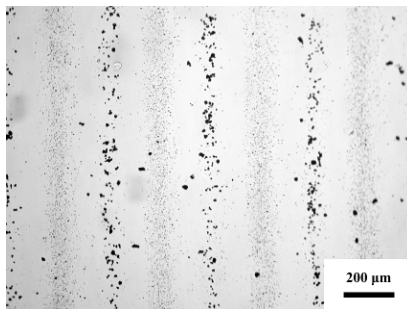
Fig. 2. Negatively charged carbon particles and positively charged aluminum particles lined alternately. The black large particles were carbon particles, and the gray small particles were aluminum powder. The period of each particle grating was 400 μm, which was the same as that of light pattern.

We also tried to trap particles on the surface of Sample I in air. After recording the grating, we sprinkled carbon particles on the surface of the crystal. The carbon particles immediately positioned onto periodic lines with the same period as the light pattern. However, the particle lines were less clear than the ones formed by suspension in silicone oil.

Uncharged metallic particles, silver particles in our experiment, were trapped by dielectrophoretic forces, too. The mean diameter of the silver particles was 50 nm. The silver particles were also dispersed in silicone oil by ultrasonic dispersion. The period of the interference pattern was about 540 μm. The suspension of silver particles in silicone oil was dropped onto the illuminated region of Sample I, particle lines established after several seconds. Based on Eq. (2), one expected uniform particle grating with fringe spacing of 270 μm induced by a sinusoidal space-charge field, which was half of the period of the light pattern. However, a nonuniform particle grating was observed in Fig. 3, the pitches between two adjacent particle strips were 252 μm and 288 μm alternately. The average period of the nonuniform particle grating was 270 μm, which was consistent with the analysis on dielectrophoresis. The nonuniform distribution was due to the high light modulation ($m \approx 1$), which caused the space-charge field with an asymmetric ramp function distribution instead of a sine-shape distribution [21]. There was a low concentration line in the middle of every particle strip, which might result from particle-particle interaction by repulsive forces [22] and the existence of the position of zero dielectrophoretic force.
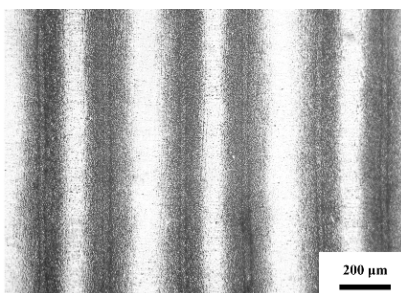
Fig. 3. Uncharged silver particles were trapped by dielectrophoretic forces. The period of light pattern was 540 μm. The particle strips were non-uniformly distributed (252 μm and 288 μm pitches, alternatively) due to high light modulation, which could be considered as particle grating with average fringe spacing 270 μm resulting from dielectrophoresis.

In order to understand the dynamic behavior of silver particles under the space-charge field, we first assume that the light modulation depth is much smaller than 1 and thus the space-charge field has a distribution of the sinusoidal shape $E_{sc} = E_a \sin(kx)$ as shown in Fig. 4, where E_a is the amplitude of the space-charge field with order of magnitude 10^7 V/m, k is the grating wave vector ($k = 2\pi / \Lambda$, where Λ is the period of the light pattern).
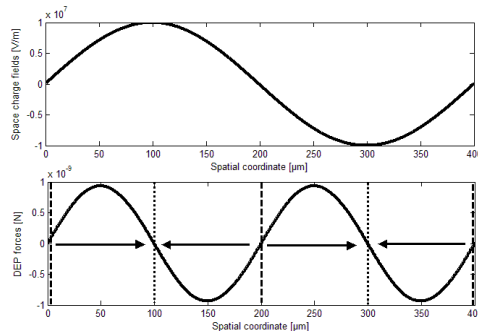
Fig. 4. The simple sketch map shows the profile of space-charge field (upper line) and dielectrophoretic (DEP) force (lower line) with the spatial coordinate in one period, respectively. The arrowheads indicate the direction of DEP forces.

According to the Eq. (2), the maximum dielectrophoretic forces, whose direction is parallel to the surface, take place at the region of high electric field gradients. The arrowheads in Fig. 4 indicate the different direction of the dielectrophoretic force at different regions. The dielectrophoretic forces will drive the polarized particles along the direction of the arrowheads moving to the positions where the dielectrophoretic force is zero, i.e. the high electric field locations (the dotted lines shown in Fig. 4). Thus the metallic particles, which dispersed in the insulation oil, deposit near the location of high electric field. But in Fig. 3, less or no metallic particles exist at center of the high electric field area, which is due to the existence of the zero dielectrophoretic force. There are two high concentration regions in one period, which means that the period of particles lines formed by dielectrophoretic force is half as that formed by electrophoretic force comparing with the same period of light pattern.

However, it is well-known that though the optical intensity is sinusoidal, the space-charge fields and photorefractive gratings in photorefractive crystals are not exactly sinusoidal. The amplitude and phase of the space-charge fields and index gratings depend on the modulation depth of intensity m [23]. Kukhtarev's theory [19,20] on holographic gratings was carried out under linear approximation with a small modulation depth of the light intensity ($m \ll 1$), whereas under the large m, the increasing contribution of the high order harmonic implies a localization of the space-charge field pattern, leading to both space-charge field and the ionized donor concentration with sharp-peaked profiles [24–27]. In case of LN:Fe crystals, the dominating mechanism is photovoltaic effect, the saturation voltage of space-charge field can be in excess of 10^7 V/m [28]. Strong photovoltaic effect can introduce a clear asymmetry in the profile of space-charge fields and the gratings fringes [21].

Therefore, under the large light modulation, the electric fields have a complicated and asymmetric ramp function distribution instead of a sine-shape distribution, which leading to the asymmetric distribution of the dielectrophoretic force, which can explain the experimental results in Fig. 3.

The transition from a dominating dielectrophoretic effect to a prevailing electrophoresis effect had been observed experimentally with Sample II. Because the iron concentration of Sample II was twice larger than that of Sample I, stronger space-charge fields could be induced in Sample II [20,28]. After recording a photorefractive grating with a period of 600 μm into Sample II, silicone oil with suspended uncharged silver particles was dropped on the illuminated region. The surface was inspected immediately by microscopy. The pictures in Fig. 5 show the change of the distribution of the silver particles with time. The time interval between two adjacent pictures was about 30 seconds.
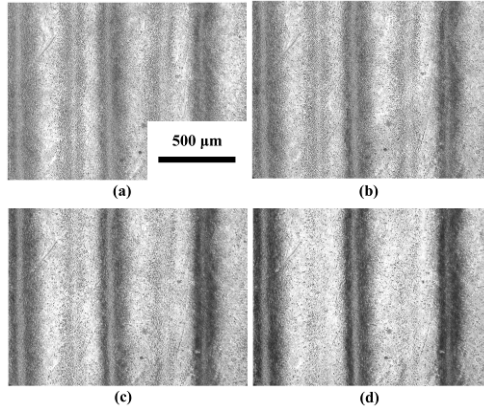
Fig. 5. The temporal evolution of the distribution of the silver particles strips. The period of light pattern was 600 μm and the time interval between two adjacent pictures was about 30 seconds. A transition from dielectrophoresis to electrophoresis was observed.

Because the silver particles were electroneutral in the beginning, the silver particles were trapped by dielectrophoretic force to form non-uniform particle gratings as shown in Fig. 5(a). There were two particle strips in one period of the light pattern, which was the characteristic of the dielectrophoretic effect. The dielectrophoretic forces led particles to the area with positive bound charges and with negative bound charges. High concentration strips were formed at negatively charged regions, while low concentration strips were formed at positively charged regions. The silver particles at regions with positive charges were soon charged, the particle-particle and particle-crystal repulsive forces would drive the charged silver particles away from the initial location by electrostatic Coulomb force. Then particle strips at positively charged area became lighter and lighter and disappeared in the end while those at negatively charged area became darker and darker as illustrated in Fig. 5. The appearance of the lower concentration line in the middle of the particles strip was due to the existence of the zero point of the dielectrophoretic force as explained above.

3. Conclusions

In summary, we offer a simple and effective method to form surface metal microstructures. Metallic particles had successfully been manipulated and trapped by the strong surface space-charge fields of LN crystals via dielectrophoresis and electrophoresis. Metal particle gratings were formed with periods between several micrometers and several hundreds of micrometers.

Our further study will focus on the fabrication of surface metallic particle patterns with sub-micrometer scale structures. Therefore, we should consider the possible minimal periods of interference pattern and of space-charge field in advance. It is well-known that holographic interference patterns inside a medium have a minimum grating period $\Lambda = \lambda / 2n$ by use of a pair of counter-propagating beams, where n is the refractive index of the recording medium. For LN crystals, the principal extraordinary refractive index n_e is about 2.25 (@ λ = 488 nm) [29], then the minimum grating period in such crystals is about 108 nm. Shen et al. had proposed and demonstrated a novel scheme for recording a second-harmonic index grating to achieve grating period beyond diffraction limit in photorefractive crystals [23]. By using a double-exposure process in a Mach-Zehnder interferometer with a dual input port, they recorded a second harmonic index grating with a period of $\Lambda / 2$. Theoretically, the space-charge field with minimum grating periods of about 54 nm might be achieved in LN crystals by employing this technique. Therefore, in principle we might form metallic particles gratings with the period of several tens nanometer with this method. However, there are some other limiting factors to prevent the fabrication of surface particle pattern with sub-micrometer structure, such as inter-particle interactions and the agglomeration of particles. The inter-particle interactions among charged particles prohibit the formation of high concentration of

particles, and thus affect the fringe visibility. In order to form smooth and continuous particles lines, it is better to use particles with diameter less than one fifth of the fringe spacing. The agglomeration effect will increase the diameter of particles, so we should and might use proper dispersing agent to avoid agglomeration.

Moreover, grating is the foundational microstructure, we can also obtain arbitrary surface microstructure of metallic particles by extended methods. Space-charge fields can be in principle induced by inhomogenous illumination using imaging method with an amplitude or phase mask. Thus optional particle-decorated surface structures in the micrometer range may be fabricated.

Acknowledgements

$(2+1)D$ surface solitons in virtue of the cooperation of nonlocal and local nonlinearities

H. Z. Kang, T. H. Zhang,* B. H. Wang, C. B. Lou, B. G. Zhu, H. H. Ma, S. M. Liu, J. G. Tian, and J. J. Xu

Photonics Research Center, the MOE Key Lab of Weak-Light Nonlinear Photonics, and Tianjin Key Lab of Photonics
Materials and Technology for Information Science, Nankai University, Tianjin, China, 300071
*Corresponding author: zhangth@nankai.edu.cn

We introduce a type of $(2+1)D$ surface soliton in virtue of the cooperation of nonlocal and local nonlinearities. Furthermore, taking advantage of diffusion and drift nonlinearity this type of surface soliton is demonstrated theoretically and experimentally in a storintium barium nitrate crystal. The dynamics behavior of the excitation and propagation of this type of surface soliton are studied using the beam-propagation method and the nonlinear equation of light rays. © 2009 Optical Society of America

OCIS codes: 190.4350, 160.5320, 240.0240.

Self-guided surface waves along the surface of a nonlinear medium are among the most intriguing phenomena in nonlinear optics, which may result in very strong enhancement of nonlinear surface optical phenomena owing to the concentration of beam energy with high intensity [1].

The nonlinear surface waves (SWs) on the boundary of a nonlinear medium are often associated with nonlocal nonlinearity, such as the nonlocal diffusive Kerr nonlinearity [2–4] and the diffusion component of photorefractive (PR) nonlinearity [5–7]. However, the study of nonlinear SWs has not been further developed. One of the difficulties is that the low conversion efficiency of SWs from incident light beams, because most of the energy is reflected by the boundary. One can consider utilizing the local drift nonlinearity to further confine the energy [8,9]. However, another disadvantage is that the above-mentioned SWs are often one dimensional, which cannot efficiently confine the energy of an incident beam, as in the two-dimension case.

Surface solitons present a good method for two-dimensional concentration of light energy, which combine solitons with SWs. There are two necessary elements to support the surface solitons. The first is the mechanism (or method) for the concentration of light energy, which enables the formation of solitons. The other essential element is the mechanism (or method) for confining a light beam near a boundary surface. In 2007 Alfassi *et al.* demonstrated nonlinear SW solitons utilizing self-focusing-type thermal nonlinearity and controlling the boundary conditions of temperatures with a strategy to fulfill the above two elements [10]. The other types of typical surface solitons are discrete surface solitons and surface gap solitons [11–14], which utilize periodic structures and near-face defects induced by nonlinearity to fulfill the above two elements. But the prefabrication of periodical structures is needed.

As we know, nonlocal nonlinearities can lead to the unidirectional transfer of light energy and local nonlinearities can lead to the concentration of light energy. When both of the above nonlinearities exist simultaneously in a nonlinear medium, the two elements for surface solitons can be satisfied. In this

Letter, we theoretically demonstrate and experimentally observe the excitation of a type of surface soliton in virtue of the cooperation of nonlocal diffusion and local drift nonlinearity for the first time (to our knowledge), which is the third type of surface solitons ever found. Furthermore, we also observed the multireflections and the periodic near-boundary oscillations of PR screening solitons for what we believe is the first time.

Considering an *e*-polarized laser beam propagating along the interface of a PR crystal (PRC) and metal, taking into account the diffusion and drift components of PR nonlinearity simultaneously, the complex amplitude $E(x,y,z)$ of the light field satisfies the scalar wave equation

$$\nabla^2 E(x,y,z) + k^2 E(x,y,z) = 0, \tag{1}$$

where $k = k_0[n+\Delta n]$, $k_0 = 2\pi/\lambda_0$, λ_0 is the wavelength in vacuum, n is the refractive index of the *e*-polarized beam in the PRC, Δn is the nonlinear refractive index change in the PRC, $[n+\Delta n]^2 = n^2 - n^4 r_{eff} E_{sc}$, r_{eff} is the effective electro-optical coefficient, and E_{sc} is the space-charge field, which can be can be written as

$$E_{SC}(x,y) = \frac{k_B T}{e} \nabla \ln[I(x,y) + I_d + I_b] + \frac{E_0(I_d + I_b)}{I(x,y) + I_d + I_b}, \tag{2}$$

where k_B is the Boltzman constant, T is the temperature, e is the charge of electron, (negative for the electrons and positive for the holes), E_0 is the applied external electric field. $I(x,y)$ is the light intensity of the PR surface soliton, I_b is the intensity of background illumination, and I_d is the equivalent dark irradiance. The first and the second terms in the right side of Eq. (2) describe the effect of diffusion and the drift nonlinearities, respectively.

First, we look for the $(2+1)D$ stationary PR surface soliton solution as $E(x,y,z) = A(x,y)\exp^{i\beta z}$. β is the propagation constant and $A(x,y) = [I(x,y)/(I_b+I_d)]^{1/2}$ is the normalized amplitude. According to Eqs. (1) and (2), the surface solitons can easily be numerically solved, taking $Sr_{0.6}Ba_{0.4}NbO_3$ (SBN:60) as sample

with $n = 2.2733$ and $r_{eff} = r_{33} = 420 \times 10^{-12}$ m/V [shown as Fig. 1(a)]. The local drift nonlinearity ensures the beam maintaining a soliton shape, just like the formation of PR screening solitons in volume. The effect of nonlocal diffusion nonlinearity is disymmetrical along the c axis, and consequently the PR surface soliton profile is disymmetrical along the c-axis direction.

Then we proceed to address the dynamics behavior of the excitation and propagation of surface solitons at the boundary of photorefractive crystal using the beam propagation method. For convenience, the $(1+1)D$ circumstance is considered. Figures 1(b)–1(d) show the evolvement and propagation of an incident Gaussian beam near SBN surface with 5 cm propagation distance, whose launched points are $x = 200$ μm, 22 μm, and 16.75 μm, respectively. The incident Gaussian beams transform into solitons within 2 mm and experience one-time reflection [shown in Fig. 1(b)], n-times reflections [shown in Fig. 1(c)], and straight propagation along the surface [shown as Fig. 1(d)].

To understand the dynamics of the above phenomena, the nonlinear equation of light ray $\mathrm{d}(n\mathrm{d}r/\mathrm{d}s)/\mathrm{d}s = \nabla n$ is introduced, which can be written as

$$\frac{\mathrm{d}^2 x}{\mathrm{d}z^2} + \frac{1}{n(x)}\frac{\mathrm{d}n(x)}{\mathrm{d}x}\frac{\mathrm{d}x^2}{\mathrm{d}z^2} - \frac{1}{n(x)}\frac{\mathrm{d}n(x)}{\mathrm{d}x} = 0, \qquad (3)$$

where

$$\frac{\mathrm{d}n(x)}{\mathrm{d}x} = \frac{\mathrm{d}}{\mathrm{d}x}\left\{\frac{1}{2}n^3 r_{eff}\left\{\frac{E_0}{A^2(x)+1} \right.\right.$$
$$\left.\left. + \frac{k_B T}{e}\frac{\mathrm{d}}{\mathrm{d}x}[\ln(A^2(x)+1)]\right\}\right\}. \qquad (4)$$

Equation (3) is a parabola equation with square damping, where the first term is the acceleration, the second term is the square damping, and the third term is gravitation. From Eq. (4) one can see that the gravitation and the coefficient of damping do not include variable z explicitly; additionally, the damping is square, and so the track of a group of photons is symmetrical in one projection. After the reflection by boundary, the next symmetrical parabola track continues. One can also see from Eqs. (3) and (4) that the gravitation is caused by diffusion nonlinearity, which determines the direction of gravitation. The incident beam is always bent toward the $-c$ surface and presents periodical oscillation near the surface. When the light beam is launched gradually close to the crystal interface, the closer the beam is launched, the shorter the period of the oscillation is, which accords with the results of Fig. 1. When the beam is launched at the site, where x is equal to half of the size of a surface soliton, the stationary soliton can be formed. Meanwhile, the period of the oscillation is infinitesimal; both the gravitation from diffusion nonlinearity and the repulsion from the boundary cannot bend the soliton beam; i.e., they are exactly balanced by each other.
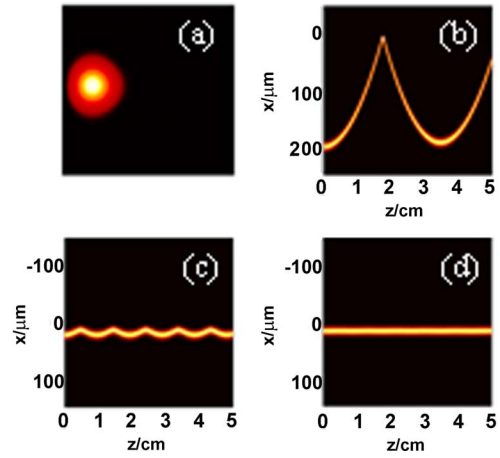
Fig. 1. (Color online) (a) Sketch of a 2D surface soliton, (b) trajectories of the incident beam with the beam center coordinates $x = 200$ μm for one-time reflection, (c) $x = 22$ μm for five-times reflection, (d) $x = 16.75$ μm for steadily propagated PR surface soliton. The applied external electric field is $E_0 = 4000$ V/cm. The FWHMs of the incident beam at $z = 0$ cm are all 10 μm. The crystal surface is located at $x = 0$ μm.

According to the above studies, we set the applied external electric field to 4130 V/cm (1900 V, 4.6 mm) and uniform background illumination using a cold white-light source of 24.5 mW/cm^2 (8.8 mW, 7.8 $\times$ 4.6 mm^2) in our experiment to create a more concentrated soliton. An e-polarized 532 nm laser beam with 9.4 μW output power was focused using a lens ($f = 20$ mm) into an SBN:60 with dimensions of 7.8 $\times$ 4.5 $\times$ 4.6 mm^3. Figure 2 shows the process of the formation and the self-bending of the PR screening soliton in bulk. The size of the formed soliton at the output face is about 30 μm, which is approximately equal to the size of focused laser beam at the input face. The deflection distance of the soliton can reach 278 μm at the output face, which is much larger than the size of the soliton.

The incident laser beam was launched approaching the boundary of the crystal step by step by shifting the crystal. Figures 3, 4, and 5(a) show the images at the input face with the distance from the center of incident beam to the boundary of the crystal about $x = 85$ μm, 35 μm, and 15 μm, respectively. The positive direction of the x axis points to the left, and the dotted lines represent the $-c$ boundary of the crystal, the coordinates of which are $x = 0$ μm. Parts (b)–(h) of Figs. 3–5 describe the entire evolvement processes of the images at the output face for 0, 2, 4, 8, 17, 45, and 95 s, respectively. The curves in the rectangles show the corresponding real-time trajectories of the laser beam. Figures 3 and 4 show that the soliton undergoes one and two times reflection, respectively, and maintains a fine shape of the soliton, which indicates that if the crystal is long enough, the soliton may directly propagate along its surface with oscillation. The experimental results meet with our theoretical calculations very well. This is the first time (to our knowledge) that multireflections and the near-boundary oscillation of solitons have been observed. The time (~ 45 s) taken for the near-surface oscillat-

Fig. 2.   Self-bending of PR screening soliton. The incident beam is converged and self-bended and reaches the steady state at 45 s.
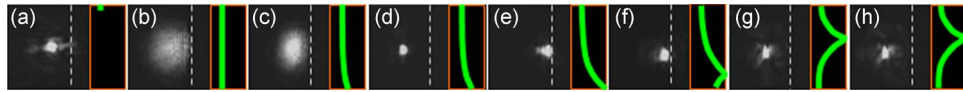
Fig. 3.   (Color online) One-time reflection of a PR screening soliton at the boundary with $x=85$ μm: (a) input image; (b) output image at 0 s. (c), (d) Incident beam is converged and (e) self-bended to the interface at the 8 s, then (f) reflected to the bulk and (g) reaches the steady state at the 45 s; (h) steady output image at 95 s.
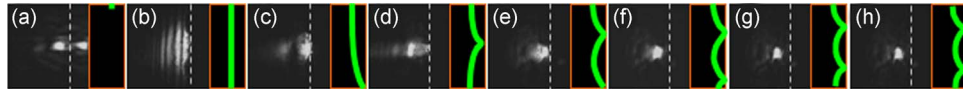
Fig. 4.   (Color online) Two-times reflection of PR screening soliton at the boundary with $x=35$ μm: (a) the input image; (b) output image at 0 s. (c) Incident beam is converged and self-bended to the interface for the first time at 2.33 s, then (d) reflected to the bulk and (e) self-bended to the interface again at 7.67 s then (f) reflected for the second time; it (g) reaches the steady state at the 45 s and (h) steady output image in at 95 s.

Fig. 5.   (Color online) Formation of the PR surface soliton when the incident beam was launched very closed to the $-c$ boundary with $x=15$ μm; (a) the input image; (b) output image at 0 s. (c) Incident beam is converged and (d) self-bended to the interface at the 4 s then (e) confined near the interface, and (f) the image at the output face reaches the steady state at the 17 s, and the (g), (h) steady output image at 45 s and 95 s, respectively.

ing solitons to reach a steady state is identical to that of the self-bending soliton in bulk. Clear interference between the incident beam and its reflection from the boundary was formed at the beginning and disappeared subsequently.

When the laser beam launched close enough to the boundary of the SBN crystal, as shown in Fig. 5, the light beam did not undergo the process of the reflection and oscillation found in Figs. 3 and 4. The diffracted laser beam and its interference fringe at the output face shrink towards boundary and then are confined near the boundary without reflection. After 17 s it begins to maintain a fixed-soliton shape and then forms a stationary surface soliton propagating along the boundary surface. While at this time, the solitons in Figs. 3 and 4 continue the evolvement of the self-bending process. This is because in Figs. 3 and 4 the space-charge field should be reestablished in the self-bending process, which spends more time. The distance from the center of the incident beam to the boundary of the crystal is about 15 μm, which is half of the size of the soliton. The results accord with the above theoretical analysis very well.

The conversion efficiency from the incident beam to the PR surface soliton is about 62.8%. The losses are caused mainly by reflection at the input and output faces and the absorption in the crystal. The high conversion efficiency indicates that the giant enhancement of the nonlinear surface optical phenomena may be expected and applied without the need for specially prefabricated waveguide structures.

References

1. I. I. Smolyaninov, C. H. Lee, and C. C. Davis, Phys. Rev. Lett. **83**, 2429 (1999).
2. D. Mihalache, M. Bertolotti, and C. Sibilia, Prog. Opt. **27**, 229 (1989).
3. P. Varatharajah, A. B. Aceves, J. V. Moloney, and E. M. Wright, J. Opt. Soc. Am. B **7**, 220 (1990).
4. P. Varatharajah, A. Aceves, J. V. Moloney, D. R. Heatley, and E. M. Wright, Opt. Lett. **13**, 690 (1988).
5. G. S. Garcia Quirino, J. J. Sanchez-Mondragon, and S. Stepanov, Phys. Rev. A **51**, 1571 (1995).
6. M. Cronin-Golomb, Opt. Lett. **20**, 2075 (1995).
7. T. H. Zhang, X. K. Ren, B. H. Wang, C. B. Lou, Z. J. Hu, W. W. Shao, Y. H. Xu, H. Z. Kang, J. Yang, D. P. Yang, L. Feng, and J. J. Xu, Phys. Rev. A **76**, 013827 (2007).
8. V. A. Aleshkevich, V. A. Vysloukh, and Y. V. Kartashev, Quantum Electron. **30**, 905 (2000).
9. V. A. Aleshkevich, V. A. Vysloukh, A. A. Egorov, and Y. V. Kartashev, Quantum Electron. **31**, 713 (2001).
10. B. Alfassi, C. Rotschild, O. Manela, M. Segev, and D. N. Christodoulides, Phys. Rev. Lett. **98**, 213901 (2007).
11. K. G. Makris, S. Suntsov, D. N. Christodoulides, G. I. Stegeman, and A. Hache, Opt. Lett. **30**, 2466 (2005).
12. Y. V. Kartashov, V. A. Vysloukh, and L. Torner, Phys. Rev. Lett. **96**, 073901 (2006).
13. A. Szameit, Y. V. Kartashov, F. Dreisow, T. Pertsch, S. Nolte, A. Tünnermann, and L. Torner, Phys. Rev. Lett. **98**, 173903 (2007).
14. X. Wang, A. Bezryadina, Z. Chen, K. G. Makris, D. N. Christodoulides, and G. I. Stegeman, Phys. Rev. Lett. **98**, 123903 (2007).